SYNTHESIS OF NANOCRYSTALLINE TI AND ZR PROMOTED χ -ALUMINA AND ITS

APPLICATION AS THE RU CATALYST SUPPORT FOR CO_2 HYDROGENATION

By

MISS Kanyanat JEENJUMRAS

A Thesis Submitted in Partial Fulfillment of the Requirements

for Master of Engineering (CHEMICAL ENGINEERING)

Department of CHEMICAL ENGINEERING

Graduate School, Silpakorn University

Academic Year 2017

Copyright of Graduate School, Silpakorn University

การสังเคราะห์ผลึกขนาดนาโนของไคอะลูมินาที่ดัดแปรด้วยไทเทเนียมและเซอร์โคเนียม
และการประยุกต์ใช้เป็นตัวรองรับของตัวเร่งปฏิกิริยารูทีเนียมในปฏิกิริยาไฮโดรจิเนชันของ
คาร์บอนไดออกไซด์

โดย
นางสาวกัญญาณัฐ จีนจำรัส

วิทยานิพนธ์นี้เป็นส่วนหนึ่งของการศึกษาตามหลักสูตรวิศวกรรมศาสตรมหาบัณฑิต
สาขาวิชาวิศวกรรมเคมี แผน ก แบบ ก 2 ระดับปริญญามหาบัณฑิต
ภาควิชาวิศวกรรมเคมี
บัณฑิตวิทยาลัย มหาวิทยาลัยศิลปากร
ปีการศึกษา 2560

SYNTHESIS OF NANOCRYSTALLINE TI AND ZR PROMOTED χ -ALUMINA AND
ITS APPLICATION AS THE RU CATALYST SUPPORT FOR CO$_2$ HYDROGENATION

By

MISS Kanyanat JEENJUMRAS

A Thesis Submitted in Partial Fulfillment of the Requirements

for Master of Engineering (CHEMICAL ENGINEERING)

Department of CHEMICAL ENGINEERING

Graduate School, Silpakorn University

Academic Year 2017

Title	Synthesis of nanocrystalline Ti and Zr promoted χ - alumina and its application as the Ru catalyst support for CO_2 hydrogenation
By	Kanyanat JEENJUMRAS
Field of Study	(CHEMICAL ENGINEERING)
Advisor	Okorn Mekasuwandumrong

Graduate School Silpakorn University in Partial Fulfillment of the Requirements for the Master of Engineering

.... Dean of graduate school

(Associate Professor Jurairat Nunthanid, Ph.D.)

Approved by

.... Chair person

(Assistant Professor Tarawipa Puangpetch , Ph.D.)

.... Advisor

(Assistant Professor Okorn Mekasuwandumrong , D.Eng.)

.... Examiner

(Assistant Professor Worapon Kiatkitipong , D.Eng.)

.... External Examiner

(Professor Joongjai Panpranot , Ph.D.)

59404202 : Major (CHEMICAL ENGINEERING)

Keyword : CO2 hydrogenation, Ru catalyst, χ -Al2O3, ZrO2-Al2O3, TiO2-Al2O3

MISS KANYANAT JEENJUMRAS : SYNTHESIS OF NANOCRYSTALLINE TI AND ZR PROMOTED χ -ALUMINA AND ITS APPLICATION AS THE RU CATALYST SUPPORT FOR CO_2 HYDROGENATION THESIS ADVISOR : ASSISTANT PROFESSOR OKORN MEKASUWANDUMRONG, D.Eng.

Ru/χ -Al_2O_3 catalysts prepared with various ruthenium precursors by incipient wetness impregnation method were investigated in CO_2 hydrogenation reaction, and the catalysts were characterized by N_2 physisorption, XRD, TEM, H_2 chemisorption and TPR. It was found that Ru/χ -Al_2O_3 catalyst prepared with ruthenium (III) nitrosyl nitrate (or RNN catalyst) and ruthenium (III) acetylacetonate (or RAA catalyst) precursors exhibited obviously better catalytic activity than Ru/χ -Al_2O_3 catalyst prepared with hexaammineruthenium (III) chloride precursor (or RCl catalyst). CO_2 conversion of RNN and RAA catalysts were 2 times higher than RCl catalyst and also their CH_4 selectivity were higher than RCl catalyst at all reaction temperatures. In addition, effect of ZrO_2 (5 – 20 wt.%) and TiO_2 (2.5 – 15 wt.%) added into χ -Al_2O_3 support by wet impregnation was also investigated. Compared with Ru/χ -Al_2O_3 catalyst, Ru/ZrO_2-Al_2O_3 and Ru/ZrO_2-Al_2O_3 catalysts exhibited higher CO_2 conversion and CH_4 yield than Ru/χ -Al_2O_3 catalyst with high active site and Ru dispersion. The addition of large amount of ZrO_2 (20%ZrO_2) and TiO_2 (15%TiO_2) in Ru catalyst could make a higher turnover frequency (TOF) than other of all Ru catalysts.

ACKNOWLEDGEMENTS

TABLE OF CONTENTS

LIST OF FIGURES

LIST OF TABLES

CHAPTER I

INTRODUCTION

1.1   Motivation

In the last century, concentration of CO_2 in the atmosphere has increased consecutively, resulting from power generation with fossil fuels, activities of industry and deforestation. The recording of CO_2 content in the atmosphere has increased from ~280 ppm before the development of industry to ~390 ppm in 2010 and then, is predicted that it further increased to 570 ppm by the end of the century. The increase of CO_2 emission has created concerns about the increasing of global temperature and climate change due to the greenhouse effect, which has CO_2 as an important component. Therefore, finding methods to reduce the amount of CO_2 in the atmosphere is very interesting and urgent necessary. There are 3 possible strategies presented, that are reduction of CO_2 produced, CO_2 sequestration and utilization of CO_2 [1].

The converting of CO_2 into hydrocarbon product such as methane (CH_4) has received interesting option due to the use of CO_2 captured from natural gas and other sources, combined with H_2 generated from electrolysis of water using renewable electrical energy. It is possible to upgrade CO_2 to useful CH_4 or synthetic natural gas (SNG) [2]. CH_4 can be produced energy though combustion. Moreover, CO_2 released from the production of energy can be recycled into CH_4 by hydrogenation of CO_2.

Many catalysts found in several researches of CO_2 hydrogenation are Ni, Ru, Rh, Pd, Co, Fe, Cu and etc. deposited on various supports (e.g., SiO_2, TiO_2, Al_2O_3, ZrO_2, and CeO_2) [1, 3]. Among all the catalysts, Ru-based catalyst is the most effective noble metal and the most stable when operated in a wide conditions range [3, 4]. However, the activity of Ru-based catalyst depends on the properties of the support.

Alumina (Al_2O_3) is normally used as catalyst and/or support due to its excellent thermal stability, fine particle size and high surface area. In addition, the high stable χ–Al_2O_3 can be prepared with common technique, by calcination of microcrystalline gibbsite [5, 6].

Zirconia (ZrO_2) possesses high surface area, high thermal stability and appropriate in hydrogenation of CO_2 [7]. Titania (TiO_2) is high activity and the most effective when supported Ru catalyst in CO_2 hydrogenation. Moreover, TiO_2-Al_2O_3 enhances activity of catalyst which is higher surface area and thermal stability than the titania or alumina alone [8].

In this research, the activity of Ru supported on χ–Al_2O_3, TiO_2-Al_2O_3 and ZrO_2-Al_2O_3 catalysts is performed in CO_2 hydrogenation reaction. The χ–Al_2O_3 support is obtained by thermal decomposition of gibbsite. The effect of Ru precursors of Ru/χ–Al_2O_3 is also investigated. The two binary oxides supports are prepared by using wet impregnation method. Moreover, the effect of TiO_2 and ZrO_2 content in χ–Al_2O_3 supported Ru catalysts on the physiochemical and catalytic properties are also investigated. The characterization of these catalysts are performed using X-ray diffraction (XRD), N_2 physisorption (BET), H_2 chemisorption, temperature programmed reduction (TPR) and transmission electron microscope (TEM) techniques.

1.2   Objective of Research

The objective of this research is to study the effect of TiO_2-Al_2O_3 and ZrO_2-Al_2O_3 on the physiochemical properties and catalytic performance of supported Ru catalysts in CO_2 hydrogenation reaction.

1.3   Scope of Research

1.3.1   Catalytic preparation

1) The Ru/χ-Al$_2$O$_3$ catalysts used in this research were prepared by incipient wetness impregnation method by using 3 different ruthenium precursors and Ru loading content was fixed at 1 wt.%.

2) The TiO$_2$-Al$_2$O$_3$ and ZrO$_2$-Al$_2$O$_3$ supports were prepared by using wet impregnation method. The content of binary oxides support was varied as 5 wt.%, 10 wt.% and 15 wt.% of TiO$_2$ or ZrO$_2$ and all supports were impregnated with the best Ru precursor from 1).

1.3.2   Catalytic activity test

The activity test of catalysts was performed by CO$_2$ hydrogenation reaction and operated with temperature programmed reaction method at atmospheric pressure.

1.3.3   Catalytic characterization

The characterization of catalysts was determined by various techniques, including:

1) X-ray diffraction (XRD)

2) N$_2$ physisorption (BET)

3) H$_2$ chemisorption

4) Temperature programmed reduction (TPR)

5) Transmission electron microscope (TEM)

1.4   Contribution of Research

1.4.1 Reduce carbon dioxide concentration in atmosphere, which is the cause of greenhouse effect.

1.4.2   Produce methane from CO_2 hydrogenation with χ-Al_2O_3 and binary oxides (TiO_2-Al_2O_3, ZrO_2-Al_2O_3) supported Ru catalysts.

1.4.3 Prepare Ru/χ-Al_2O_3, Ru/TiO_2-Al_2O_3 and Ru/ZrO_2-Al_2O_3 by using incipient wetness impregnation method.

CHAPTER II

THEORY

2.1 CO_2 hydrogenation

Hydrogenation of CO_2 is an one of interesting option for reduction of greenhouse gases [9]. CO_2 can react with hydrogen to production of valuable chemicals and fuels. The main products in this reaction process can be classified into two groups as chemicals and fuels, which illustrated in **Figure 1** [1, 10].
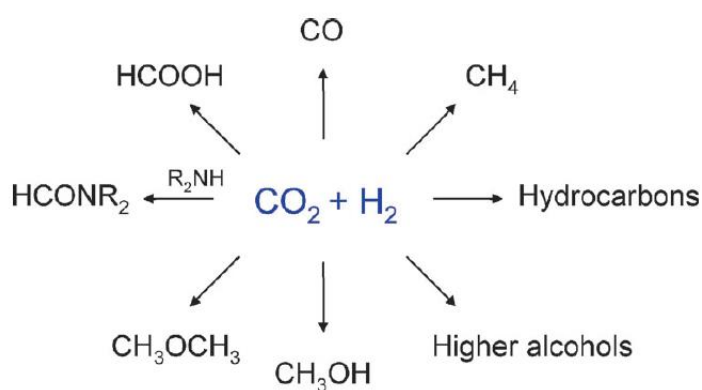
Figure 1 Product species formed from CO_2 hydrogenation process [1].

In CO_2 hydrogenation to methane, it can be called as CO_2 methanation or the Sabatier reaction. The reacted CO_2 with hydrogen can produce syngas and compressed natural gas as methane. This reaction was developed from work of NASA (National Aeronautics and Space Administration) to application of oxygen reclaiming within life support system. CO_2 in cabin atmosphere is combined with hydrogen to obtain methane and water vapor. Which stored water is used in electrolysis process to produce breathing oxygen [1, 11].

The CO_2 methanation equation is shown in Eq. (1) [3, 12].

$$CO_2 + 4H_2 \longrightarrow CH_4 + 2H_2O, \Delta H = -164.75 \text{ kJ/mol} \tag{1}$$
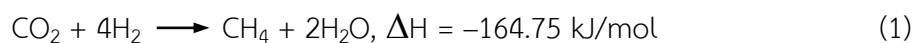
2.2 Ruthenium

Ruthenium (Ru) is one of platinum group metals (PGMs) [13, 14]. It is silvery-grey, shiny metal that looks like platinum. Ruthenium is of the rarest metals in the world. It is harder and more brittle than platinum [14-16]. It is better thermal resistance due to its high melting point as 2,333°C and boiling point as 4,147°C [15, 17]. Ruthenium is not tarnish at room temperature, but can oxidize explosively in air at about 800°C [14, 17]. Other properties of ruthenium are shown in **Table 1** [15, 16].

Because of ruthenium is very hard, it is used as an alloying agent to harden platinum, palladium and other metals in platinum group. Adding ruthenium-hardened alloying agent in platinum and palladium are made for the manufacture of fine jewelry and of electric contacts that extremely wear resistance [14-17]. Ruthenium is high resistance to chemical attack therefore it is used for improving corrosion resistance of titanium by addition of 0.1% Ru [14, 17]. Ruthenium is also versatile catalyst. It is used in removal of H_2S from oil refineries and other industrial processes [14, 17]. It can be catalyst in CO_2 hydrogenation processes to methanol and methane [3, 18].

Table 1 Chemical and physical properties of ruthenium [15, 16].

Ruthenium properties	
Atomic number	44
Molecular weight	101.07
Melting point	2,333°C
Boiling point	4,147°C
Density (g/cm^3)	12.1

2.3 Aluminum oxide

Aluminum oxide also called alumina is chemical equation as Al_2O_3 that is a white or colorless crystalline structure [19]. Its melting point is 2,050°C and its boiling point is 3,500°C [20]. Alumina structure consists two types of sites that is hexagonal and octahedral [21]. The crystalline alumina structures have many different forms which these alumina structure were called as "Transition Alumina" and used Greek alphabet denote the different alumina forms such as chi, kappa, alpha, gamma, theta and rho etc. The different alumina structures can be occurred by five alumina hydroxides: gibbsite, boehmite, beyerite, diaspore and nordstrandite that used as starting structure. The transition alumina is illustrated in **Figure 2** which it depend on thermal transformation [22].
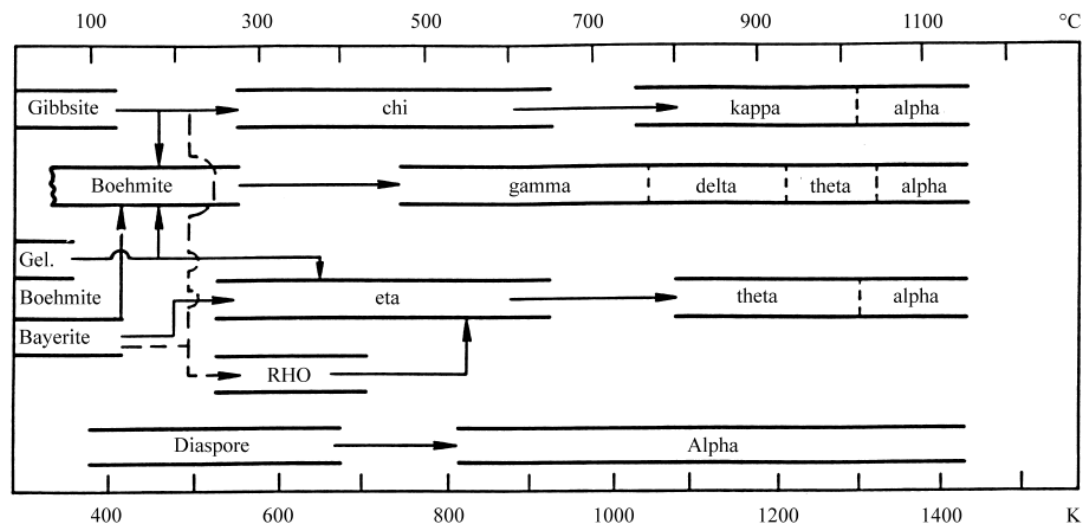
Figure 2 Alumina hydroxides transformation relate with temperature [22].

In the present, alumina is very interesting due to it is broadly application such as adsorbents, coatings, filters, protective barriers, electronic-device fabrication, soft abrasives, ceramics, catalysts and catalyst supports [22-24]. Moreover, 90% of all alumina produced is used in aluminum production. These application indicate the properties of alumina very well that are high thermal stability, low electric conductivity, high resistance to chemical corrosion, high strength and also extreme material hardness—diamond is only harder than alumina [19, 21, 23].

2.4 Zirconium dioxide

Zirconium dioxide (ZrO_2) is also called zirconium oxide or zirconia. It is one of the most use as ceramic materials [25]. Application of zirconium dioxide consists ceramic pigments, artificial jewelry, dental bridges and crowns, fuel cell membranes, joint implants, insulator and fire-retardant materials [25, 26]. It is also used as catalyst supports [27]. Zirconium dioxide has specific properties that is non-magnetic, high acid resistance, low reactivity, great hardness, and excellent thermal stability. It cannot be melted at temperature below 2,680°C. Since its high melting point, it is

the oldest mineral found on the earth [25, 28]. Chemical and physical properties are exposed in **Table 2** [25, 26, 29]. In addition, characteristics of zirconium dioxide is illustrated in TEM image which it shown in **Figure 3** [25].

Table 2 Chemical and physical properties of zirconium dioxide [25, 26, 29].

Zirconium dioxide properties	
Chemical formula	ZrO_2
Molecular weight (g/mol)	123.22
Melting point	2,680°C
Boiling point	4,300°C
Density (g/cm^3)	5.68
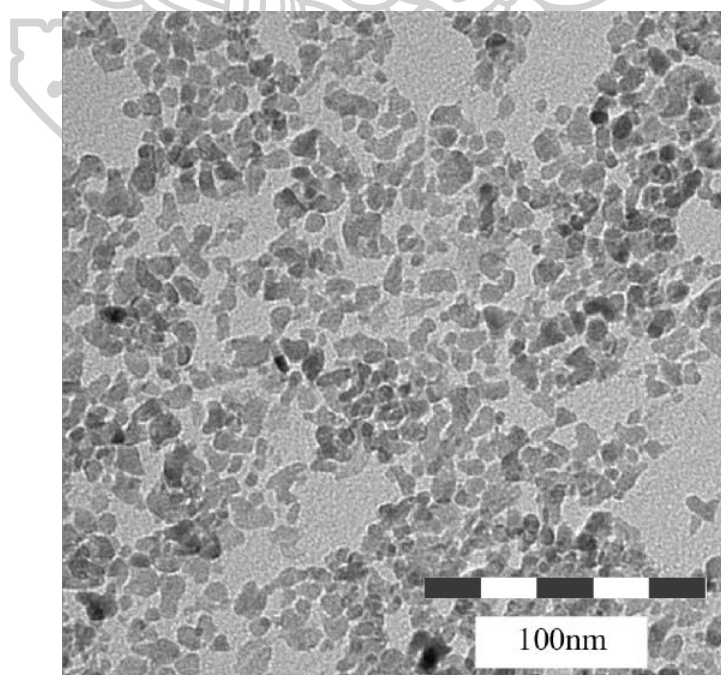
Figure 3 TEM image of zirconium dioxide [25].

Zirconium dioxide phase transformation depend on various temperatures that follows in below [28, 30]:

$$\text{monoclinic} \underset{\approx950°C}{\overset{1,170°C}{\rightleftarrows}} \text{tetragonal} \xrightarrow{2,370°C} \text{cubic} \xrightarrow{2,680°C} \text{liquid (melted)}.$$
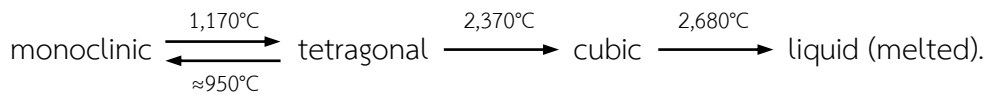
Monoclinic phase is the most stable of zirconium dioxide at low temperature. At temperature of 1,170°C and ambient pressure, tetragonal phase becomes to be transformed and then, it is transformed to cubic phase at 2,370°C [28, 30, 31]. Structural model of three zirconium dioxide phases is indicated in **Figure 4** [31].

● Zirconium dioxide atom
● Oxygen atom
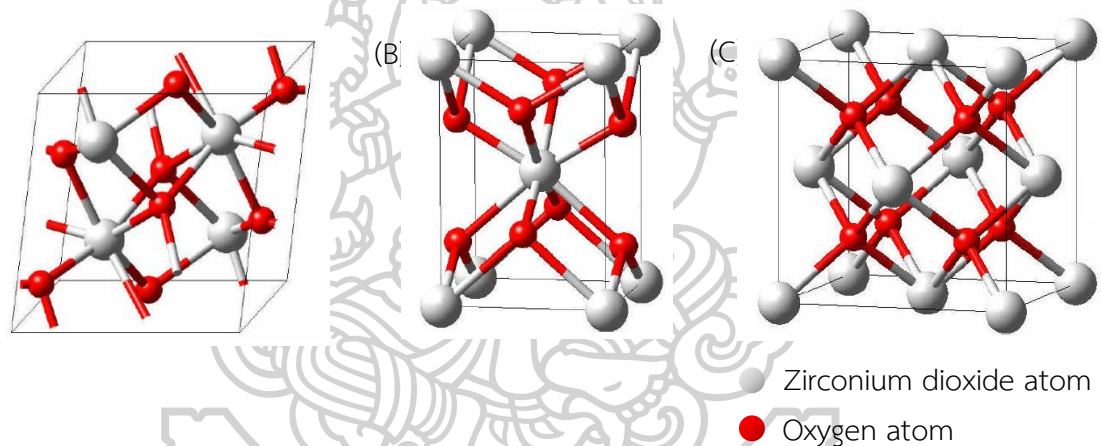
Figure 4 Structural model of zirconium dioxide: monoclinic (A), tetragonal (B) and cubic (C) [31].

2.5 Titanium dioxide

Titanium dioxide (TiO$_2$) is generally known as titania. It is a white, opaque and resists to UV radiation. Since its UV resistance, it is added in cosmetic products such as sunscreen creams, whitening creams, etc. [32, 33]. Other application of titanium dioxide is an additive in paints, coatings, ceramics, filter for polymers, luminescent materials, solar cells and also catalysts [33-35]. **Table 3** is exhibited chemical and physical properties of titanium dioxide [33, 36].

Table 3 Chemical and physical properties of titanium dioxide [33, 36].

Titanium dioxide properties	
Chemical formula	TiO_2
Molecular weight (g/mol)	79.87
Melting point	1,843°C
Boiling point	2,972°C
Density (g/cm^3)	4.23 (rutile) 3.78 (anatase)

Titanium dioxide is used as heterogeneous catalysts such as in CO_2 methanation reaction—it is the most efficient support in Ru catalyst, and in the Deacon reaction [37]. In addition, titanium dioxide is utilized in environmental and photocatalytic for hydrogen production by water splitting, and treatment of polluted air and wastewater [34, 38, 39]. Nowadays, TiO_2 nanostructure can be synthesized by several methods such as sol-gel, hydrothermal, solvothermal, direct oxidation, electrodeposition, microwave methods, etc. [40].

Titanium dioxide has three different polymorphs that consists rutile (tetragonal), anatase (tetragonal) and brookite (orthorhombic). Rutile is only stale form at all temperatures and pressures, whereas, anatase and brookite are metastable and they can be transformed to rutile when heated. This transformation to rutile cannot identify a unique temperature [34, 35, 41, 42]. The crystal structures of rutile, anatase and brookite are shown in **Figure 5** [43, 44].
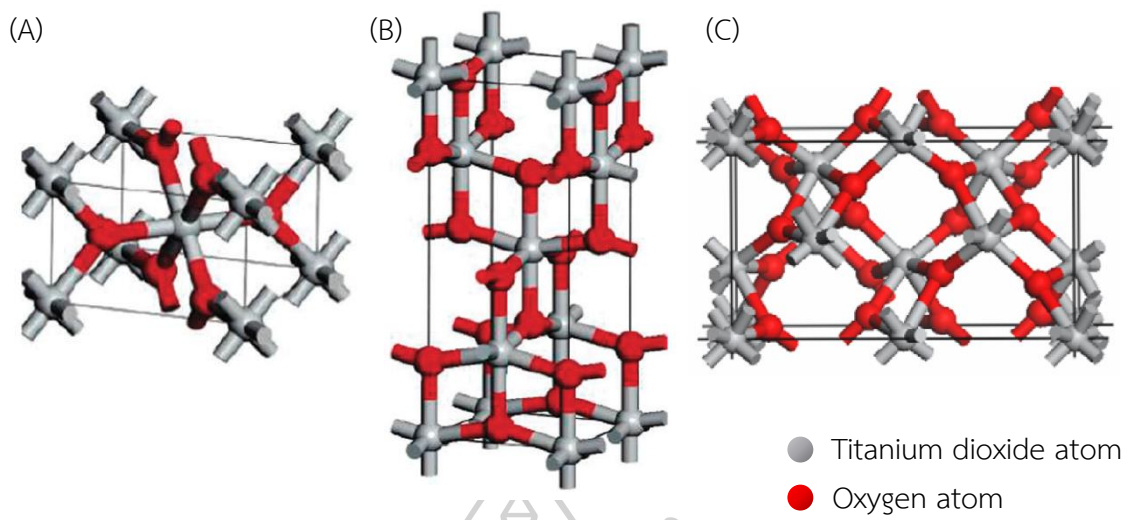
Figure 5 Crystal phases of rutile (A), anatase (B) and brookite (C) [43, 44].

CHAPTER III

LITERATURE REVIEWS

3.1 Chi-alumina (χ-Al_2O_3)

Alumina is considered to be one of the most interesting materials because of its special chemical, physical and catalytic properties, besides it is excellent thermal stability with high melting point as 2,050°C. Thereby, the alumina have used extensively such as ceramics, ceramic coating, protective barriers, wear-resistance materials, filters, crucibles, absorbents, catalysts, catalyst supports and soft abrasives [5, 20-24]. The alumina can be produced from five crystalline aluminum hydroxide precursors that consists bayerite, nordstrandite, diaspore, gibbsite and boehmite. These alumina precursors can be transformed to various metastable structures which the structures of each alumina depend on temperature of transition [22, 24]. Several alumina research commonly used gibbsite as alumina precursor. The transition of alumina structures from gibbsite is separated to two routes: [6, 45, 46]

$$
\begin{array}{c}
\text{Gibbsite} \xrightarrow{>250°C} \chi\text{-}Al_2O_3 \xrightarrow{>650°C} \kappa\text{-}Al_2O_3 \xrightarrow{>800°C} \alpha\text{-}Al_2O_3 \\
\downarrow \\
\text{Boehmite} \xrightarrow{>300°C} \gamma\text{-}Al_2O_3 \xrightarrow{>700°C} \delta\text{-}Al_2O_3 \xrightarrow{>800°C} \theta\text{-}Al_2O_3 \xrightarrow{>850°C} \alpha\text{-}Al_2O_3.
\end{array}
$$
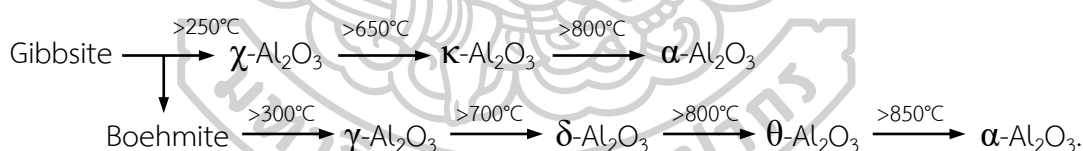
A. Tonejc et al. [46] used gibbsite as starting material for transformation to α-Al_2O_3. They found that the gibbsite could transform to χ-Al_2O_3 when heated at 500°C, κ-Al_2O_3 at 800°C and α-Al_2O_3 at 1,300°C. Chang P.-L. et al. [45] also said that gibbsite was heating treatment for produce χ-Al_2O_3 at 600°C then χ-Al_2O_3 was transformed to κ-Al_2O_3 at 1,000°C and κ-Al_2O_3 was formed as α-Al_2O_3 at 1,150-1,300°C. So that κ-Al_2O_3 is intermediate in formation of $\chi \rightarrow \alpha$-Al_2O_3 reaction. In addition, the alumina transition in route 1 (χ-, κ-, α-alumina) can be occurred by thermal decomposition of fine-grained gibbsite in air, whereas coarse-grained gibbsite can be transformed to

boehmite with water vapor presence or hydrothermal method and then metamorphose as γ-, δ-, θ-, α-alumina with various temperature [24, 47].

χ-Al_2O_3 is interested as catalysts and catalyst supports in several chemical reactions. Chaitree W. et al. [5] studied effect of χ-Al_2O_3 on the catalytic behavior of Co/Al_2O_3 in CO hydrogenation which χ-Al_2O_3 was prepared by thermal decomposition (χ-GB) and solvothermal method (χ-SV). They found that %Co metal dispersion of Co/χ-GB was higher than Co/χ-SV and Co/γ-Al_2O_3 respectively (Co/χ-GB > Co/χ-SV > Co/γ-Al_2O_3). Moreover, the Co/χ-GB and Co/χ-SV were higher CO conversion (both in initial and steady state), CH_4 selectivity and turnover frequency (TOF) than Co/γ-Al_2O_3. Kanezaki E. et al. [48] reported that Pd/CeO_2 supported on χ-Al_2O_3 catalyst gave excellent catalytic activity in methane oxidation reaction. Janlamool J. et al. [49] studied composition effect of χ-Al_2O_3 and γ-Al_2O_3 catalyst in ethanol dehydration to ethylene. Their results indicated that catalytic activity decreased in order as 50% χ-Al_2O_3 > 100% χ-Al_2O_3 > 70% χ-Al_2O_3 > 0% χ-Al_2O_3 at reaction temperature of 200-300°C. Observing, both catalyst mixed with χ-Al_2O_3 in γ-Al_2O_3 (70% χ-Al_2O_3 and 50% χ-Al_2O_3) and pure χ-phase alumina catalyst (100% χ-Al_2O_3) were higher catalytic conversion than pure γ-phase alumina catalyst (0% χ-Al_2O_3) at reaction temperature of 200°C. Moreover, they concluded that hexagonal close packing (hcp) of χ-Al_2O_3 structure was better catalytic conversion and ethylene yield than cubic close packing (ccp) of γ-Al_2O_3 structure. In other research, studying effect of phase composition between γ- and χ-Al_2O_3 on Pt/Al_2O_3 catalyst in CO oxidation by Meephoka C. et al. [23]. The Pt/Al_2O_3 catalysts mixed of γ- and χ-Al_2O_3 (30 - 70% χ-Al_2O_3) were higher CO conversion than without χ-Al_2O_3 catalyst whereas Pt supported on 10% χ-Al_2O_3 catalyst indicated the worst its activity. In addition, the CO oxidation activities related to amount of Pt active sites. It concludes that the χ-Al_2O_3 is interesting for used as catalyst and catalyst support. Therefore, in this research, the χ-Al_2O_3 is used as catalyst support.

3.2 CO_2 hydrogenation reaction

In present, CO_2 in atmosphere is continuously increased because expanding of world's population and industry growth, that causing global warmed up through the greenhouse effect. Therefore, reduction of CO_2 in atmosphere is urgently necessity. In several strategies. CO_2 hydrogenation to methane or CO_2 methanation is an option of Carbon Capture and Sequestration (CCS), that is capture of CO_2 in atmosphere and storage in underground. After that the CO_2 captured is utilized and converted to methane or chemical compounds [8, 9, 50]. The CO_2 methanation reaction (Eq. (1) in chapter II) is strongly exothermic, although thermodynamics favor at low temperatures. From this reason, catalyst used in the CO_2 methanation reaction should be high activity catalysts at low temperatures and enough stable to high temperatures [8].

CO_2 hydrogenation to methane is considered by using several metal catalysts, including Ni, Ru, Rh, Pt, Pd, Ir, Co and Fe carried out on various oxide supports (e.g. TiO_2, Al_2O_3, SiO_2, CeO_2, ZrO_2, MgO) [8, 12, 51, 52]. Catalysts of 3% Ru/Al_2O_3 and 20% Ni/Al_2O_3 were studied in carbon dioxide methanation reaction by Garbarino G. et al. [9]. Feed gases were mixed with 6%CO_2 and 30% H_2 diluted with 64% N_2. The catalysts were reacted with increasing temperature from 523 to 773 K and step back to 523 K. They reported that CO_2 conversion of Ru/Al_2O_3 was almost zero at low temperature (523 – 573 K), then CO_2 conversion and CH_4 yield increased at 623 - 673 K that was effect of conditioning. Moreover, CO_2 conversion and CH_4 yield in decreasing temperature steps were higher than in increasing step at same temperature. These results confirmed that the conditioning affected to activities of catalysts. In addition, CO_2 conversion and CH_4 yield of Ni/Al_2O_3 was clearly lower than that of Ru/Al_2O_3, concluding that Ru/Al_2O_3 catalyst was more active than Ni/Al_2O_3 catalyst. Activities of Ru and Ni supported on SiO_2 catalysts in CO_2 methanation reaction were studied by Fujita S.-I. et al. [53]. CO_2 conversion of 5.0 wt.% Ru/SiO_2 was higher than that of 8.2 wt.% Ni/SiO_2 as 3.2% and 1.0%,

respectively. The same results considered in rate of methane formation, the methane formation rate of Ru/SiO_2 was obviously more than that of Ni/SiO_2 as 26.2 and 8.2 μmol/$g_{cat.}$/min. Panagiotopoulou P. [51] reported results of noble metals (as Rh, Ru, Pt and Pd) supported on TiO_2 catalysts in CO_2 hydrogenation reaction. Mixed gases of 5%CO_2 and 20%H_2 in He were used as feed gases. CO_2 conversion of Rh/TiO_2 catalyst was clearly higher than other catalysts and reached to equilibrium at about 380°C that shown in **Figure 6** in Ru/TiO_2 and Pt/TiO_2 catalysts. CO_2 conversion curves were shift to higher temperature, whereas the CO_2 conversion of Pd/TiO_2 catalyst was less than 10% albeit reaction temperature reached 440°C. In addition, methane selectivity at reaction temperature of 350°C decreased following the order of Rh > Ru > Pt > Pd, indicated that the reverse water gas shift (RWGS) reaction was strongly supported over Pt and Pd catalysts which it produced co-production compound of CO.
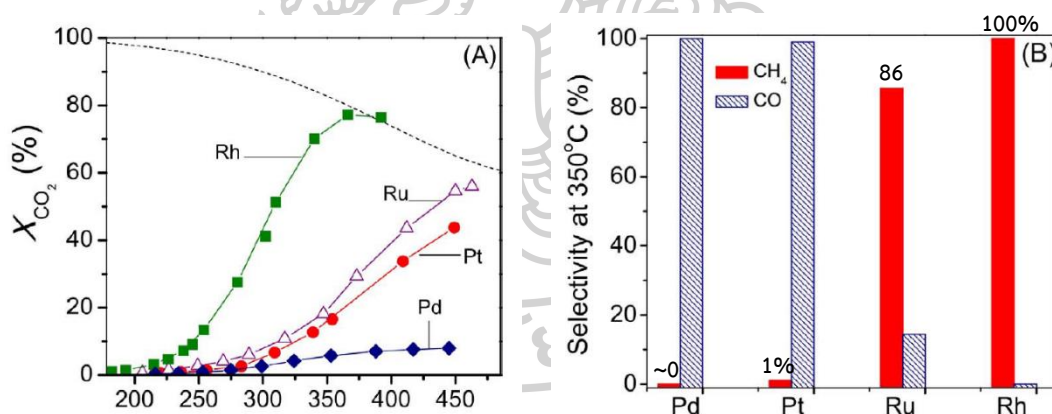
Figure 6 CO_2 conversion in a function of reaction temperatures (A), CH_4 selectivity and CO at reaction temperature of 350°C (B) [51].

Li D. et al. [54] studied Ru/TiO_2 catalysts prepared by different methods and Ru loading. In the same condition, initial rate and TOF of Ru/TiO_2 catalysts prepared by spray reaction (SPR) method were higher than those of Ru/TiO_2 catalysts prepared by impregnation (IMP) method. The spr-Ru/TiO_2 catalysts were supported by

characteristic of fine particles and new active sites creation at interface. Similarly, Ru/Al2O3 catalysts prepared by three different methods were studied by Li D. et al. [4]. The three preparation methods were consisted spray reaction (SPR), impregnation (IMP) and Hybrid (HYB) method—method of combination with spray and impregnation. The initial rate and TOF of Ru/Al_2O_3 catalysts indicated in decreasing order as spr-Ru/Al_2O_3 > imp-Ru/Al_2O_3 > hyb-Ru/Al_2O_3 catalyst. The initial rate and TOF of spr-Ru/Al_2O_3 catalyst was 2 times and 3 times higher than imp-Ru/Al_2O_3 catalyst, respectively. Reasons of the higher activities of spr-Ru/Al_2O_3 catalyst probably were its fine particle structure and homogeneity of metal and support. In addition, Li D. et al. [4] also studied impact of amount of Ru molar loading as 1%, 5%, 10% and 15% in spr-Ru/Al_2O_3 catalysts. The 5 mol% of Ru/Al_2O_3 catalyst could get the maximum initial catalytic rate and hydrogen uptake. It was concluded that the amount of Ru metal in catalyst influenced on catalytic activity per site. Kwak J.H. et al. [55] reported effect of Ru content as 0.01, 0.5, 1, 2 and 5 wt.% supported on Al_2O_3 catalysts which exhibited in **Figure 7** Catalyst 5 wt.% Ru/Al_2O_3 showed the maximum CO_2 conversion at reaction temperature of ~320°C. In decreasing amount of Ru loading, CO_2 conversion curves were shifted toward higher temperature. Interesting, CO_2 conversion of all Ru loading catalysts continuously increased and then, dropped to above ~450°C, although the amount of loading changed by a factor of 50. Whereas, CO formation profiles were quiet different and lower Ru loading catalysts were significantly higher CO rate at low temperature. Moreover, CH_4 yield increased with increasing Ru loading and temperature of maximum CH_4 yield was shift to higher temperature. From these reports, they concluded that CH_4 formation was favored in large metal clusters catalyst because CH_4 formation increased with increasing amount of Ru loading.
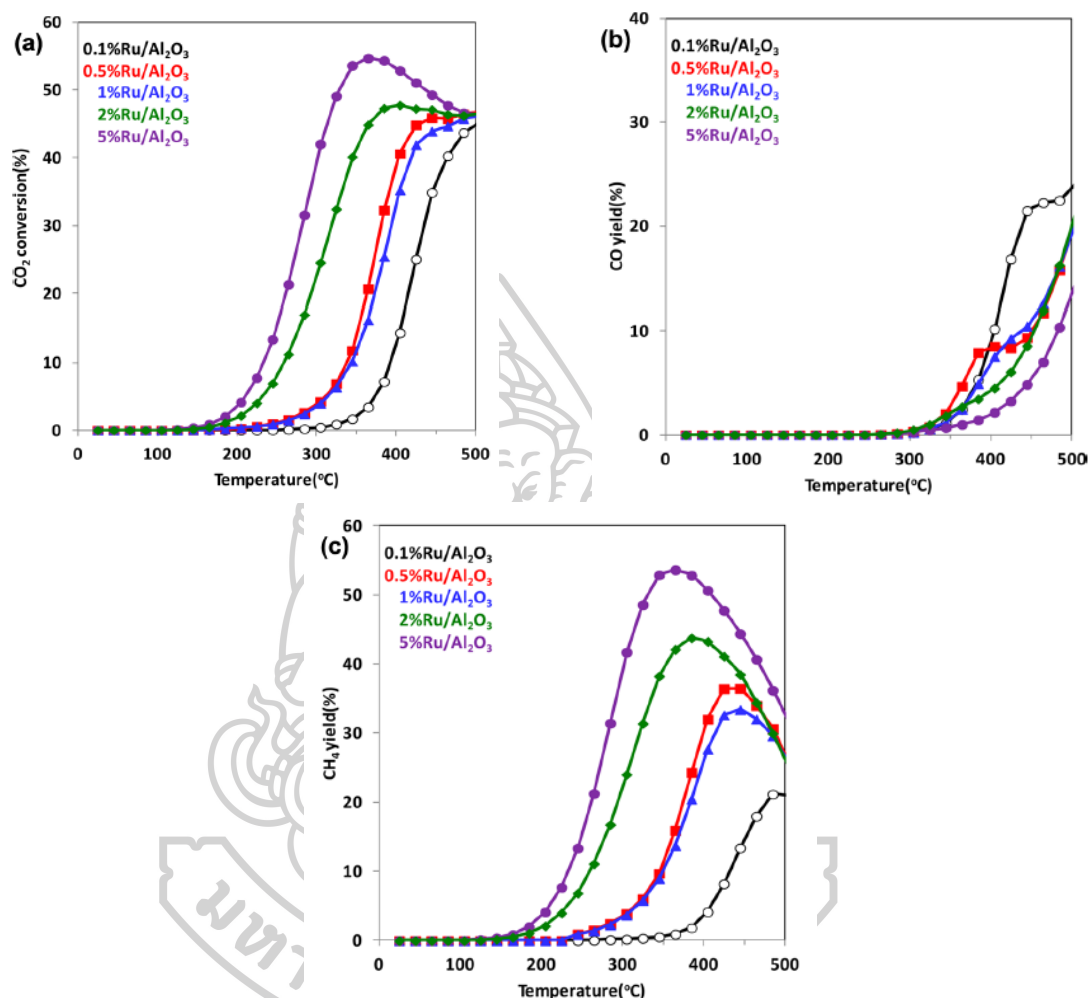
Figure 7 CO_2 hydrogenation reaction on Ru/Al_2O_3 catalyst in a function of temperature: CO_2 conversion (A), CO yield (B) and CH_4 yield (C) [55].

Supports influence to catalytic properties that consists three main features: improving of catalyst dispersion, reducing of inactive spinel phase formation, and modifying of catalytic reducibility [27]. Iizuka T. et al. [52] investigated CO_2 hydrogenation reaction over Rh catalysts supported on various metal oxides as ZrO_2, Al_2O_3, SiO_2 and MgO. The Rh/ZrO_2 indicated highest activity at all reaction

temperatures and the lowest activity was Rh/MgO. The activity of all catalysts was showed in order as $Rh/ZrO_2 > Rh/Al_2O_3 > Rh/SiO_2 > Rh/MgO$. Suo Z.-h. et al. [56] studied 5 wt.% Fe supported on TiO_2, ZrO_2 and Al_2O_3 catalysts in CO_2 hydrogenation. Reduction of catalytic activity was followed in order of $Fe/TiO_2 > Fe/ZrO_2 > Fe/Al_2O_3$. The Fe/TiO_2 gave higher CO_2 conversion (19%) and also better selectivity of C_{2+}-hydrocarbon. In addition, binary metal oxide supports were investigated in several researches. Rynkowski J.M. et al. [57] studied effect of CeO_2-Al_2O_3 binary oxide supported Ru catalysts in CO_2 methanation. 5 wt% Ru catalysts were varied CeO_2 content in CeO_2-Al_2O_3 as 10, 20 wt% CeO_2. The maximum conversion of all catalysts were followed as $Ru/20CeO_280Al_2O_3 = 76\%$, $Ru/10CeO_290Al_2O_3 = 74.5\%$ and $Ru/Al_2O_3 = 72\%$. Observing, adding CeO_2 in catalyst support gave higher activity and lower reaction temperature of maximum conversion than without CeO_2 in catalyst support. Xu J. et al. [8] interested in catalysts of binary oxide support too. They used 5 wt.% Ru catalysts supported on 5, 10, 15 wt.% TiO_2 in Al_2O_3 which those catalyst supports were compared with Ru/Al_2O_3 catalyst. CO_2 conversion as a function of reaction temperature was observed that the Ru catalysts with loading of TiO_2 were higher CO_2 conversion than Ru/Al_2O_3 catalyst that shown in **Figure 8**. At reaction temperature of 225°C, reaction rate of Ru/5 wt.% TiO_2-Al_2O_3 catalyst (0.59 molCO$_2$/gRu·h) was 3.1 times higher than that of Ru/Al_2O_3 (0.19 molCO$_2$/gRu·h) catalyst. Moreover, loading of TiO_2 in catalysts could inhibit the aggregation of RuO_2 on catalyst surface.
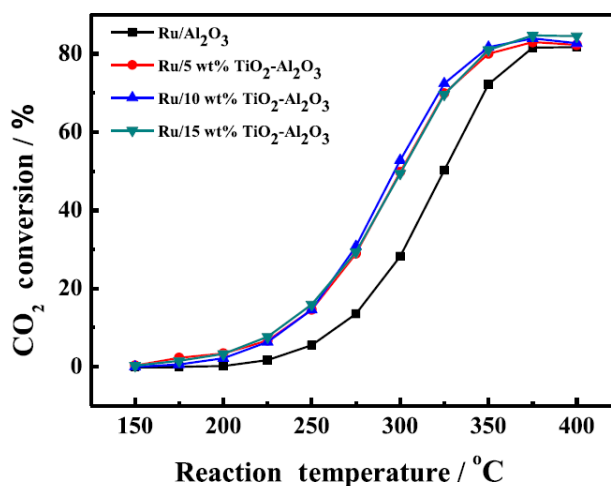
Figure 8 CO_2 conversion of various TiO_2 loading in TiO_2-Al_2O_3 binary oxide supported Ru catalysts [8].

CHATER IV

RESEARCH METHODOLOGY

4.1 Materials Preparation

4.1.1 Materials

The chemicals used in the catalytic preparation are shown in **Table 4**.

Table 4 The chemicals were prepared for synthetic of catalysts.

Chemical	Formula	Grade	Manufacture
Ruthenium (III) acetylacetonate	$Ru(C_5H_7O_2)$	97%	Sigma-Aldrich
Ruthenium (III) nitrosyl nitrate solution	$Ru(NO)(NO_3)_x(OH)_y$, $x + y = 3$	1.5% in nitric acid	Sigma-Aldrich
Hexaammineruthenium (III) chloride	$Ru(NH_3)_6Cl_3$	98%	Sigma-Aldrich
Gibbsite	$Al(OH)_3$	Technical	Sigma-Aldrich
Titanium (IV) butoxide	$Ti(OCH_2CH_2CH_2CH_3)_4$	97%	Sigma-Aldrich
Zirconium n-butoxide	$C_{16}H_{36}O_4Zr$	80% in 1-butanol	Alfa Aesar
Xylene	C_8H_{10}	AR	QReC

4.1.2 Support preparation

The chemical properties used in the preparation of support are shown in **Table 4**. The χ–Al_2O_3 support was prepared by the thermal decomposition of microcrystalline gibbsite. The gibbsite was calcined at 600℃ in tube furnace under the air flow (100 ml/min) with heating rate of 10℃/min and was hold in this temperature for 4 hours.

TiO$_2$–Al$_2$O$_3$ and ZrO$_2$–Al$_2$O$_3$ binary oxides supports were prepared using wet impregnation method. The content of TiO$_2$ in Al$_2$O$_3$ was varied as 5 wt.%, 10 wt.%, 15 wt.% and 20 wt.%, and the content of ZrO$_2$ in Al$_2$O$_3$ was varied as 2.5 wt.%, 5 wt.%, 10 wt.% and 15 wt.%. In the case of TiO$_2$–Al$_2$O$_3$ support, gibbsite was added in titanium (IV) butoxide diluted with xylene solvent. Then, the sample was heated up to 80℃ and hold in this temperature until the sample was dampened. After that, the sample was dried at 110℃ for 12 hours and calcined in air (100 ml/min) by heating up to 600℃ with rate 10℃/min for 4 hours. The ZrO$_2$–Al$_2$O$_3$ support was prepared with the same preparation procedure but zirconium n-butoxide was used as a precursor instead.

4.1.3 Catalytic preparation

χ–Al_2O_3 supported Ru catalysts was prepared by incipient wetness impregnation method with 1 wt.% of Ru loading. The Ru precursors of catalyst were varied with 3 different Ru precursors, which included ruthenium (III) acetylacetonate, ruthenium (III) nitrosyl nitrate solution and hexaammineruthenium (III) chloride. The support was impregnated with Ru precursor dissolved in solvent and kept at room temperature for 6 hours. Then, the sample was dried at 110℃ for 12 hours and calcined in air (100 ml/min) at 300℃ with heating rate of 10℃/min at 300℃ and hold in this temperature for 4 hours. The details of catalytic preparation precursor used for Ru/χ–Al_2O_3 catalysts are shown in **Table 5**.

This preparation procedure was used also to prepare TiO_2–Al_2O_3 and ZrO_2–Al_2O_3 binary oxides supported Ru catalysts. But, the Ru precursor used for preparation of Ru/TiO_2–Al_2O_3 and Ru/ZrO_2–Al_2O_3 catalysts was chose from the best of Ru/χ–Al_2O_3 catalysts.

Table 5 The details of preparation precursors of Ru/χ–Al_2O_3 catalysts.

Support	Ru precursor	Solvent
χ–Al_2O_3	Ruthenium (III) acetylacetonate	Xylene
	Ruthenium (III) nitrosyl nitrate solution	Deionized Water
	Hexaammineruthenium (III) chloride	Deionized Water

4.2 Catalytic activity test

The catalytic activity test was performed by CO_2 hydrogenation reaction. In addition, the flow diagram of this system is shown in **Figure 9**.
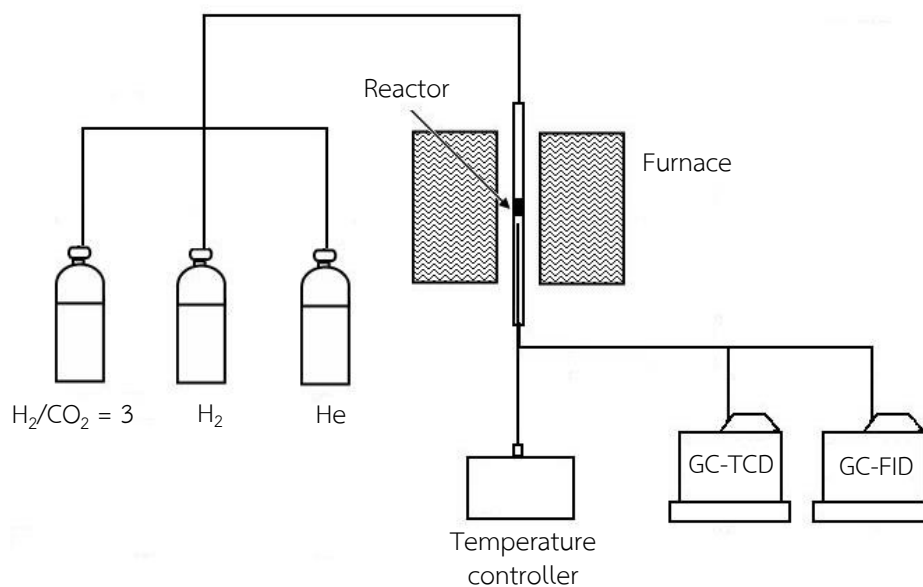
Figure 9 The flow diagram of operating system of CO_2 hydrogenation.

The activity test of the catalysts in CO_2 hydrogenation reaction was performed in a continuous-flow fixed-bed reactor with the inner diameter of 7.1 mm (stainless steel) under atmospheric pressure. 0.15 ml of catalyst powder was loaded in reactor, and then, reduced in H_2 with 30 ml/min at 400°C for 2 hours before starting the reaction. The reaction was carried out using temperature programmed reaction method (250, 275, 300, 325, 350, 375, 400 and 425°C), which increased continuously by 25°C per hour. The gas mixture of H_2/CO_2 = 3 and balanced with helium (CO_2+H_2 = 20 ml/min and He = 20 ml/min) was used as the feed gases for reaction with the catalysts prepared by different Ru precursors. In addition, H_2/CO_2 = 4 balanced with helium (CO_2+H_2 = 20 ml/min, H_2 = 5 ml/min and He = 15 ml/min) as feed gas were used for the reaction of Ru/ZrO_2 and Ru/TiO_2 catalysts. GHSV used in the reaction was at 14,000 h^{-1}. The gas products out of the reactor were measured by using gas chromatograph (SHIMADZU GC-14B) with a TCD and FID detector. The operating conditions of GC-TCD and GC-FID detectors are shown in **Table 6** and **Table 7**, respectively.

Table 6 The operating conditions of GC-TCD detector used for catalytic activity test.

Gas chromatograph	SHIMADZU GC-14B
Detector	TCD
Column	Porapack Q
Carrier gas	He
Carrier gas flow	30 ml/min
Injector temperature	150°C
Detector temperature	150°C
Column temperature	40°C

Analysis gas	CO_2, CO, CH_4

Table 7 The operating conditions of GC-FID detector used for catalytic activity test.

Gas chromatograph	SHIMADZU GC-14B
Detector	FID
Column	DB-1
Carrier gas	N_2
Split flow rate	40 ml/min
Purge flow rate	10 ml/min
Carrier pressure	40 kPa
Make up pressure	50 kPa
Injector temperature	200℃
Detector temperature	200℃
Column temperature	40℃
Analysis gas	Hydrocarbons

4.3   Catalytic characterization

In this research, the characterization of catalysts was determined using techniques of X-ray diffraction (XRD), N_2 physisorption (BET), H_2 chemisorption, Temperature programmed reduction (TPR) and Transmission electron microscope (TEM).

4.3.1 X-ray diffraction (XRD)

X-ray diffraction (XRD) is a technique that used to study crystalline structure of catalysts. XRD patterns were recorded using a Siemens D5000 X-ray diffractometer and Cu K$_\alpha$ radiation with a Ni filter. The range of 2θ was from 20° to 80°. The crystallite size was calculated using Scherrer's equation.

4.3.2 N$_2$ physisorption (BET)

The specific surface area, average pore size and pore volume of catalysts were measured by nitrogen gas adsorption-desorption at liquid nitrogen temperature (-196ºC) using a BET SORP mini II. The catalysts were pretreated in helium gas at 180ºC for 3 hours.

4.3.3 H$_2$ chemisorption

The H$_2$ chemisorption technique was performed to measure the active site, dispersion and particle size of Ru metal, by using a Micrometics AutoChem 2910 instrument. Prior to measurement, 60 mg of catalyst sample was reduced in H$_2$ gas (25 ml/min) at 400ºC for 2 hours. Then, the reduced sample was cooled down to 100ºC and measured at this temperature using N$_2$ carrier gas. 50 μl of H$_2$ gas was injected in the form of a pulse into instrument until amount of H$_2$ measured was constant.

4.3.4 Temperature programmed reduction (TPR)

The reduction behavior and reducibility of catalyst were obtained from Temperature programmed reduction (TPR) experiment using a Micrometritics AutoChem 2910 instrument. Prior to H$_2$-TPR experiment, about 100 mg of catalyst sample was loaded into a U-shape quartz reactor and then, pretreated with N$_2$ gas (30 ml/min) at 200ºC with heating rate of 10ºC/min for 1 hour to remove the adsorbed water. After pretreatment, the pretreated sample was cooled to room temperature. Then, 10% H$_2$ in N$_2$ (30 ml/min) was flowing through the sample and heated up to 800ºC with rate of 10ºC/min.

4.3.5 Transmission electron microscope (TEM)

The morphology of catalyst sample was determined by Phillips Tecni 20 and operated at 120 kV.

CHAPTER V

RESULTS AND DISCUSSION

In this chapter, the story is divided into four major sections, which consists: 1) effect of different ruthenium precursors in Ru/χ-Al$_2$O$_3$ catalyst, 2) effect of ZrO$_2$ addition in χ-Al$_2$O$_3$ supported Ru catalyst, 3) effect of TiO$_2$ addition in χ-Al$_2$O$_3$ supported Ru catalyst and then 4) Comparison of catalytic activity of ZrO$_2$-Al$_2$O$_3$ and TiO$_2$-Al$_2$O$_3$ supported Ru catalysts. The first three major sections describe about characterization of catalyst which analyzed by five techniques, viz., N$_2$ physisorption (BET), transmission electron microscope (TEM), X-ray diffraction (XRD), H$_2$ chemisorption and temperature programmed reduction (TPR) techniques.

In addition, CO$_2$ hydrogenation reaction with temperature programmed is considered for catalytic activity investigation. Feed gases used in this reaction contain 12.5% CO$_2$ and 37.5% H$_2$ with He balanced for section one, and 12.5% CO$_2$ and 50% H$_2$ with He balanced for section two and three. GHSV specified is 14,416 h^{-1}.

5.1 Effect of different ruthenium precursors in Ru/χ-Al$_2$O$_3$ catalyst

In this section, the Ru/χ-Al$_2$O$_3$ catalysts prepared by incipient wetness impregnation method using three different ruthenium precursors are investigated. The three different ruthenium precursors included ruthenium (III) nitrosyl nitrate solution, ruthenium (III) acetylacetonate and hexaammineruthenium (III) chloride. The catalysts prepared by these precursors denoted as RNN, RAA and RCl, respectively. The amount of ruthenium loading is 1 wt.%.

5.1.1 Catalytic characterization

BET surface area, total pore volume and average pore size diameter of RNN, RAA and RCl catalysts are shown in **Table 8**. The BET surface area of RAA catalyst (192 m^2/g) is higher than two other catalysts. When consider the different ruthenium precursor catalysts, the BET surface area of RNN (171 m^2/g) and RCl catalysts (155 m^2/g) are lower than that of RAA, respectively. In addition, the RAA catalyst is highest pore volume (0.91 cm^3/g). The pore volume of both of the RNN and RCl catalysts are same value (0.21 cm^3/g).

Table 8 BET surface area, pore volume, pore diameter, isotherm type and hysteresis loop type of Ru/χ-Al$_2$O$_3$ catalysts prepared with three different ruthenium precursors.

Catalyst	BET surface area [m^2/g]	Pore volume [cm^3/g]	Pore diameter [nm]	Type of isotherm	Type of hysteresis loop
RNN	171	0.21	5.0		
RAA	192	0.91	4.0	IV(a)	H2(b)
RCl	155	0.21	5.5		
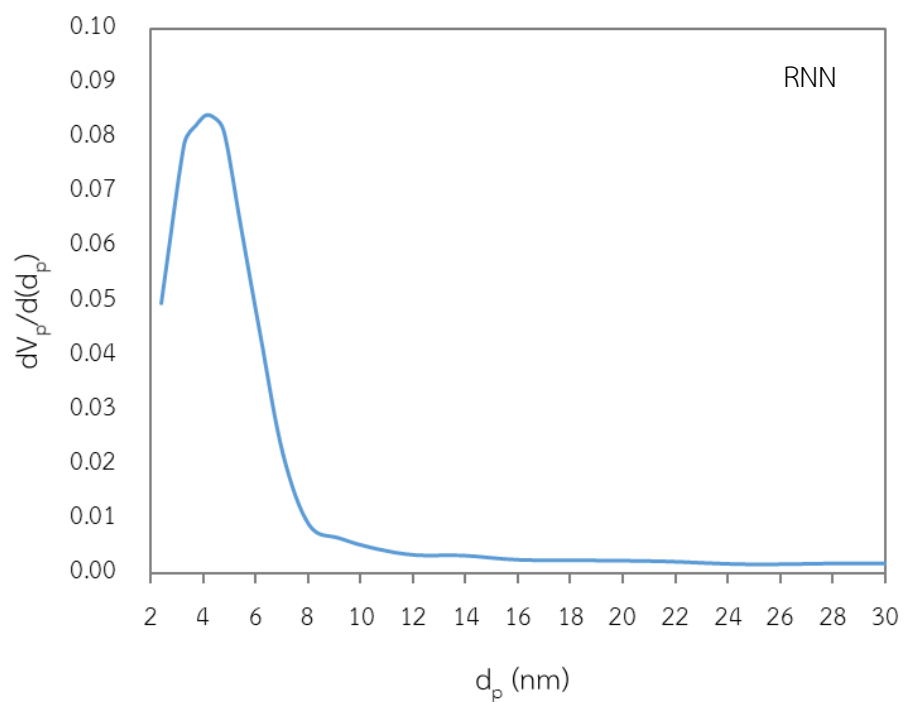
Figure 10 Pore diameter distribution of RNN catalyst.
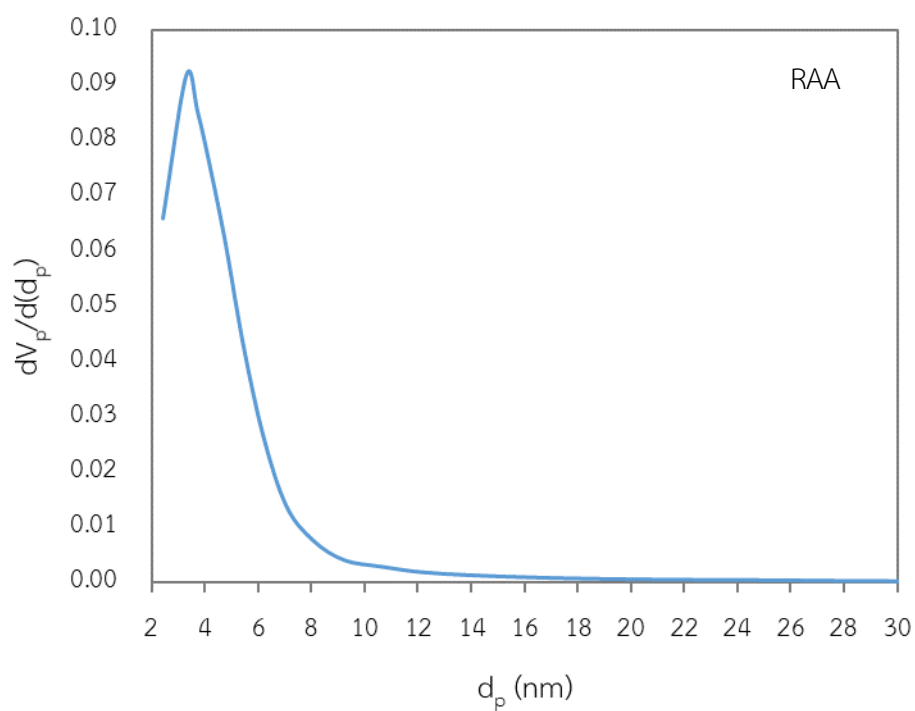
Figure 11 Pore diameter distribution of RAA catalyst.
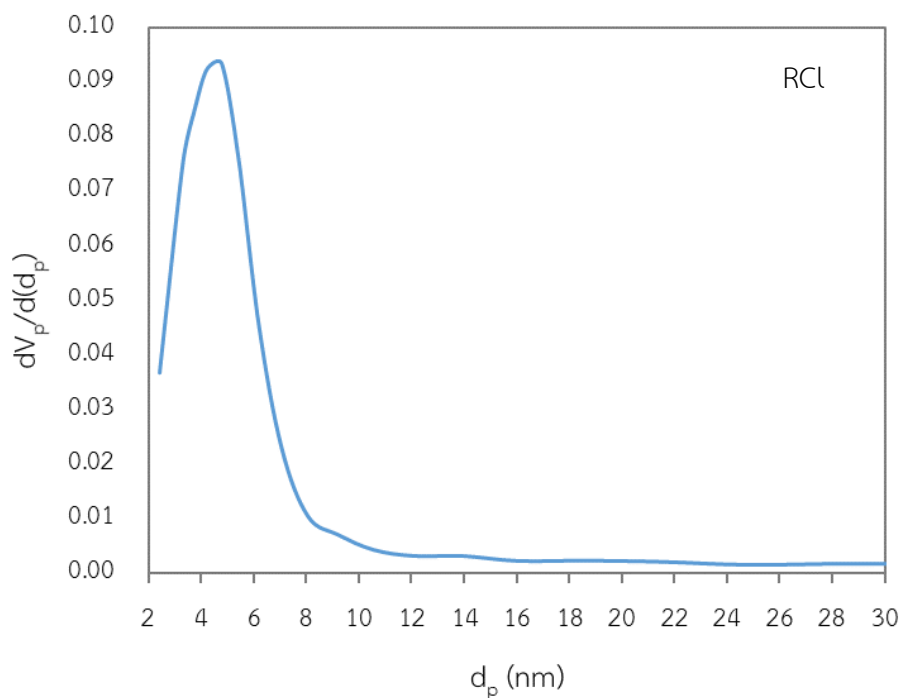
Figure 12 Pore diameter distribution of RCl catalyst.

Pore diameter distribution of RNN, RAA and RCl catalysts analyzed by using BJH method are shown in **Figure 10 – 12**. All catalysts exhibited the very uniform narrow distribution curve. The pore diameter in descending sort is RCl (5.5 nm), RNN (5.0 nm) and RAA (4.0 nm), respectively. In addition, pore structure of all catalyst is mesopore that is confirmed in isotherm and hysteresis description.

The physisorption isotherms of RNN, RAA and RCl are exhibited in **Figure 13 – 15**, respectively. The physisorption isotherms of these catalysts are assigned as that in type IV(a). This type indicate that the catalysts have characteristic as mesoporous structure. In addition, the porous catalysts are cylindrical porous structure which described by hysteresis loop of type H2(b) [58]. The hysteresis loops are also shown in **Figure 13 – 15**.
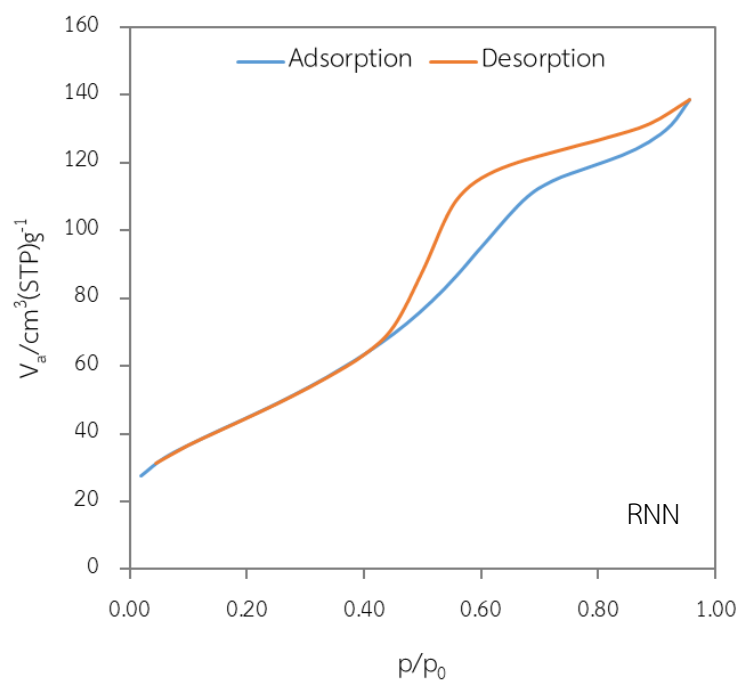
Figure 13 N_2 adsorption and desorption isotherm of RNN catalyst.
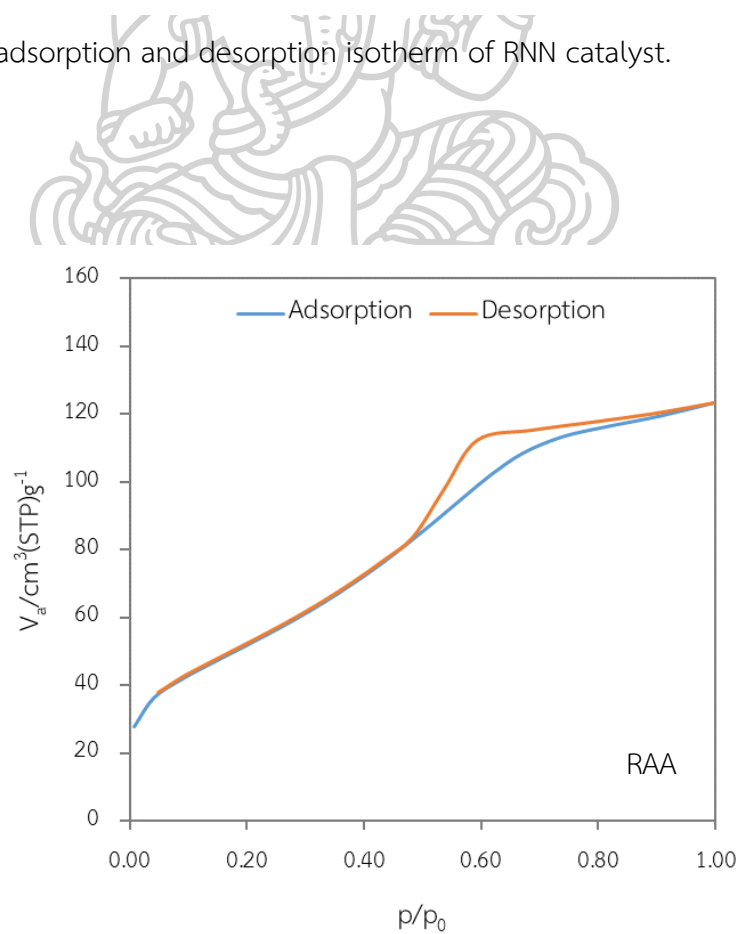
Figure 14 N_2 adsorption and desorption isotherm of RAA catalyst.
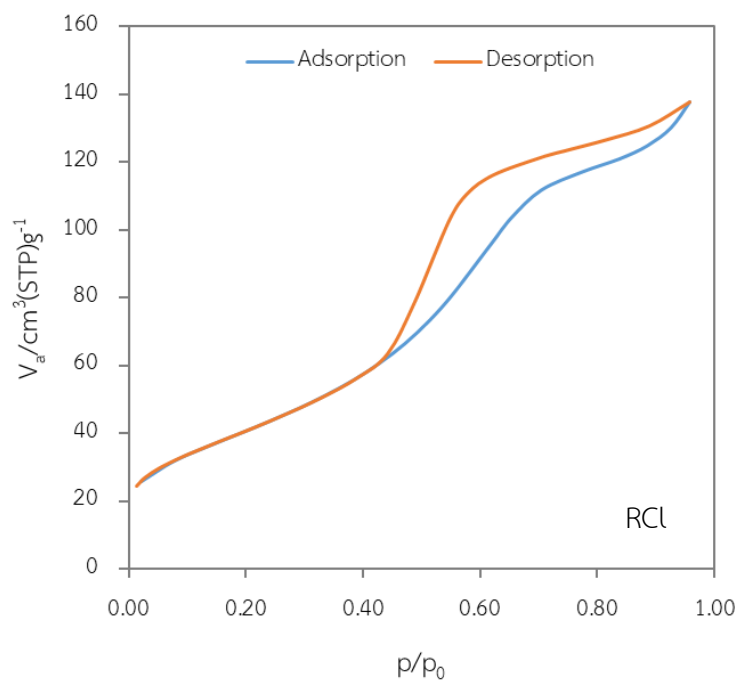
Figure 15 N$_2$ adsorption and desorption isotherm of RCl catalyst.

Figure 16 shows the XRD pattern of RNN, RAA and RCl catalysts. From all catalysts, the main diffraction peaks of RuO$_2$ is appeared at 2θ = 28°, which is the same peak observed by Li D. et al. [4]. The RuO$_2$ peak intensity of RNN and RAA catalysts is much sharper comparing with RCl catalyst, which almost does not appear. In addition, the diffraction peak intensity of χ-Al$_2$O$_3$ are also observed in all Ru/χ-Al$_2$O$_3$ catalysts prepared by using various Ru precursors. The crystallite size of all species in RNN, RAA and RCl catalysts is calculated by using the Scherrer equation and the results are shown in **Table 9**. It clearly showed that RuO$_2$ crystallite size of RCl catalyst (24 nm) is smaller than the crystallite size of RNN and RAA catalysts (31 and 37 nm, respectively). These results are contributed with XRD results by Nurunnabi, M., et al. [59] which they investigate in effect of Ru precursors on Ru/Al$_2$O$_3$ catalyst. They found that RuO$_2$ crystallite size of Ru/Al$_2$O$_3$ prepared by RuCl$_3$·nH$_2$O precursor was smaller than the catalyst prepared by Ru(NO$_3$)$_3$(NO) and acetone solution of Ru(C$_5$H$_7$O$_2$)$_3$ precursors, respectively. In an observation of Al$_2$O$_3$ crystallite size, the size of all three catalysts are not much different.
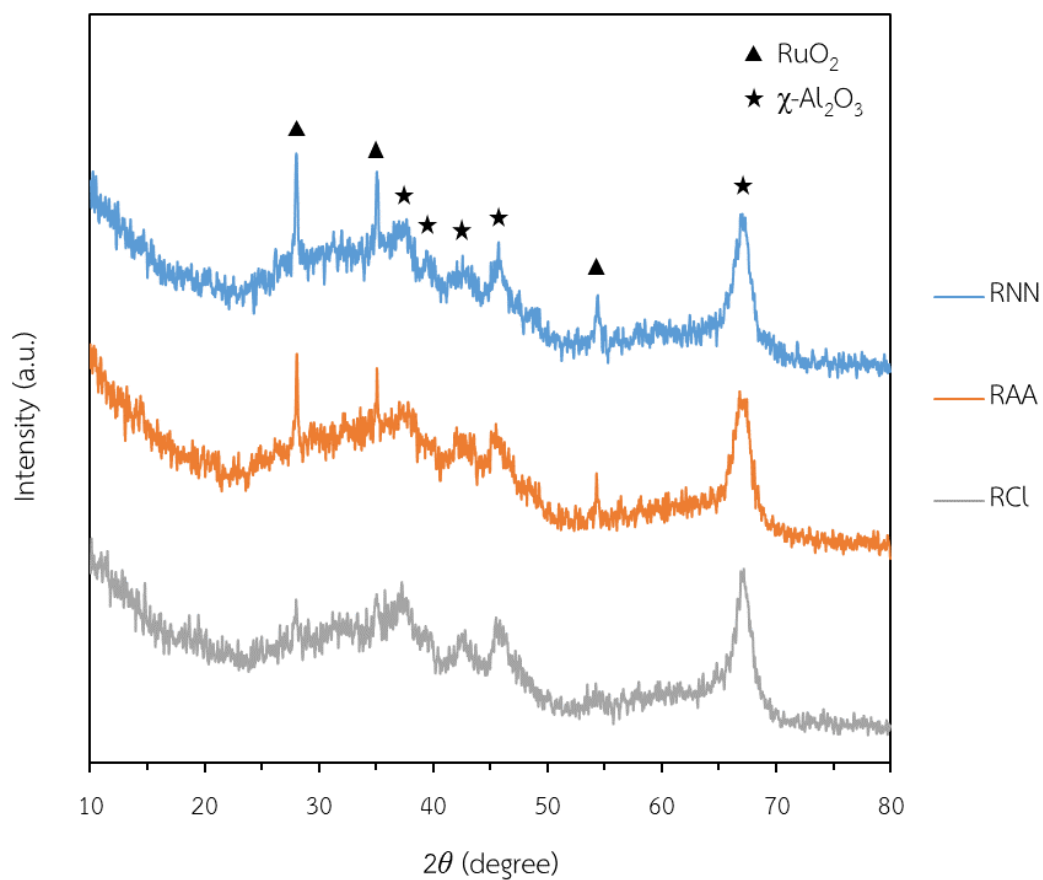
Figure 16 XRD pattern of RNN, RAA and RCl catalysts.

Table 9 Crystallite size of RNN, RAA and RCl catalysts calculated by XRD results.

Catalyst	Crystallite size (nm)	
	RuO_2	Al_2O_3
RNN	31	6.3
RAA	37	5.9
RCl	24	6.4

Particle morphology of RNN, RAA and RCl catalysts observed by TEM technique are shown in **Figure 17**. In the TEM images, RuO_2 particles exhibited as deep black color. The RuO_2 particles of RNN catalyst were obviously larger than that of RCl catalyst and the RuO_2 particle shape of both catalysts cannot be identified in geometric form. In RAA catalyst, the RuO_2 was very large particle. Moreover, part of the RuO_2 particles in RAA catalyst were similar to crystalline rods. It is seemly that the above description has the same tendency as the XRD results. In addition, the RuO_2 particles of all three catalysts are quite poorly dispersed on χ-Al_2O_3 support and it is like to cluster form.

Amount of active site, Ru metal dispersion and Ru particle size of RNN, RAA and RCl catalysts are displayed in **Table 10**. The active site of RNN catalyst (3.0 μmol/g_{cat}) was higher than that of RAA catalyst (2.1 μmol/g_{cat}). In the Ru dispersion results, Ru dispersion of RNN catalyst as 3.0% was higher than Ru dispersion in RAA catalyst as 2.1%. This means that Ru metal from ruthenium (III) nitrosyl nitrate precursor dispersed on χ-Al_2O_3 support is better than Ru metal from ruthenium (III) acetylacetonate precursor. In addition, average Ru particle size of RNN catalyst is smaller than Ru particle size of RAA catalyst as 30 and 43 nm, respectively. Interestingly, results of active site, Ru metal dispersion and Ru particle size in RCl catalyst cannot be measured that probably due to existence of chlorine residual. Murata S. et al. [60] explained reason for low dispersion and low activity of Ru/Al_2O_3 catalyst prepared from $RuCl_3 \cdot 3H_2O$ precursor that because of chlorine residual. Moreover, when chlorine removed by hydrogen treatment at high temperature and washing in ammonia solution, the activity of this catalyst was increased about four times.
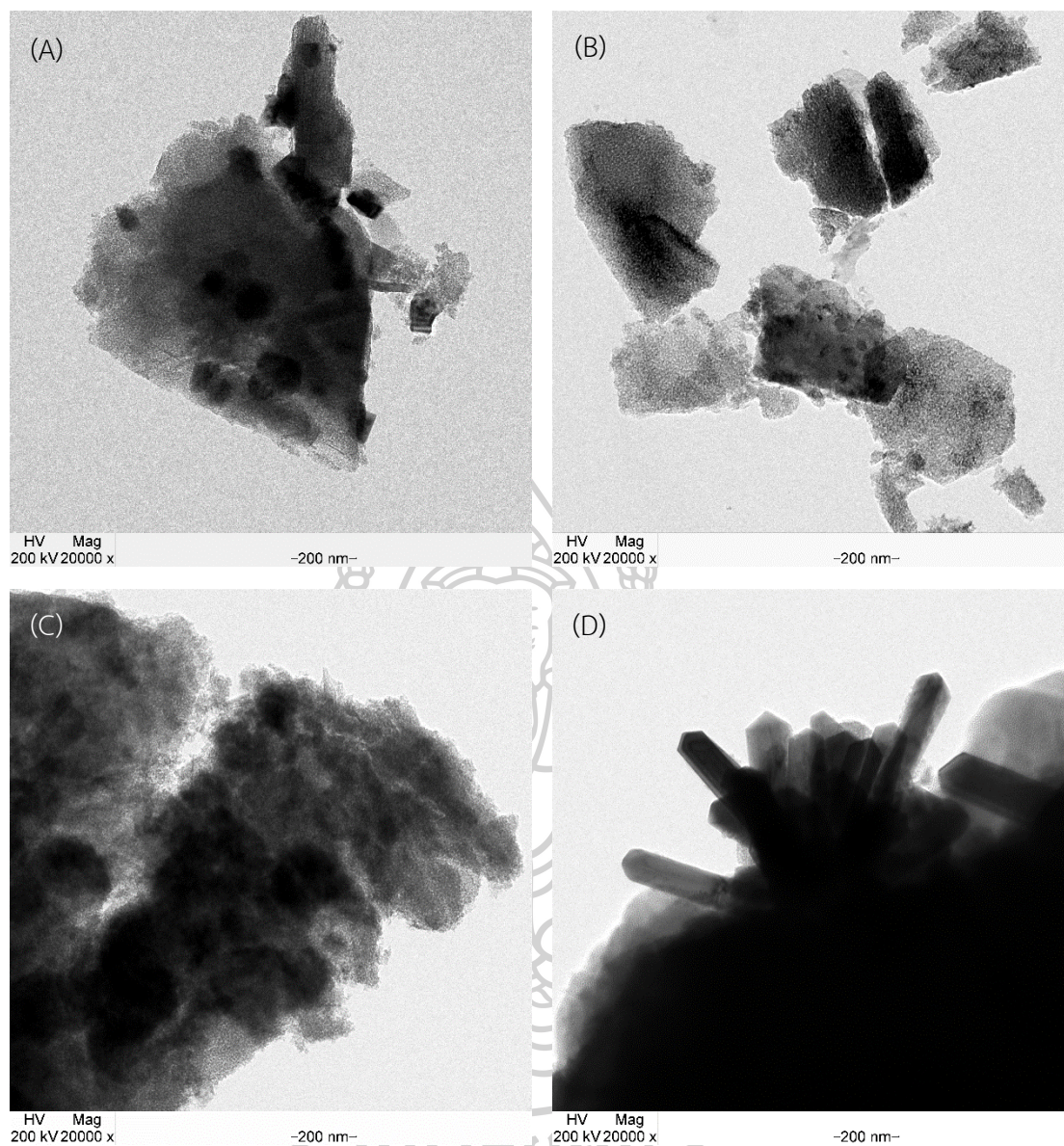
Figure 17 TEM images of Ru/χ-Al₂O₃ catalysts seeing that (A) RNN catalyst, (B) RCl catalyst and (C), (D) RAA catalyst.

Table 10 H$_2$ chemisorption results of RNN, RAA and RCl catalysts.

Catalyst	Active site [μmol/g$_{cat.}$]	Ru dispersion [%]	Average diameter of Ru particles [nm]
RNN	3.0	3.0	30
RAA	2.1	2.1	43
RCl	N/A	N/A	N/A
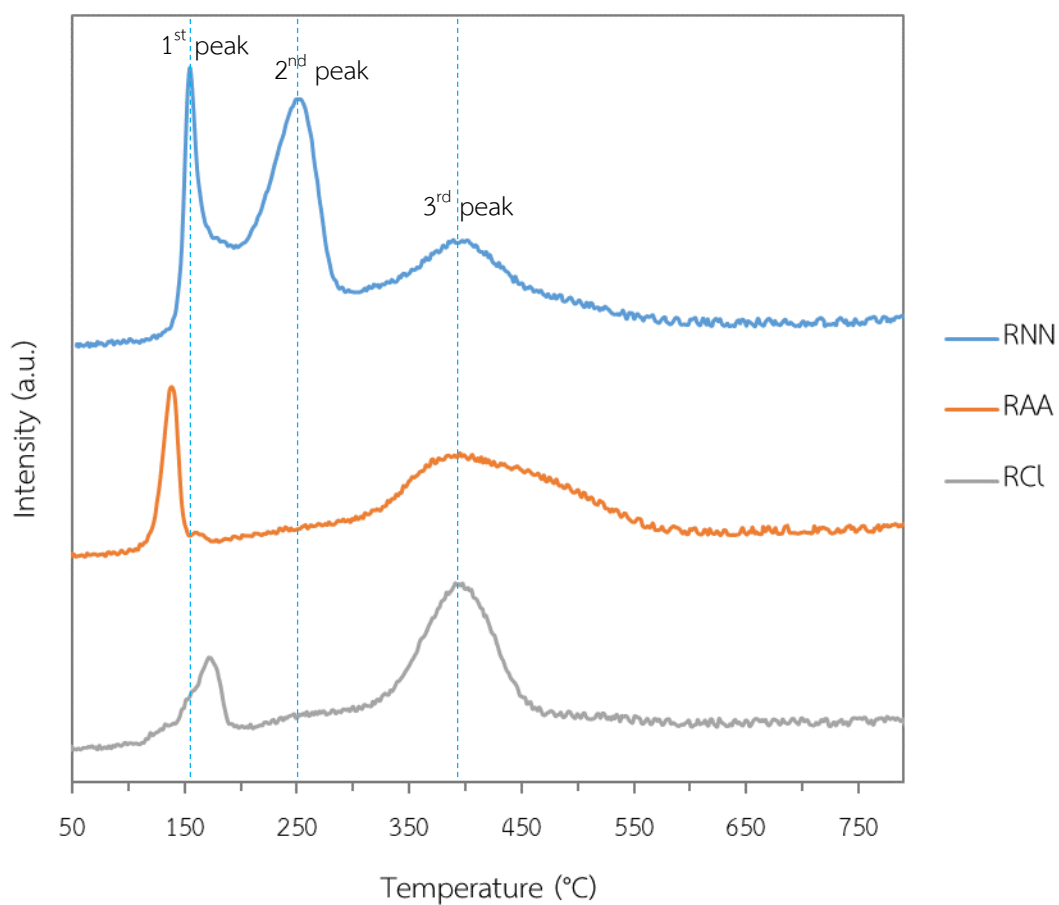
Figure 18 H$_2$-TPR profiles of RNN, RAA and RCl catalysts.

Figure 18 indicates H_2-TPR profiles of RNN, RAA and RCl catalysts. These results were composed of a sharp low temperature reduction peak at about 154 – 173°C, a medium temperature reduction peak at about 241 – 267°C, and a broad high temperature reduction peak at about 392 – 395°C. In literatures discovered [59, 61-63], the first peak and second peak were attributed to reduction step from RuO_2 to RuO and RuO to Ru^0, respectively. Then, third peak at high reduction temperature can be assigned to reduction of Ru species oxidized that strongly interact with χ-Al_2O_3 support.

5.1.2 Catalytic activity test

CO_2 hydrogenation reaction is investigated with Ru/χ-Al_2O_3 catalysts prepared by using three different Ru precursors. Feed gases mixed of H_2/CO_2 as 3/1 with He balanced and GHSV as 14,416 h^{-1} are used in this investigation. Temperature programed CO_2 conversion of RNN, RAA and RCl catalysts is indicated in **Figure 19**. CO_2 conversion profiles of RNN and RAA catalysts are little different while that of RCl catalyst was significantly lower than other two catalysts for all reaction temperatures. Reason of lower CO_2 conversion in RCl catalyst might be the presence of chlorine residual that caused the overlaid of active catalyst by chlorine [60]. In addition, Ru catalyst supported on commercial γ-Al_2O_3 was used to compare with RNN. Both catalysts were prepared by using same Ru precursor as ruthenium (III) nitrosyl nitrate precursor. The Ru/Al_2O_3 (Commercial) catalyst can get maximum CO_2 conversion at lower reaction temperature at 350°C than that of RNN catalyst. Besides, CO_2 conversion of Ru/Al_2O_3 (Commercial) catalyst decreased when increasing toward high reaction temperature probably due to the catalytic deactivation.

Plot between CH_4 selectivity and reaction temperature is shown in **Figure 20**. The CH_4 selectivity of RNN and RAA catalysts was almost 100%, whereas, the CH_4 selectivity of RCl is less than that of all catalysts at every reaction temperature. The result suggests that the RCl catalyst promotes production of CO. Plot between CH_4 yield and CO yield with reaction temperature are exhibited in **Figure 21 and 22**. The CH_4 yield profile of RCl catalyst was lower than that of RNN and RAA catalysts, and RCl catalyst gave the most CO yield of all catalysts. The CH_4 yield of Ru/Al_2O_3 (Commercial) catalyst was higher than RNN catalyst at low reaction temperature, whereas, at high reaction temperature, the CH_4 yield of Ru/Al_2O_3 (Commercial) catalyst decreased and the CO yield of Ru/Al_2O_3 (Commercial) catalyst increased and then it was overtaking by RNN and RAA catalyst.
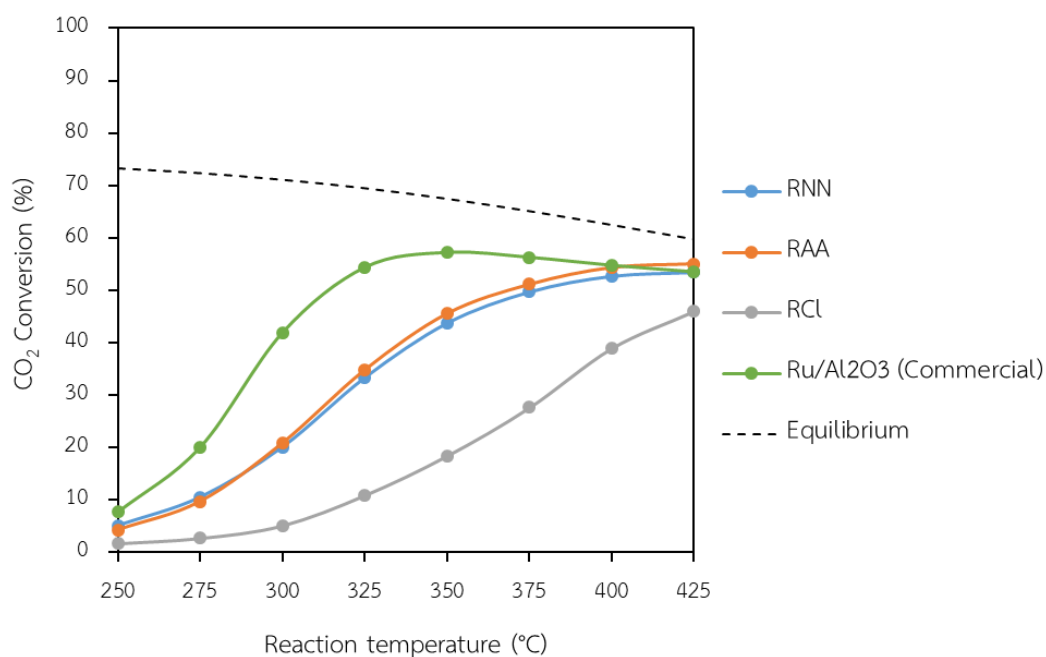
Figure 19 CO_2 conversion as function of reaction temperature of RNN, RAA, RCl and Ru/Al_2O_3 (Commercial) catalysts.
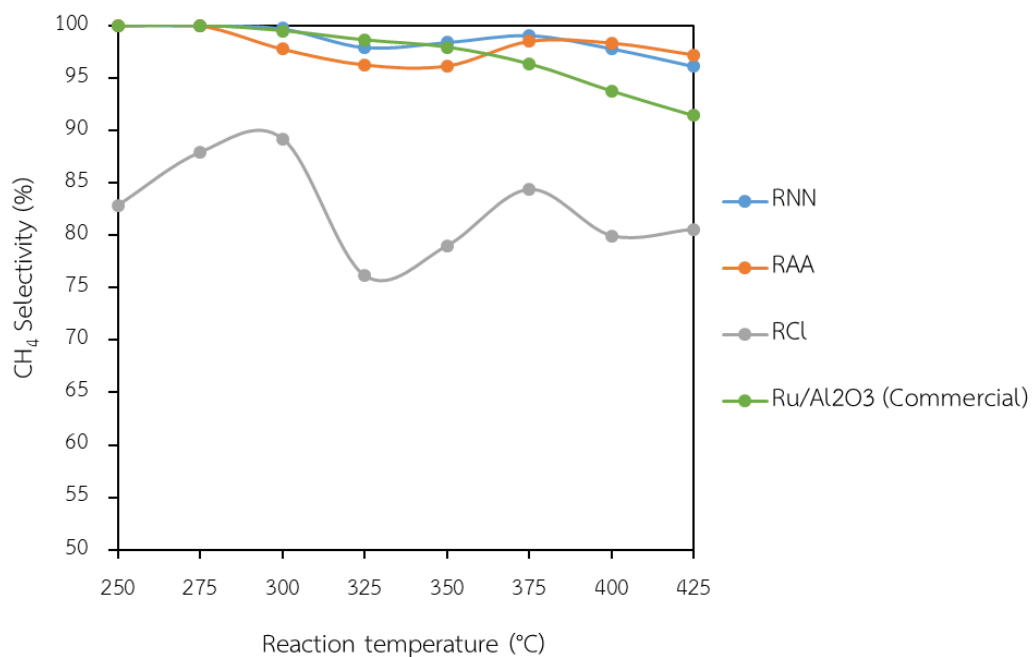
Figure 20 CH$_4$ selectivity as function of reaction temperature of RNN, RAA, RCl and Ru/Al$_2$O$_3$ (Commercial) catalysts.
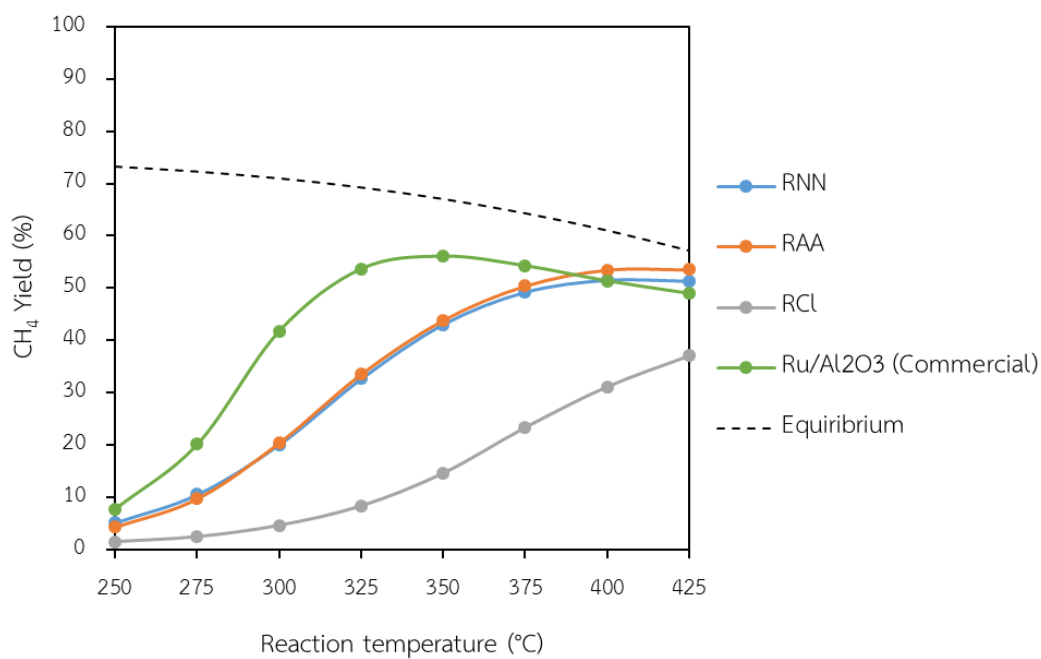
Figure 21 CH$_4$ yield as function of reaction temperature of RNN, RAA, RCl and Ru/Al$_2$O$_3$ (Commercial) catalysts.
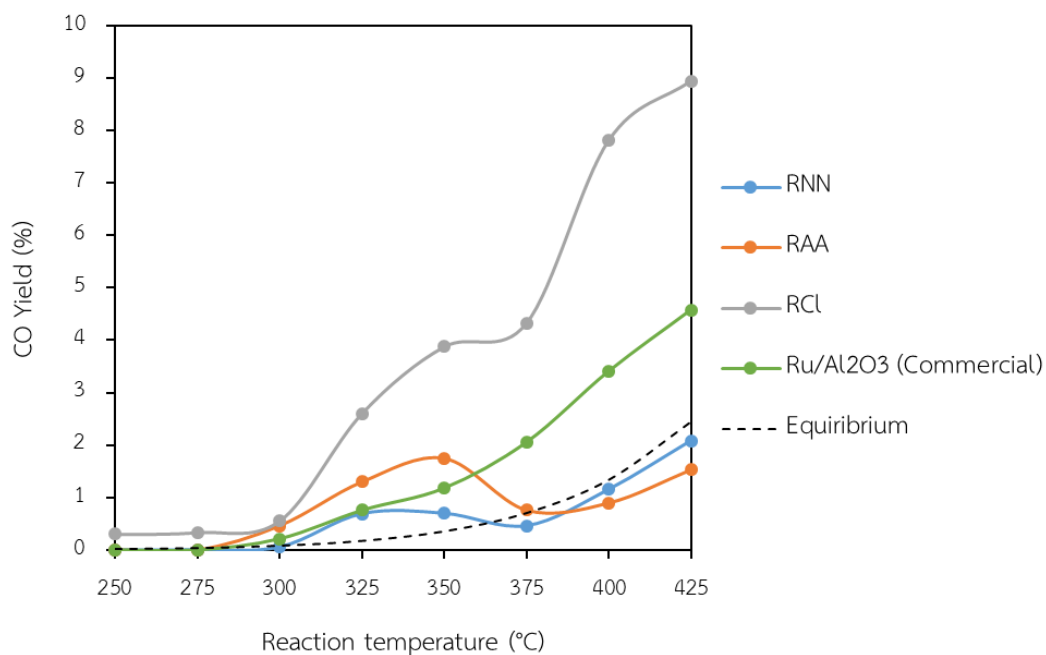
Figure 22 CO yield as function of reaction temperature of RNN, RAA, RCl and Ru/Al$_2$O$_3$ (Commercial) catalysts.
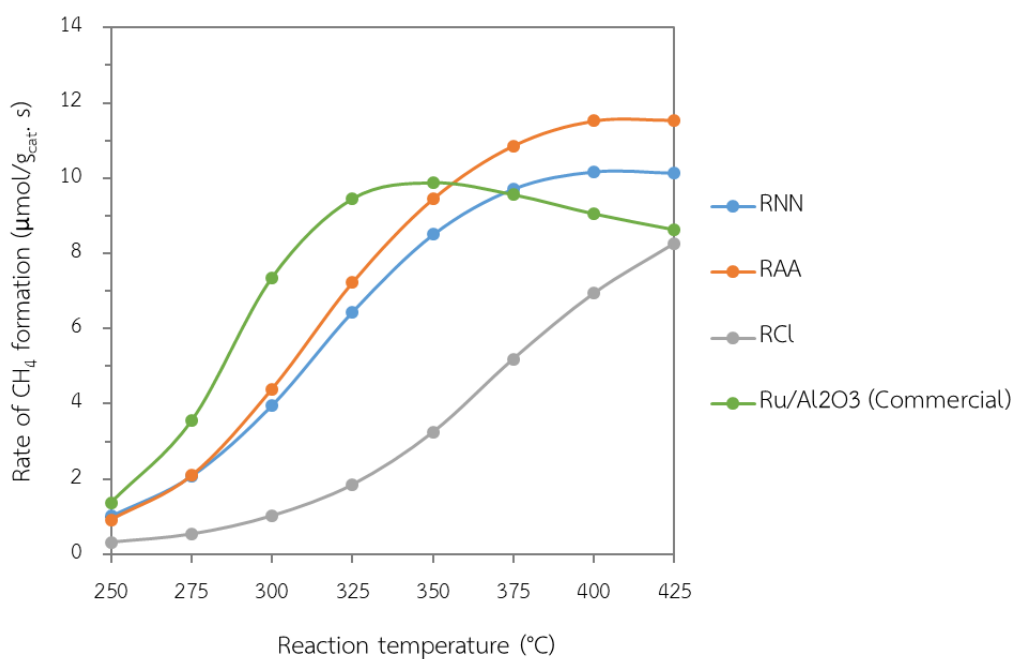
Figure 23 Rate of CH$_4$ formation as function of reaction temperature of RNN, RAA, RCl and Ru/Al$_2$O$_3$ (Commercial) catalysts.
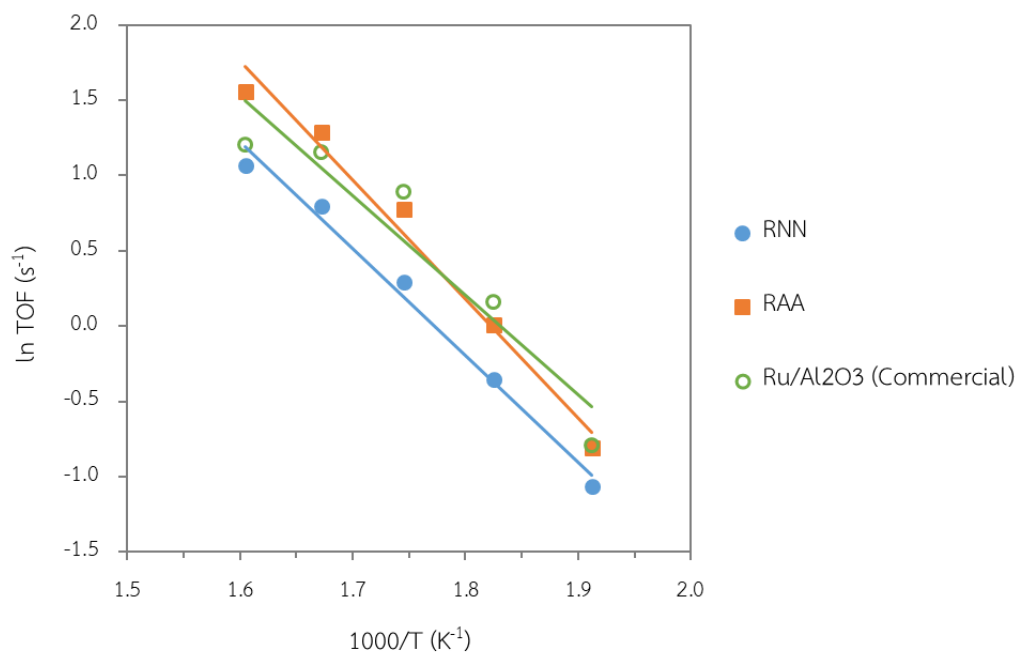
Figure 24 Turnover frequency (TOF) of CO_2 conversion obtained from RNN, RAA, RCl and Ru/Al$_2$O$_3$ (Commercial) catalysts.

Table 11 Apparent activation energy (E_a) of CO_2 hydrogenation reaction obtained from RNN, RAA, RCl and Ru/Al$_2$O$_3$ (Commercial) catalysts.

Catalyst	E_a [kJ/mol]
RNN	68
RAA	79
RCl	N/A
Ru/Al$_2$O$_3$ (Commercial)	91

Figure 23 exhibits the plot between rate of CH_4 formation and reaction temperature of RNN, RAA and RCl catalysts comparing with Ru/Al_2O_3 (Commercial) catalyst. The CH_4 formation rate of RNN and RAA catalysts are significantly higher than RCl catalyst. These results mean that a gram of RNN and RAA catalysts can produce CH_4 more than RCl catalyst. In addition, turnover frequencies (TOF) of CO_2 conversion of RNN, RAA and RCl catalysts are shown in Figure 24 which observed at reaction temperature between 250 to 350°C. The TOF of RCl catalyst could not report due to the active site of this catalyst could not measure. In an observation, the TOF of RNN catalyst was lower than that of RAA catalyst and also Ru/Al_2O_3 (Commercial).

The apparent activation energies (E_a) of CO_2 hydrogenation reaction over RNN, RAA, RCl and Ru/Al_2O_3 (Commercial) catalysts are shown in Table 11. These results were calculated from the slopes of linear lines in Figure 24. It is observed that these results are similar to E_a values of Ru/Al_2O_3 catalysts in CO_2 hydrogenation [51].

As the results description above, Ru/Al_2O_3 catalyst prepared by ruthenium (III) nitrosyl nitrate precursor or RNN catalyst can give high catalytic activity and high stability, and also solvent used in the preparation of this catalyst is more safety and environmental friendly than others. Therefore, ruthenium (III) nitrosyl nitrate precursor is used as Ru precursor for all catalysts in further two section.

5.2 Effect of ZrO_2 addition in χ-Al_2O_3 supported Ru catalyst

In this section, Ru catalysts supported on ZrO_2-Al_2O_3 prepared by using ruthenium (III) nitrosyl nitrate precursor are investigated with various ZrO_2 content as 5, 10, 15 and 20 wt.%. These Ru/ZrO_2-Al_2O_3 catalysts are compared with Ru/χ-Al_2O_3 or RNN catalyst and Ru/γ-Al_2O_3 or Ru/Al_2O_3 (Commercial) catalyst.

5.2.1 Catalytic characterization

BET surface area, pore volume and pore diameter of RNN, Ru/Al$_2$O$_3$ (commercial) and Ru/ZrO$_2$-Al$_2$O$_3$ catalysts are shown in **Table 12**. BET surface area of catalysts decreased with ZrO$_2$ presence and these results were almost no different. Pore volume and pore diameter of Ru/5%ZrO$_2$-Al$_2$O$_3$ was larger than RNN catalyst, and then, that decreased with increasing amount of ZrO$_2$ in support. In addition, the BET surface area of Ru/Al$_2$O$_3$ (Commercial) catalyst (158 m^2/g) was less than that of RNN catalyst (171 m^2/g) while pore volume and pore diameter of Ru/Al$_2$O$_3$ (Commercial) catalyst as 0.23 cm^3/g and 5.8 nm were higher than those of RNN catalyst as 0.21 cm^3/g and 5.0 nm, respectively.

Table 12 BET surface area, pore volume, pore diameter, isotherm type and hysteresis loop type of RNN, Ru/Al$_2$O$_3$ (commercial) and Ru/ZrO$_2$-Al$_2$O$_3$ catalysts.

Catalyst	BET surface area [m^2/g]	Pore volume [cm^3/g]	Pore diameter [nm]	Type of isotherm	Type of hysteresis loop
Ru/Al$_2$O$_3$ (commercial)	158	0.23	5.8		
RNN	171	0.21	5.0		
Ru/5%ZrO$_2$-Al$_2$O$_3$	142	0.22	6.1	IV(a)	H2(b)
Ru/10%ZrO$_2$-Al$_2$O$_3$	136	0.19	5.5		
Ru/15%ZrO$_2$-Al$_2$O$_3$	146	0.18	5.0		
Ru/20%ZrO$_2$-Al$_2$O$_3$	149	0.18	4.9		
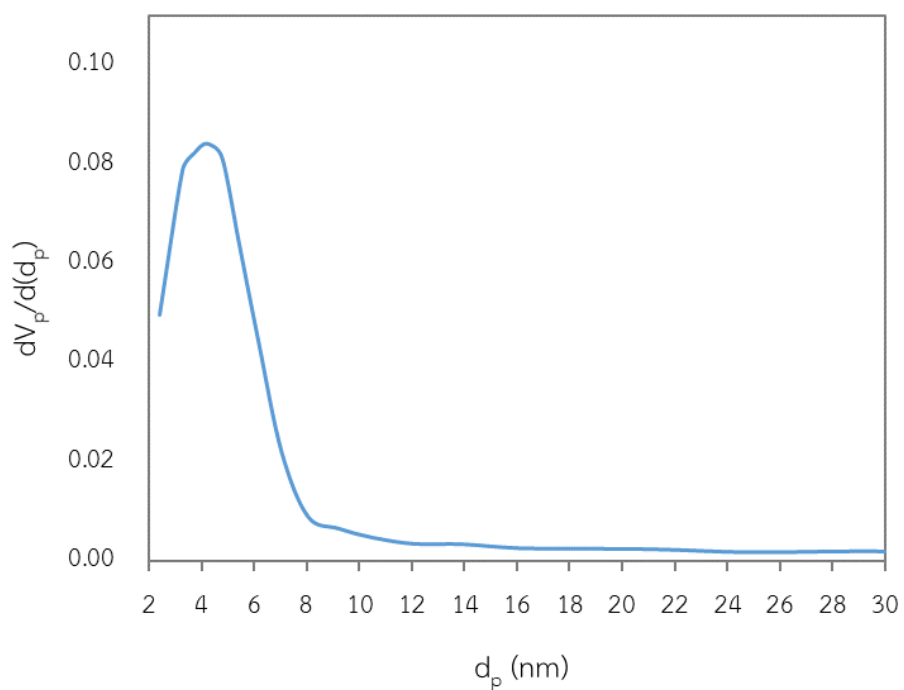
Figure 25 Pore diameter distribution of RNN catalyst.
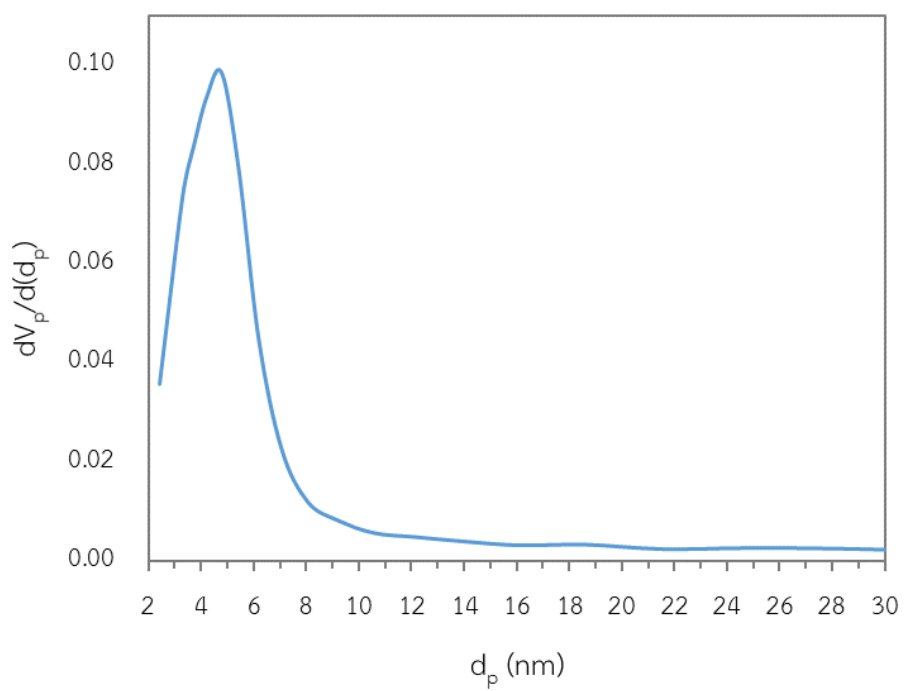
Figure 26 Pore diameter distribution of Ru supported on Al_2O_3 commercial catalyst.
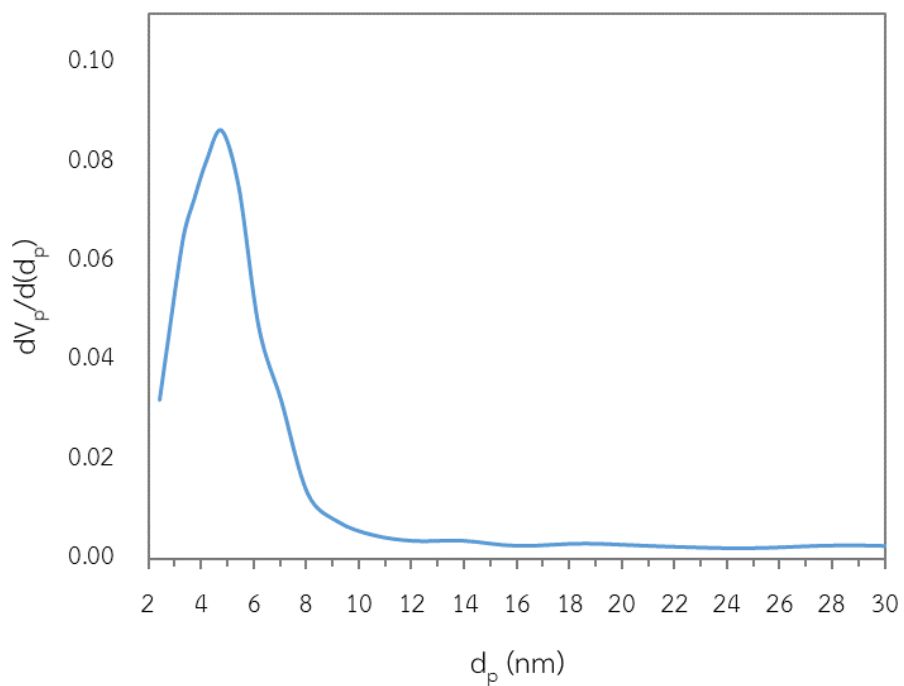
Figure 27 Pore diameter distribution of Ru/5%ZrO$_2$-Al$_2$O$_3$ catalyst.
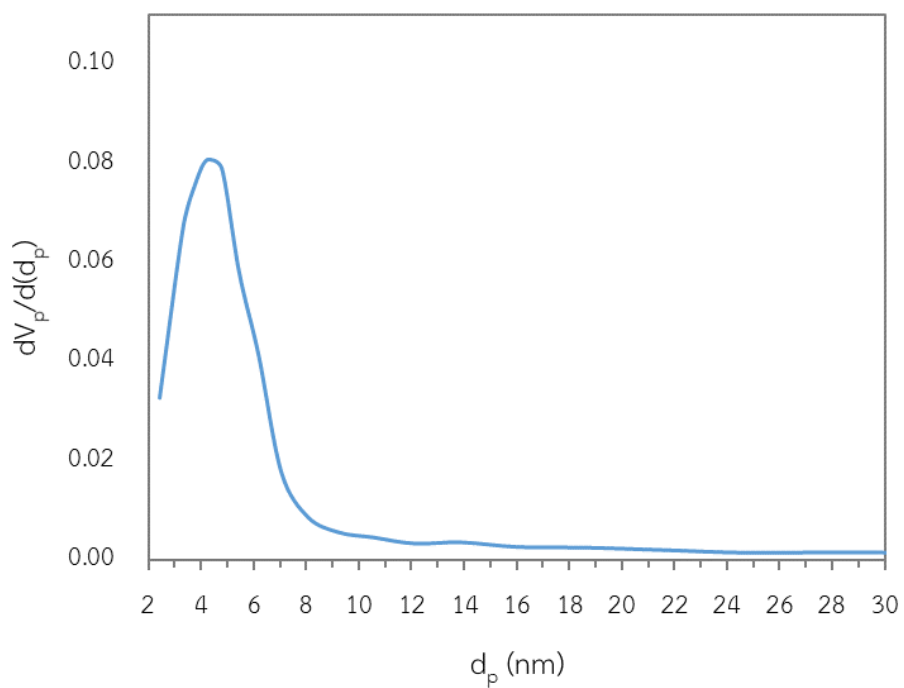
Figure 28 Pore diameter distribution of Ru/10%ZrO$_2$-Al$_2$O$_3$ catalyst.
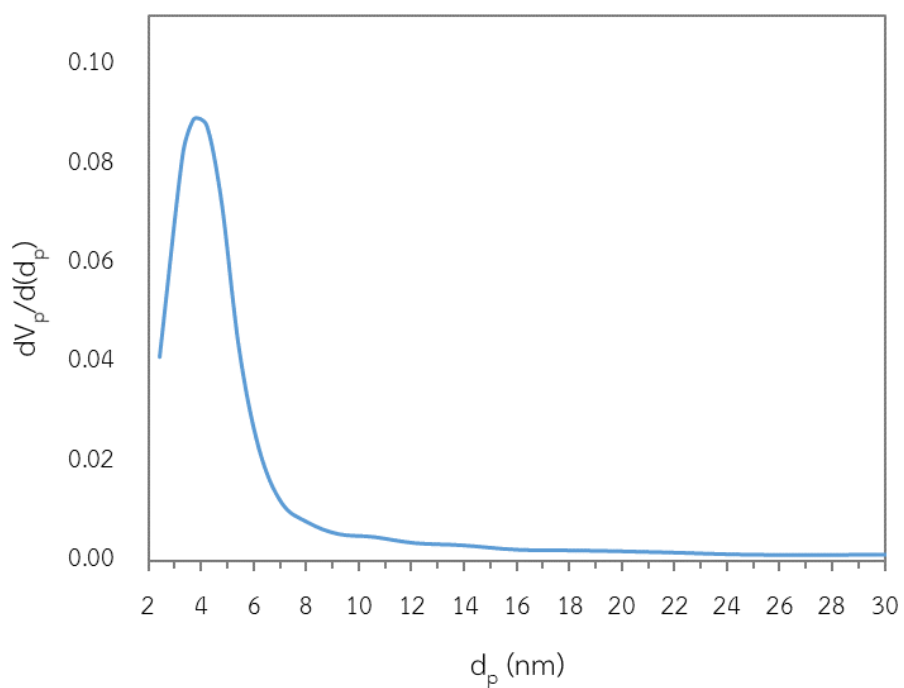
Figure 29 Pore diameter distribution of Ru/15%ZrO$_2$-Al$_2$O$_3$ catalyst.
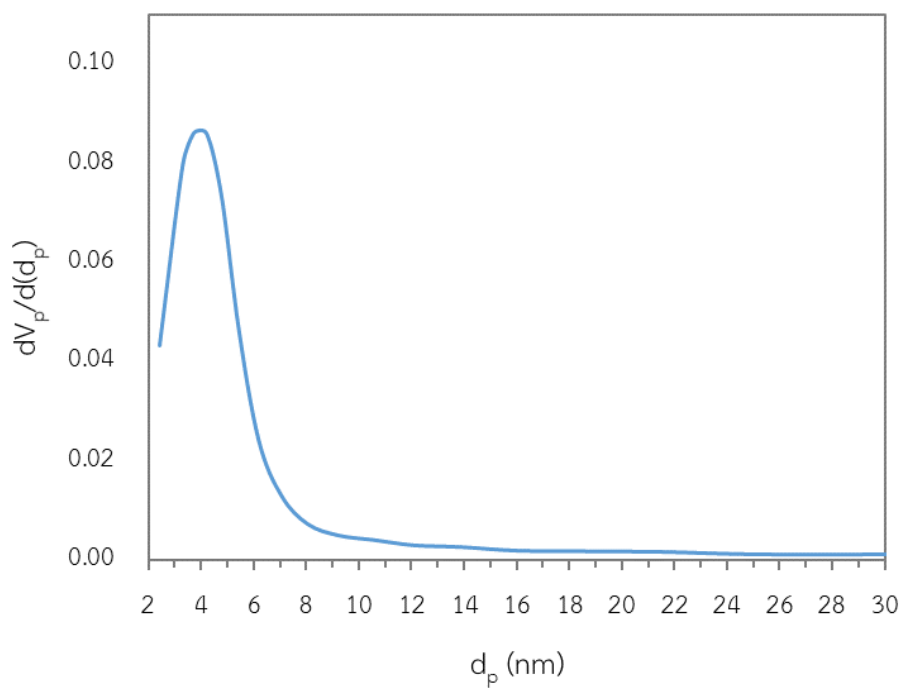
Figure 30 Pore diameter distribution of Ru/20%ZrO$_2$-Al$_2$O$_3$ catalyst.

Pore diameter distributions of RNN, Ru/Al$_2$O$_3$ (Commercial) and Ru/ZrO$_2$-Al$_2$O$_3$ catalysts analyzed by BJH method are shown in **Figure 25 – 30**. The RNN, Ru/Al$_2$O$_3$ (Commercial) and Ru/ZrO$_2$-Al$_2$O$_3$ catalysts exhibited a narrow pore diameter distribution. Pore structure of these catalyst was same structure as mesopore. It is further described in N$_2$ adsorption and desorption isotherm and hysteresis loop.

N$_2$ adsorption and desorption isotherm of RNN, Ru/Al$_2$O$_3$ (Commercial) and Ru/ZrO$_2$-Al$_2$O$_3$ catalysts are exhibited in **Figure 31 – 36**. The physisorption isotherms of all catalysts were assigned to type IV(a). This type is described that the catalysts is mesopores structure. In addition, types of hysteresis loop of these all catalysts were H2(b). The type of H2(b) is specified that porous characteristics of catalysts are cylindrical porous structure [58].
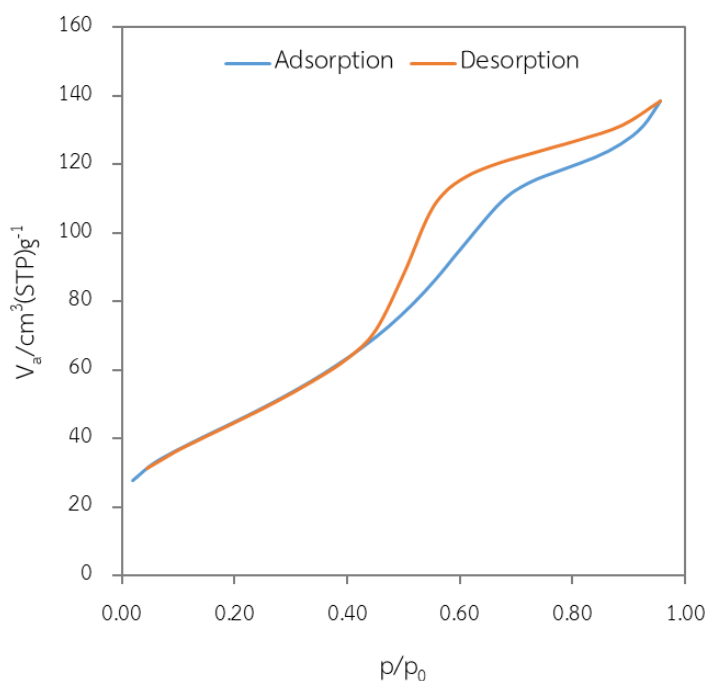
Figure 31 N$_2$ adsorption and desorption isotherm of RNN catalyst.
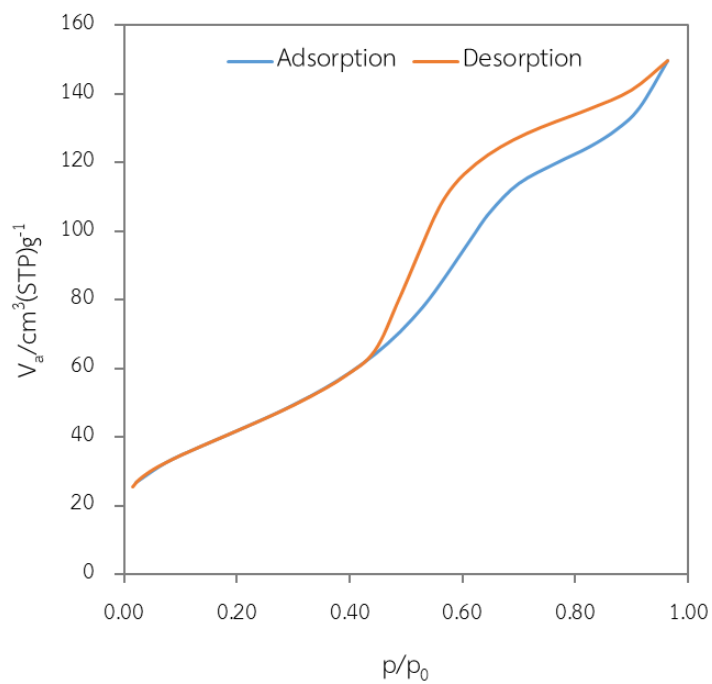
Figure 32 N_2 adsorption and desorption isotherm of Ru supported on Al_2O_3 commercial catalyst.
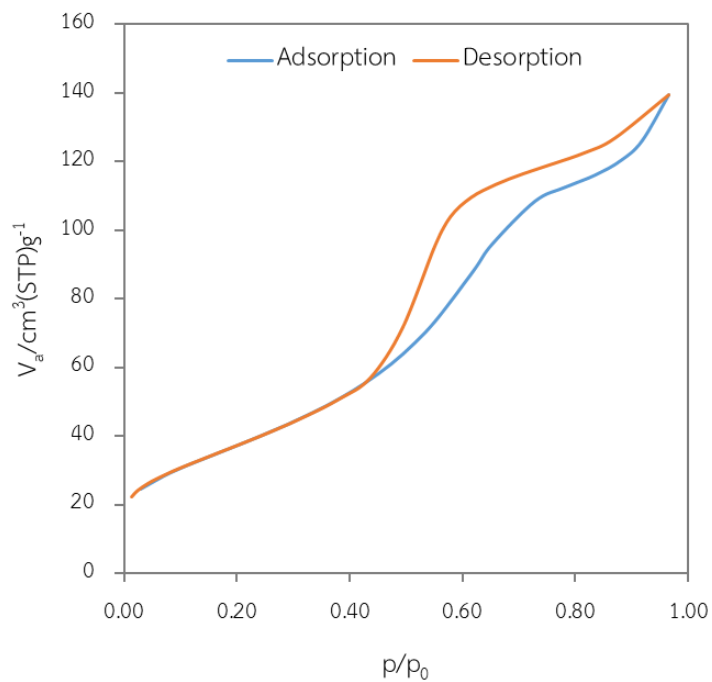
Figure 33 N_2 adsorption and desorption isotherm of Ru/5%ZrO_2-Al_2O_3 catalyst.
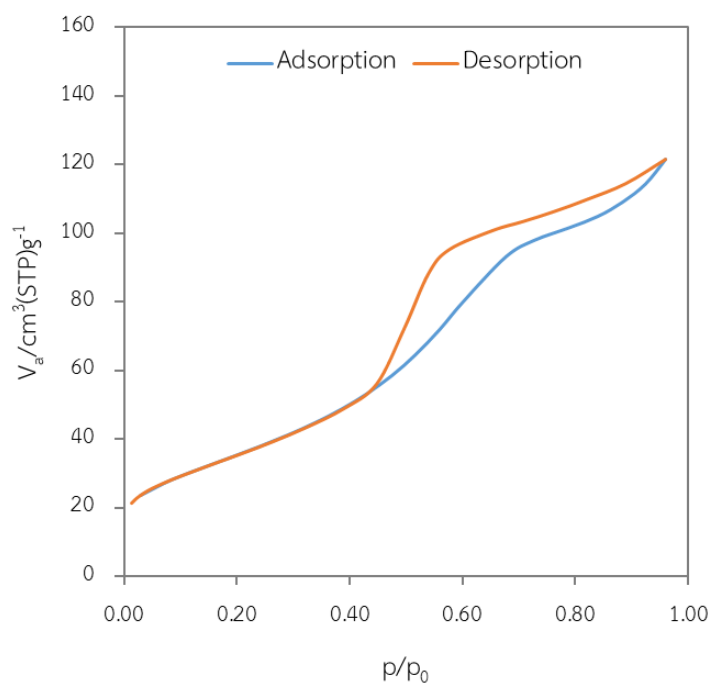
Figure 34 N_2 adsorption and desorption isotherm of Ru/10%ZrO$_2$-Al$_2$O$_3$ catalyst.
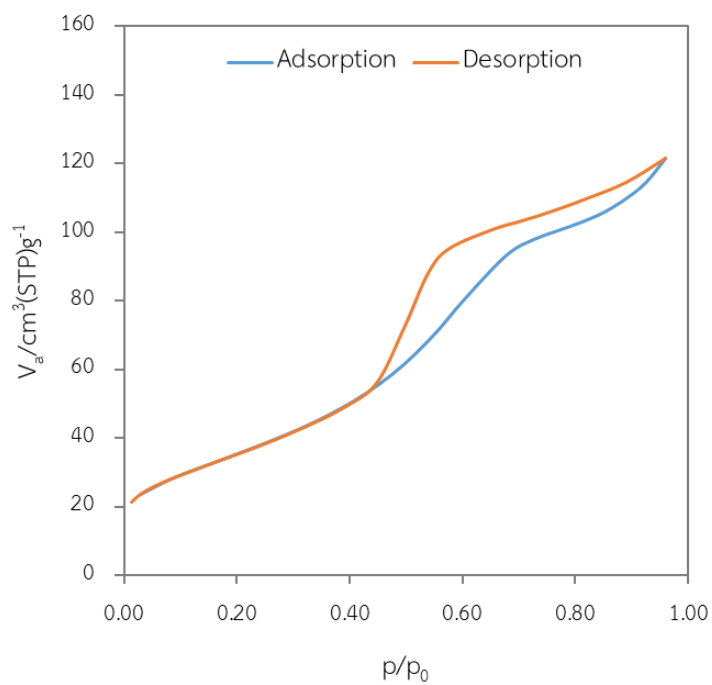
Figure 35 N_2 adsorption and desorption isotherm of Ru/15%ZrO$_2$-Al$_2$O$_3$ catalyst.
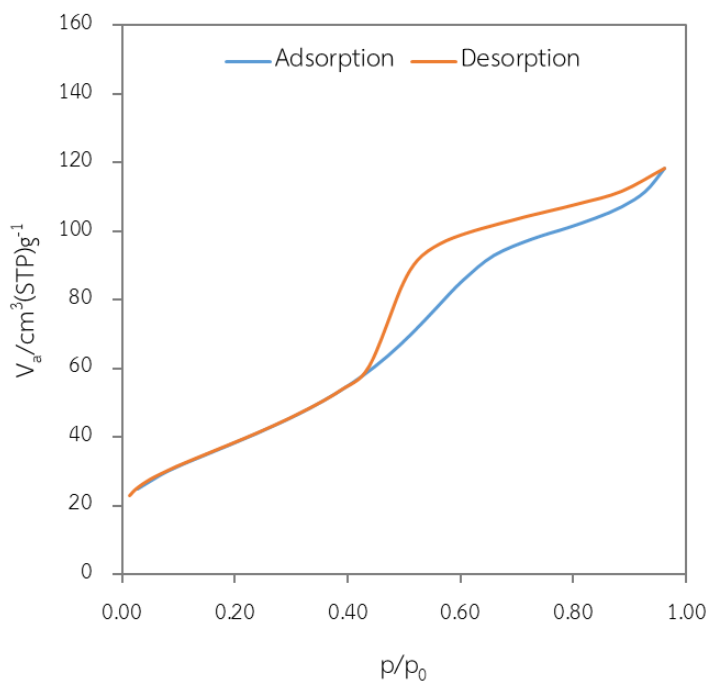
Figure 36 N_2 adsorption and desorption isotherm of Ru/20%ZrO$_2$-Al$_2$O$_3$ catalyst.

Figure 37 indicates XRD patterns of RNN, Ru/Al$_2$O$_3$ (Commercial) and Ru/ZrO$_2$-Al$_2$O$_3$ catalysts. This figure appeared peak of RuO$_2$ in all catalysts which the positions of this peak consisted to 2θ = 28°, 35° and 54.5° [4]. The catalysts of ZrO$_2$ presence could be clearly seen that ZrO$_2$ formed in tetragonal structure and its main diffraction peak was specified as 2θ = 30° [64]. In observing, the intensity of ZrO$_2$ peak increased with increasing amount of ZrO$_2$ loading.
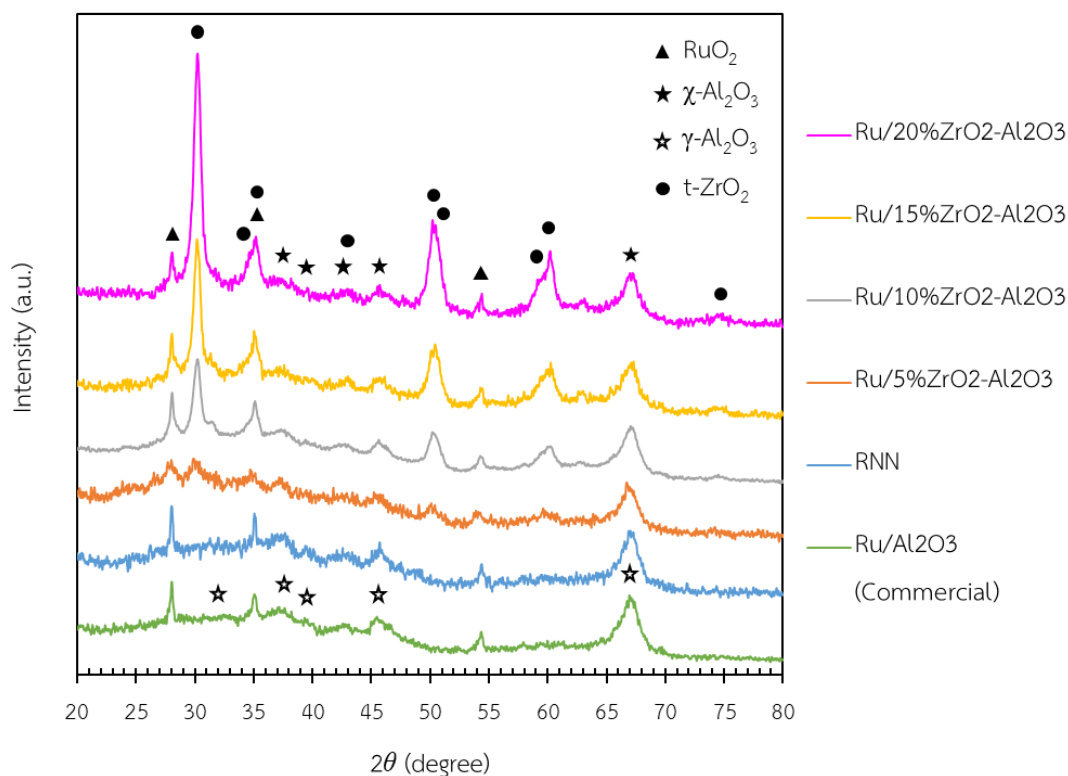
Figure 37 XRD pattern of RNN, Ru/Al$_2$O$_3$ (commercial) and Ru/ZrO$_2$-Al$_2$O$_3$ catalysts.

Table 13 Crystallite size of RNN, Ru/Al$_2$O$_3$ (commercial) and Ru/ZrO$_2$-Al$_2$O$_3$ catalysts calculated by XRD results.

Catalyst	Crystallite size (nm)		
	RuO$_2$	Al$_2$O$_3$	ZrO$_2$
Ru/Al$_2$O$_3$ (Commercial)	31	5.6	-
RNN	31	6.3	-
Ru/5%ZrO$_2$-Al$_2$O$_3$	14	6.3	5.2
Ru/10%ZrO$_2$-Al$_2$O$_3$	27	6.0	11.8
Ru/15%ZrO$_2$-Al$_2$O$_3$	31	6.3	12.9
Ru/20%ZrO$_2$-Al$_2$O$_3$	37	6.1	12.2

Crystallite size of each species in RNN, Ru/Al_2O_3 (Commercial) and Ru/ZrO_2-Al_2O_3 catalysts calculated by using the Scherrer's equation is indicated in **Table 13**. It was observed that crystallite sizes of RuO_2 in RNN and Ru/Al_2O_3 (Commercial) catalysts were the same size (31 nm) which it meant that the Al_2O_3 phase did not affect to crystallite size of metal oxide. Interesting, the crystallite size of RuO_2 decreased to 14 nm when ZrO_2 added small amount in support ($Ru/5\%ZrO_2$-Al_2O_3). Whereas, the crystallite size of RuO_2 increased to 27 nm for $Ru/10\%ZrO_2$-Al_2O_3 catalyst, and also increased to 37 nm when added ZrO_2 further to $20\%ZrO_2$. The crystallite size of Al_2O_3 seemed similarly in all catalysts as about 6 nm, while the ZrO_2 crystallite size of various Ru/ZrO_2-Al_2O_3 catalysts increased with increasing amount of ZrO_2 added.
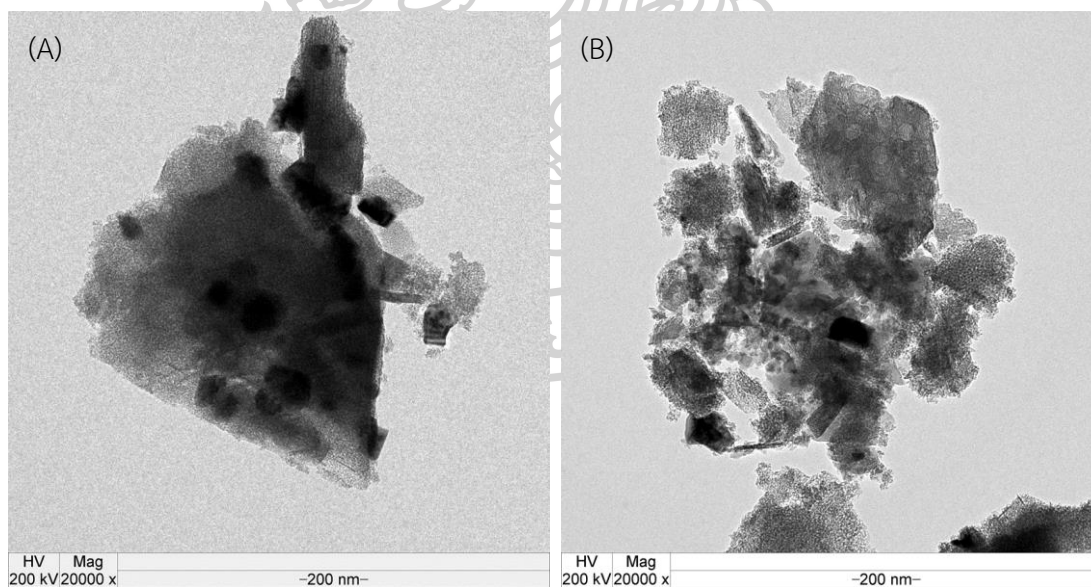
Figure 38 TEM images of RNN catalyst (A) and Ru/Al_2O_3 (Commercial) catalyst (B).
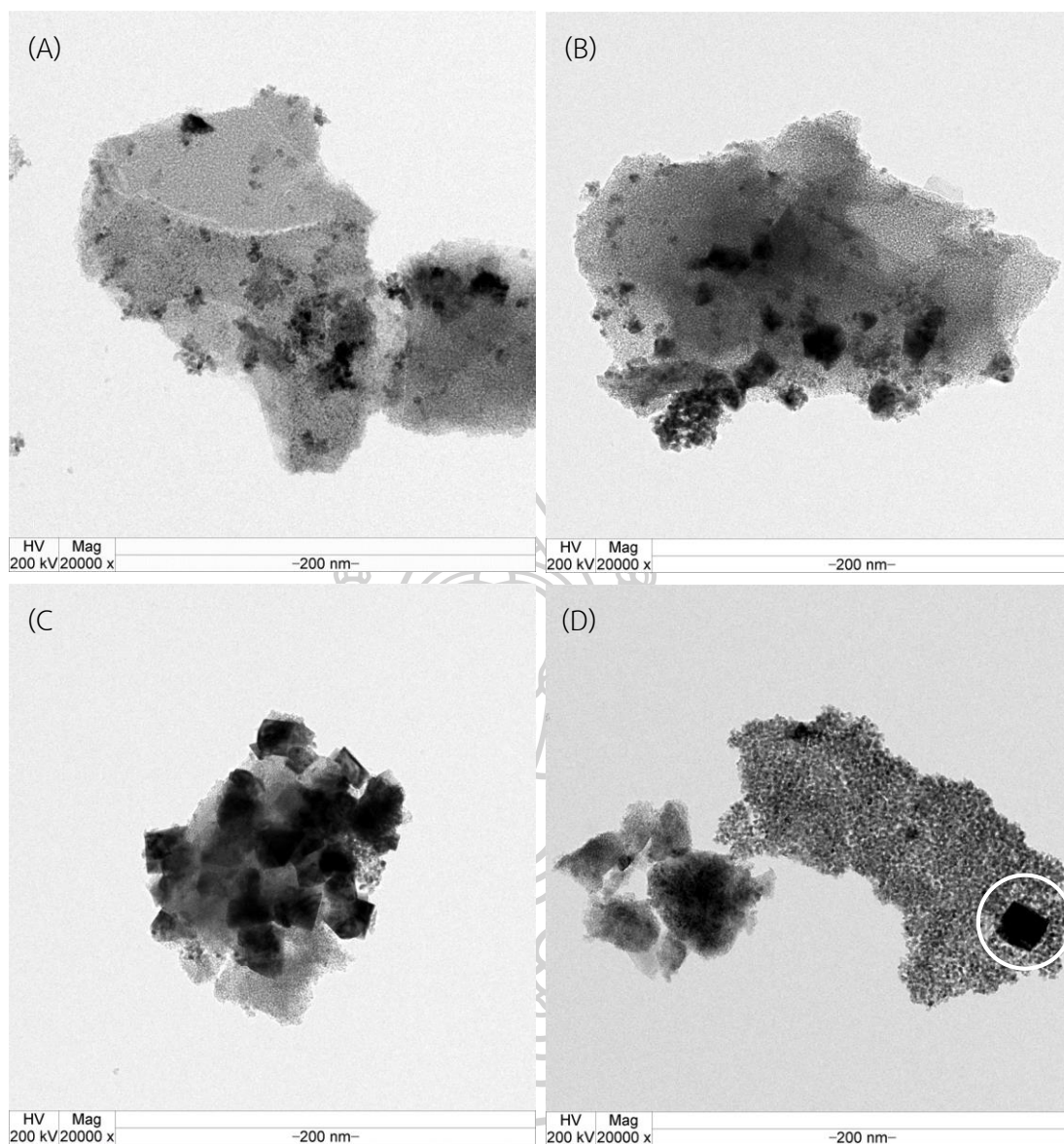
Figure 39 TEM images of Ru/ZrO$_2$-Al$_2$O$_3$ catalysts seeing that (A) Ru/5%ZrO$_2$-Al$_2$O$_3$ catalyst, (B) Ru/10%ZrO$_2$-Al$_2$O$_3$ catalyst, (C) Ru/15%ZrO$_2$-Al$_2$O$_3$ catalyst and (D) Ru/20%ZrO$_2$-Al$_2$O$_3$ catalyst.
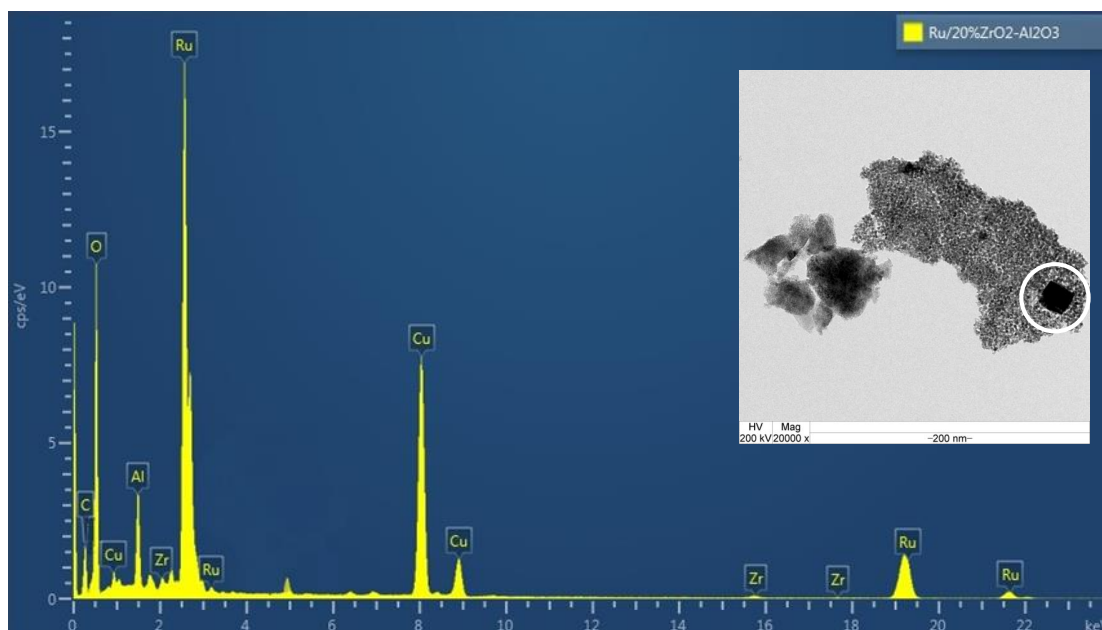
Figure 40 EDS spectra obtained at the area in cycle that presented in TEM image of Ru/20%ZrO$_2$-Al$_2$O$_3$ catalyst.

TEM images of RNN, Ru/Al$_2$O$_3$ (Commercial) and Ru/ZrO$_2$-Al$_2$O$_3$ catalysts are exhibited in **Figure 38 and 39**. The deep black parts were assigned as RuO$_2$. It appeared fine particles and smaller particles size of RuO$_2$ on γ-Al$_2$O$_3$ support than the particles size of RuO$_2$ in RNN catalyst. Whereas, some particles of RuO$_2$ in Ru/Al$_2$O$_3$ (Commercial) catalyst were large size and similar to RNN catalyst. These large RuO$_2$ particles of RNN and Ru/Al$_2$O$_3$ (Commercial) catalysts seemed as result of particle aggregation to cluster form. In an observation in Ru/ZrO$_2$-Al$_2$O$_3$ catalysts, the RuO$_2$ particles of Ru/5%ZrO$_2$ catalyst were smaller than other Ru/ZrO$_2$-Al$_2$O$_3$ catalysts, and highly dispersed on support. Moreover, the particles size of RuO$_2$ increased with increasing ZrO$_2$ composition in χ-Al$_2$O$_3$ support which these results were the same trend to their XRD results. An EDS spectrum of area in the cycle of Ru/20%ZrO$_2$-Al$_2$O$_3$ catalyst is presented in **Figure 40**. It could confirm the above description that the deep dark parts were assigned to RuO$_2$.

Active site, Ru metal dispersion and average Ru particle size of RNN, Ru/Al$_2$O$_3$ (commercial) and Ru/ZrO$_2$-Al$_2$O$_3$ catalysts are represented in **Table 14**. The active site of RNN catalyst was same that of Ru/Al$_2$O$_3$ (Commercial) catalyst which it was 3.0 µmol/g$_{cat}$. Both Ru dispersion and average Ru particle size of RNN catalyst were almost same value as those of Ru/Al$_2$O$_3$ (Commercial) catalyst. In ZrO$_2$ adding in support observed that the catalysts with ZrO$_2$ presence gave more active site and Ru dispersion which Ru/10%ZrO$_2$-Al$_2$O$_3$ catalyst could indicate the highest active site and Ru dispersion as 9.7 µmol/g$_{cat}$ and 9.8%, respectively. But at large amount of ZrO$_2$ loading, the active site and Ru dispersion of Ru/15%ZrO$_2$-Al$_2$O$_3$ catalyst decreased and the Ru/20%ZrO$_2$-Al$_2$O$_3$ catalyst was the least active site and Ru dispersion. In the explanation above, ZrO$_2$ addition in χ-Al$_2$O$_3$ support of Ru catalyst could improve active site and metal dispersion. Whereas, the presence of high amount of ZrO$_2$ or more than 10%ZrO$_2$ affected to decreased active site and metal dispersion which it was probably due to RuO$_2$ aggregation.

Table 14 H$_2$ chemisorption results of RNN, Ru/Al$_2$O$_3$ (commercial) and Ru/ZrO$_2$-Al$_2$O$_3$ catalysts.

Catalyst	Active site [µmol/g$_{cat.}$]	Ru dispersion [%]	Average diameter of Ru particles [nm]
Ru/Al$_2$O$_3$ (commercial)	3.0	3.1	29
RNN	3.0	3.0	30
Ru/5%ZrO$_2$-Al$_2$O$_3$	5.1	5.2	17
Ru/10%ZrO$_2$-Al$_2$O$_3$	9.7	9.8	9
Ru/15%ZrO$_2$-Al$_2$O$_3$	5.7	5.8	16
Ru/20%ZrO$_2$-Al$_2$O$_3$	2.1	2.1	43

Figure 41 indicates H_2-TPR profiles of RNN, Ru/Al$_2$O$_3$ (commercial) and Ru/ZrO$_2$-Al$_2$O$_3$ catalysts. The results were composed to two sharp low reduction temperature peaks and a broad high reduction temperature peaks. As according to several literatures [59, 61-63], the two peaks of low reduction temperature could be assigned to the reduction of RuO$_2$ to RuO and RuO to Ru^0, respectively. A high reduction temperature peaks could be attributed to Ru oxidized reduction that strongly interaction with support. In an observation, the second and third reduction peaks of Ru catalysts with ZrO$_2$ presence were shifted to higher reduction temperature with increasing amount ZrO$_2$ loading. Moreover, these two reduction peaks of Ru/20%ZrO$_2$-Al$_2$O$_3$ catalyst were more shifted to higher reduction temperature than other Ru catalysts with ZrO$_2$ loading. In Ru/20%ZrO$_2$-Al$_2$O$_3$ catalyst, it appeared the fourth reduction peak at very high reduction temperature of about 625°C. This small broad peak was assigned to reduction of ZrO$_2$ crystallites which similar result was reported by Souza, M.M.V.M. et al. [65]. They reported that 20%ZrO$_2$/Al$_2$O$_3$ was also appeared a small peak at reduction temperature of 650°C, whereas lower amount of ZrO$_2$ did not have reduction peak appeared.
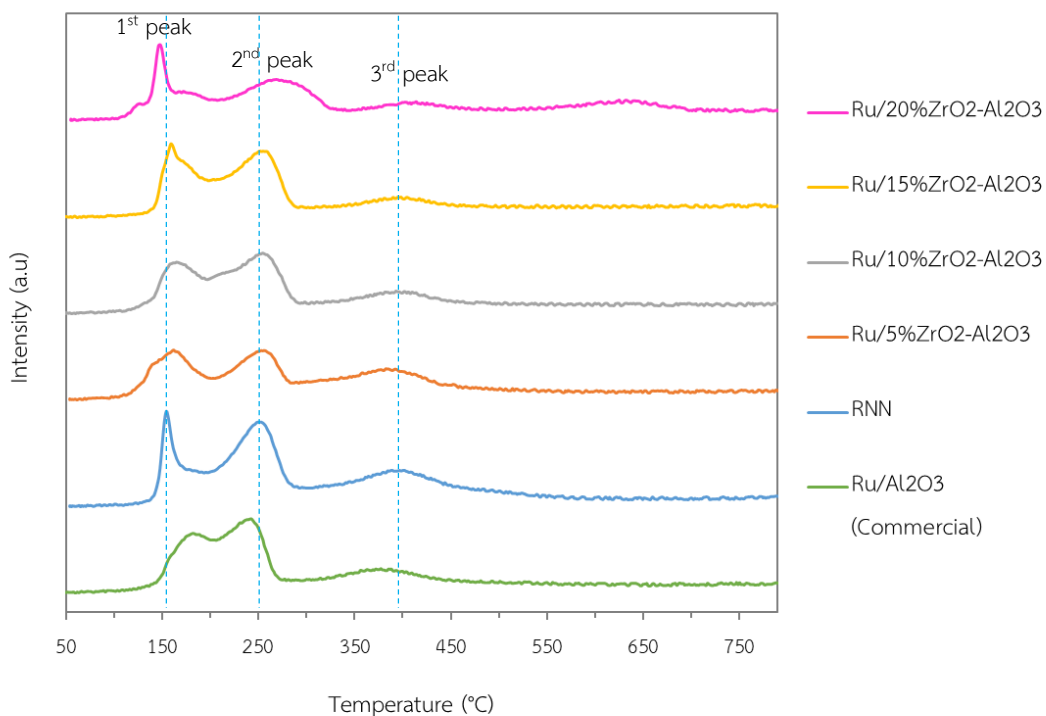
Figure 41 H_2-TPR profiles of RNN, Ru/Al_2O_3 (commercial) and $Ru/ZrO_2-Al_2O_3$ catalysts.

5.2.2 Catalytic activity test

Ru catalysts supported on various amount of ZrO_2 in χ-Al_2O_3 prepared by using ruthenium (III) nitrosyl nitrate precursor are investigated in CO_2 hydrogenation reaction. The amount of ZrO_2 added in support is varied as 5, 10, 15 and 20 wt.% of ZrO_2. A reaction gases mixture of 12.5% CO_2, 50% H_2 ($4H_2/1CO_2$) with He balanced, and GHSV = 14,416 h^{-1} are used in this investigation. The various $Ru/ZrO_2-Al_2O_3$ catalysts are compared with Ru/χ-Al_2O_3 or RNN and Ru/γ-Al_2O_3 or Ru/Al_2O_3 (Commercial) catalysts.

Conversion of CO_2 as function of temperature obtained over RNN, Ru/Al_2O_3 (Commercial) and $Ru/ZrO_2-Al_2O_3$ catalysts is plotted in **Figure 42**. The CO_2 conversion curves increased with increasing reaction temperature and they were almost the same conversion at high temperature which these curves could be approached to

thermodynamic equilibrium. These results are accorded to reports of Cai M. et al. [27]. They were presented the result of Ru/Al_2O_3. In increasing reaction temperature, CO_2 conversion was reached to thermodynamic equilibrium. In addition, ZrO_2 loading in support of Ru catalysts resulted to the CO_2 conversion increased and $Ru/20\%ZrO_2$ catalyst indicated high CO_2 conversion at lower temperature than other catalysts. In Ru/Al_2O_3 (commercial) catalyst, CO_2 conversion increased with increasing reaction temperature, and also decreased suddenly at reaction temperature of 400°C that was probably because of catalytic deactivation at high temperature or sintering.
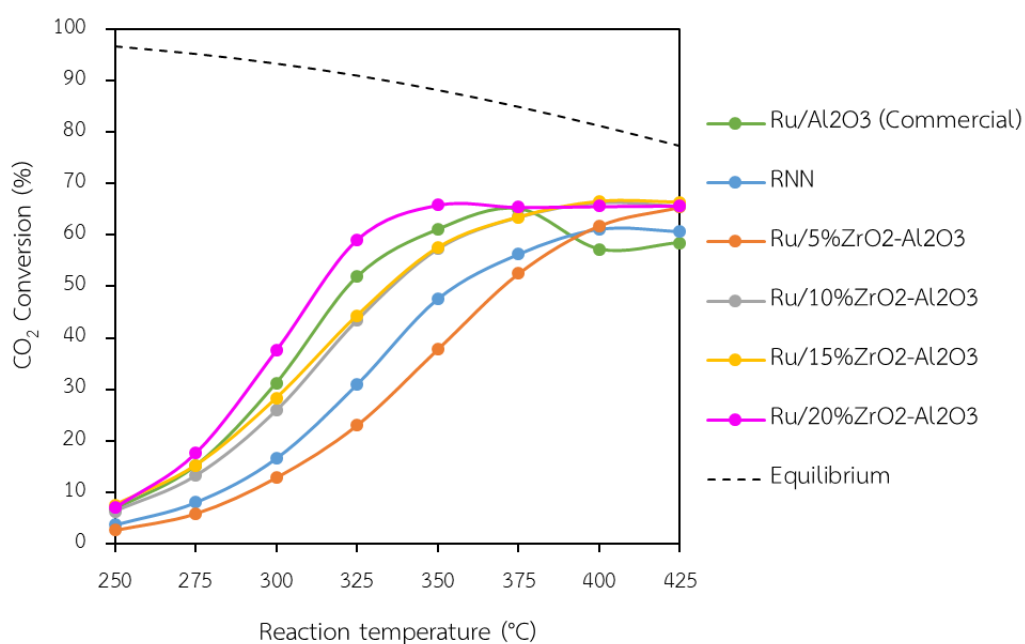
Figure 42 CO_2 conversion as function of reaction temperature of RNN, Ru/Al_2O_3 (Commercial) and Ru/ZrO_2-Al_2O_3 catalysts.
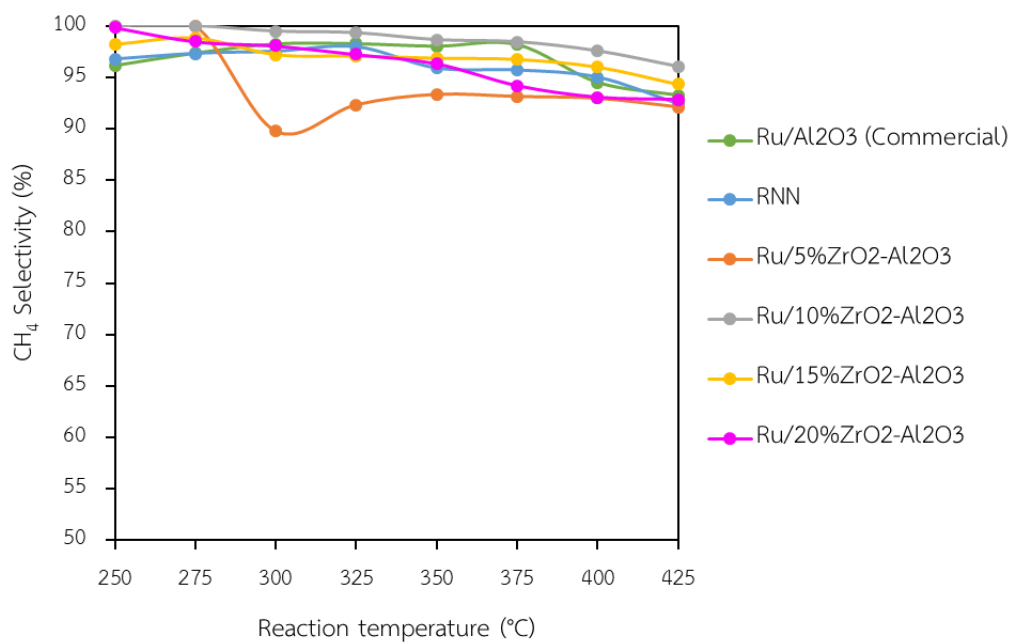
Figure 43 CH$_4$ selectivity as function of reaction temperature of RNN, Ru/Al$_2$O$_3$ (commercial) and Ru/ZrO$_2$-Al$_2$O$_3$ catalysts.
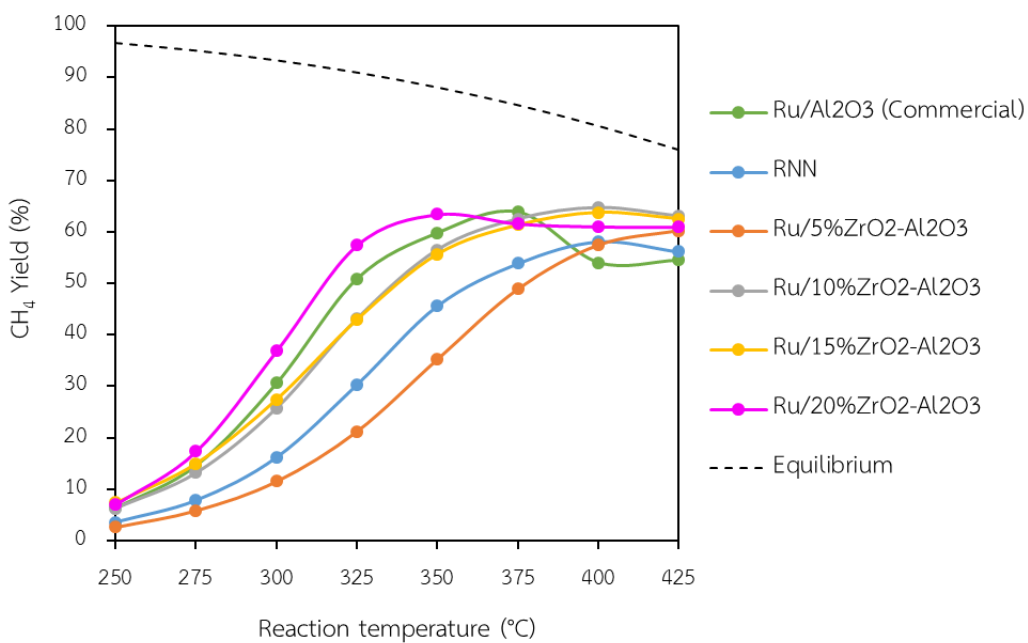
Figure 44 CH$_4$ yield as function of reaction temperature of RNN, Ru/Al$_2$O$_3$ (Commercial) and Ru/ZrO$_2$-Al$_2$O$_3$ catalysts.
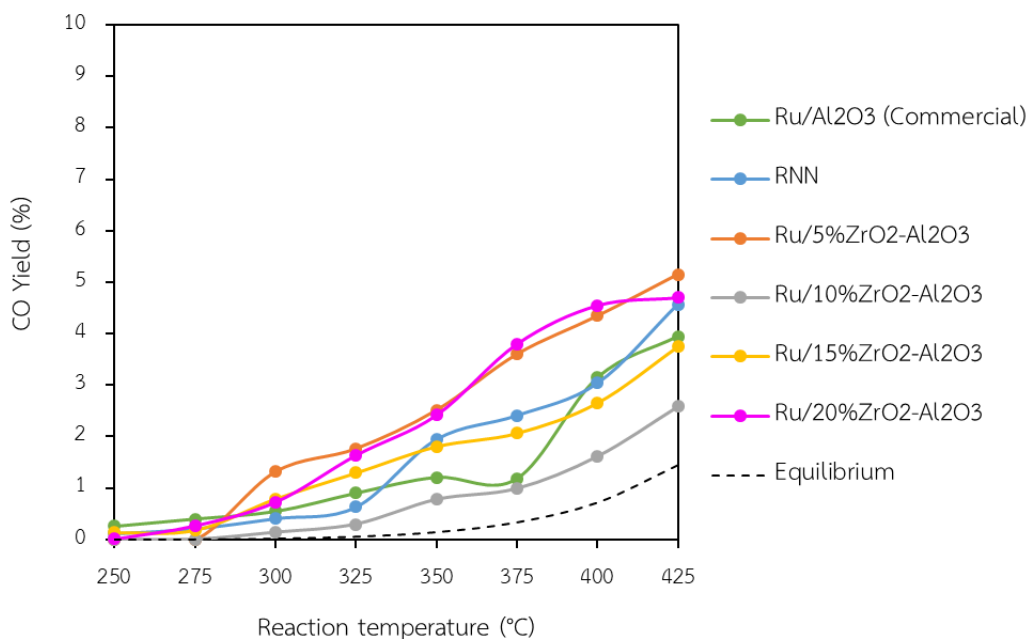
Figure 45 CO yield as function of reaction temperature of RNN, Ru/Al$_2$O$_3$ (Commercial) and Ru/ZrO$_2$-Al$_2$O$_3$ catalysts.

Figure 43 is indicated plots of CH$_4$ selectivity of RNN, Ru/Al$_2$O$_3$ (commercial) and Ru/ZrO$_2$-Al$_2$O$_3$ catalysts with reaction temperature. All catalysts indicated excellent selectivity of CH$_4$ and almost 100% at all reaction temperatures. CH$_4$ yield as function of reaction temperature of RNN, Ru/Al$_2$O$_3$ (Commercial) and Ru/ZrO$_2$-Al$_2$O$_3$ catalysts is shown in **Figure 44**. The CH$_4$ yield profiles indicated that the CH$_4$ yield increased with increasing reaction temperature, and the maximum CH$_4$ yield could shift to lower reaction temperature with increasing amount of ZrO$_2$ loading. In CO yields represented in **Figure 45**, the CO yields increased with increasing reaction temperature and those of all catalysts were lower than 5% of CO yield.
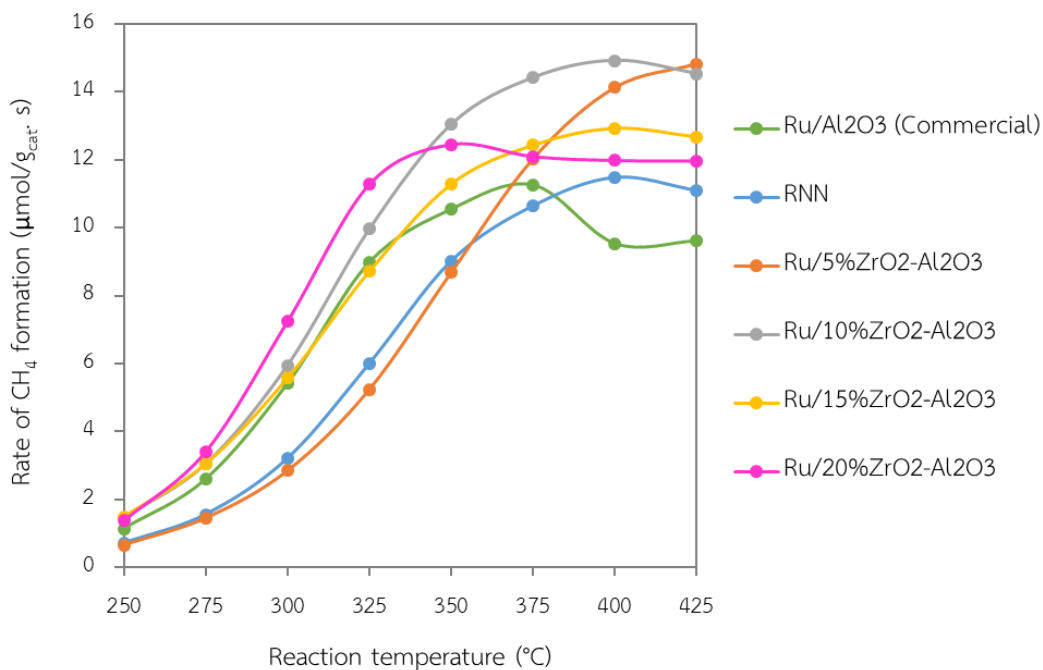
Figure 46 Rate of CH_4 formation as function of reaction temperature of RNN, Ru/Al_2O_3 (Commercial) and $Ru/ZrO_2-Al_2O_3$ catalysts.
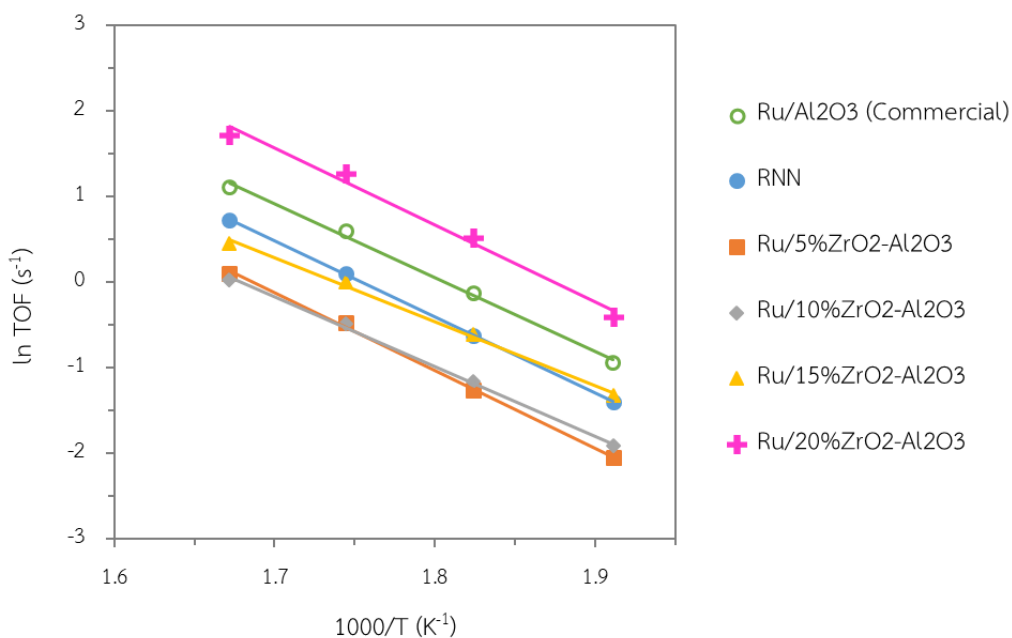
Figure 47 Turnover frequency (TOF) of CO_2 conversion obtained from RNN, Ru/Al_2O_3 (Commercial) and $Ru/ZrO_2-Al_2O_3$ catalysts.

Table 15 Apparent activation energy (E_a) of CO_2 hydrogenation reaction obtained from RNN, Ru/Al_2O_3 (Commercial) and $Ru/ZrO_2-Al_2O_3$ catalysts.

Catalyst	E_a [kJ/mol]
Ru/Al_2O_3 (Commercial)	78
RNN	75
$Ru/5\%ZrO_2-Al_2O_3$	79
$Ru/10\%ZrO_2-Al_2O_3$	71
$Ru/15\%ZrO_2-Al_2O_3$	67
$Ru/20\%ZrO_2-Al_2O_3$	88

Figure 46 indicates plots of CH_4 formation rate with reaction temperature obtained from RNN, Ru/Al_2O_3 (Commercial) and $Ru/ZrO_2-Al_2O_3$ catalysts. The rate of CH_4 formation increased with increasing reaction temperature, and at the same time, with increasing amount of ZrO_2 added in support. The addition of ZrO_2 in catalyst, it encouraged the formation of CH_4 that was CO methanation promotion, resulting in CH_4 formation rate higher than the catalysts without ZrO_2. Moreover, the $Ru/10\%ZrO_2-Al_2O_3$ catalyst gave the maximum rate of CH_4 formation that was about 14.9 $\mu mol/g_{cat.}$·s at 400°C due to its maximum amount of active site.

Turnover frequencies (TOF) of CO_2 conversion obtained over RNN, Ru/Al_2O_3 (Commercial) and $Ru/ZrO_2-Al_2O_3$ catalysts are summarized in **Figure 47**. It was observed that the activity per metal atom exposed decreased in order of $Ru/20\%ZrO_2-Al_2O_3$ > Ru/Al_2O_3 (Commercial) > RNN ∼ $Ru/15\%ZrO_2-Al_2O_3$ > $Ru/10\%ZrO_2-Al_2O_3$ ∼ $Ru/5\%ZrO_2-Al_2O_3$. In an interesting, the TOF line of $Ru/20\%ZrO_2-Al_2O_3$ catalyst was higher than other all catalysts because it had stronger interaction between Ru and binary oxides support.

Apparent activation energies (E_a) of CO_2 hydrogenation reaction over RNN, Ru/Al_2O_3 (Commercial) and Ru/ZrO_2-Al_2O_3 catalysts are indicated in **Table 15**. The E_a values of all catalysts were in range of E_a values of Ru/Al_2O_3 catalyst in CO_2 hydrogenation reaction [51].

5.3 Effect of TiO_2 addition in χ-Al_2O_3 supported Ru catalyst

In this section, the effect of TiO_2 added in χ-Al_2O_3 support of Ru catalysts is studied with Ru/χ-Al_2O_3 or RNN catalyst and Ru/γ-Al_2O_3 or Ru/Al_2O_3 (Commercial) catalyst comparison. All catalysts in this section are prepared by incipient wetness impregnation using ruthenium (III) nitrosyl nitrate precursor. The amount of TiO_2 added in support is varied as 2.5, 5, 10 and 15 wt.% TiO_2.

5.3.1 Catalytic characterization

BET surface area, total pore volume and average pore size diameter of RNN, Ru/Al_2O_3 (commercial) and Ru/TiO_2-Al_2O_3 catalysts are exhibited in **Table 16**. In the increasing TiO_2 loading, the BET surface area decreased from Ru/2.5%TiO_2-Al_2O_3 (178 m^2/g) to Ru/15%TiO_2-Al_2O_3 (144 m^2/g), moreover, total pore volume and average pore size diameter increased to 0.25 cm^3/g and 7.0 nm of Ru/15%TiO_2-Al_2O_3. In addition, Ru catalyst supported on χ-Al_2O_3 or RNN catalyst had high BET surface area, low pore volume and small pore diameter than Ru/Al_2O_3 (Commercial) catalyst.

Pore diameter distributions of RNN, Ru/Al_2O_3 (commercial) and Ru/TiO_2-Al_2O_3 catalysts are indicated in **Figure 48 and 53**. The pore diameter distributions of all catalysts appeared a narrow distribution. Mesoporous structure was assigned in pore structure of all catalysts which it was further explained in N_2 adsorption and desorption isotherm and hysteresis loop.

N_2 adsorption and desorption isotherm observed in catalysts of RNN, Ru/Al_2O_3 (Commercial) and Ru/TiO_2-Al_2O_3 are exhibited in **Figure 54 and 59**. The physisorption

isotherms type of all catalysts were specified to type IV(a). This isotherms type is assigned to mesopores structure of catalysts. In observation of hysteresis loop type, these all catalysts were H2(b) type. The hysteresis loop type of H2(b) is assigned that porous of catalysts are characterized as cylindrical porous structure [58].

Table 16 BET surface area, pore volume, pore diameter, isotherm type and hysteresis loop type of RNN, Ru/Al_2O_3 (commercial) and $Ru/TiO_2-Al_2O_3$ catalysts.

Catalyst	BET surface area $[m^2/g]$	Pore volume $[cm^3/g]$	Pore diameter $[nm]$	Type of isotherm	Type of hysteresis loop
Ru/Al_2O_3 (commercial)	158	0.23	5.8		
RNN	171	0.21	5.0		
$Ru/2.5\%TiO_2-Al_2O_3$	178	0.21	4.7	IV(a)	H2(b)
$Ru/5\%TiO_2-Al_2O_3$	163	0.20	5.0		
$Ru/10\%TiO_2-Al_2O_3$	158	0.27	6.7		
$Ru/15\%TiO_2-Al_2O_3$	144	0.25	7.0		
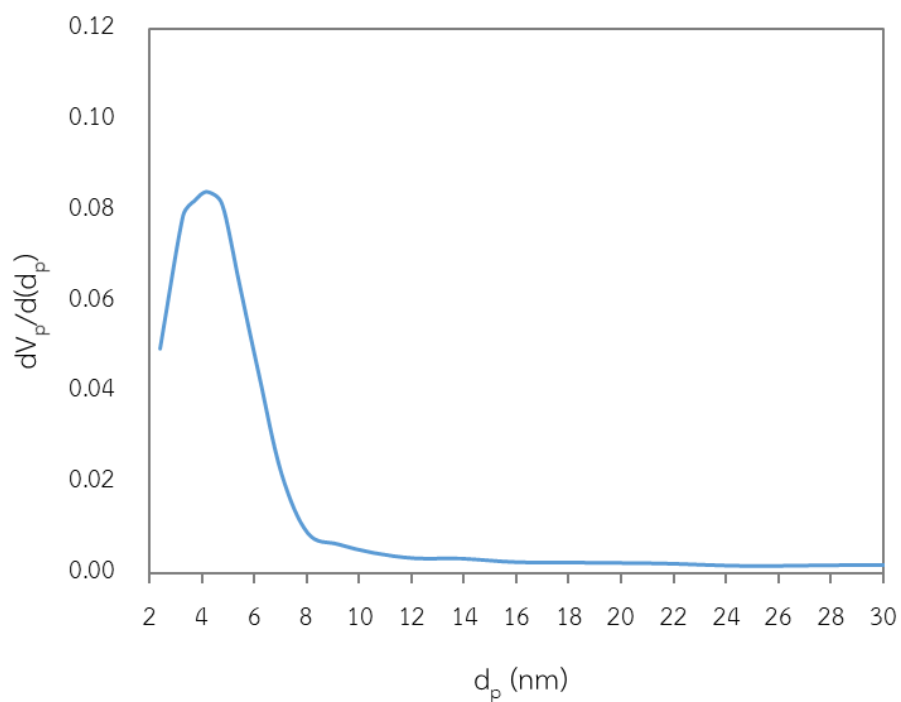
Figure 48 Pore diameter distribution of RNN catalyst.
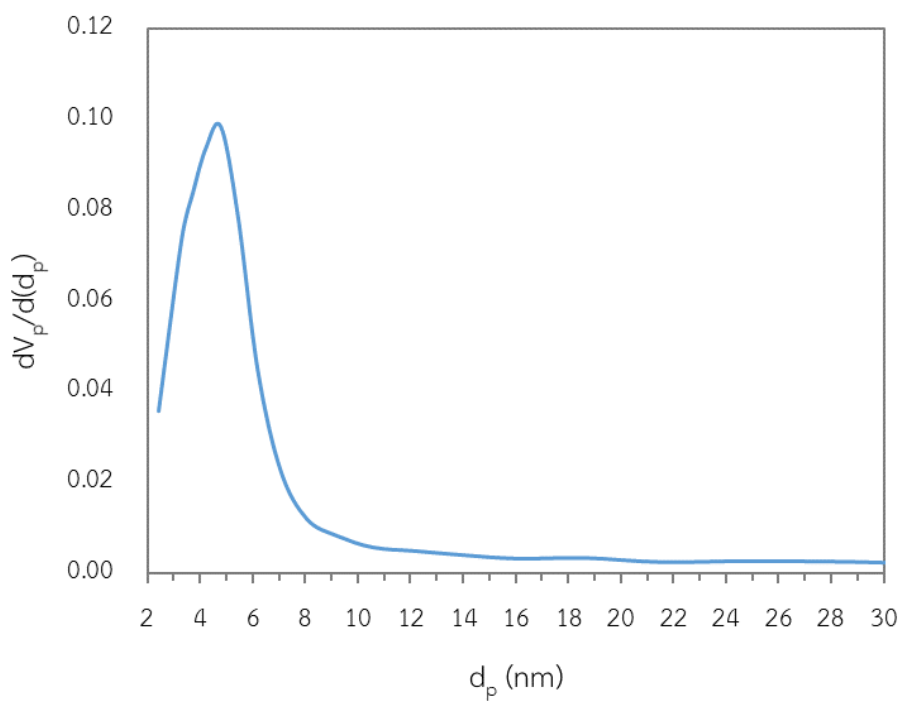
Figure 49 Pore diameter distribution of Ru/Al_2O_3 (commercial) catalyst.
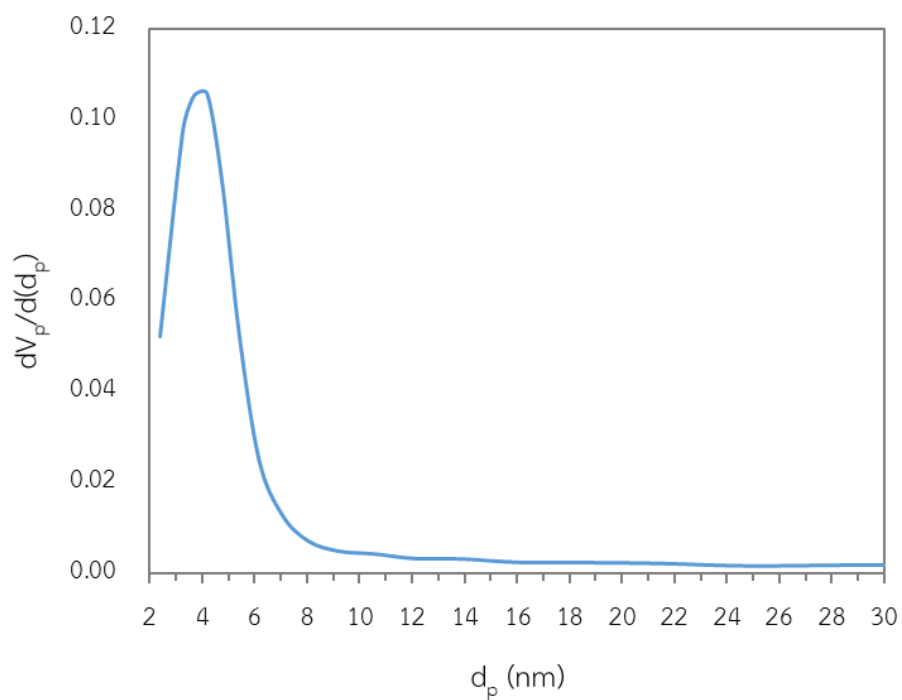
Figure 50 Pore diameter distribution of Ru/2.5%TiO$_2$-Al$_2$O$_3$ catalyst.
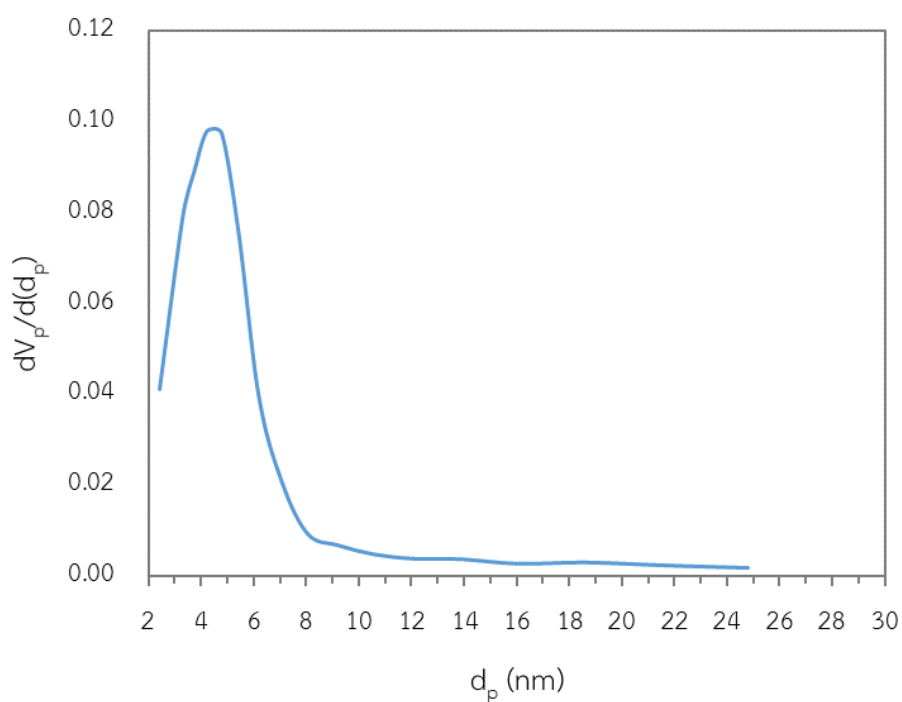
Figure 51 Pore diameter distribution of Ru/5%TiO$_2$-Al$_2$O$_3$ catalyst.
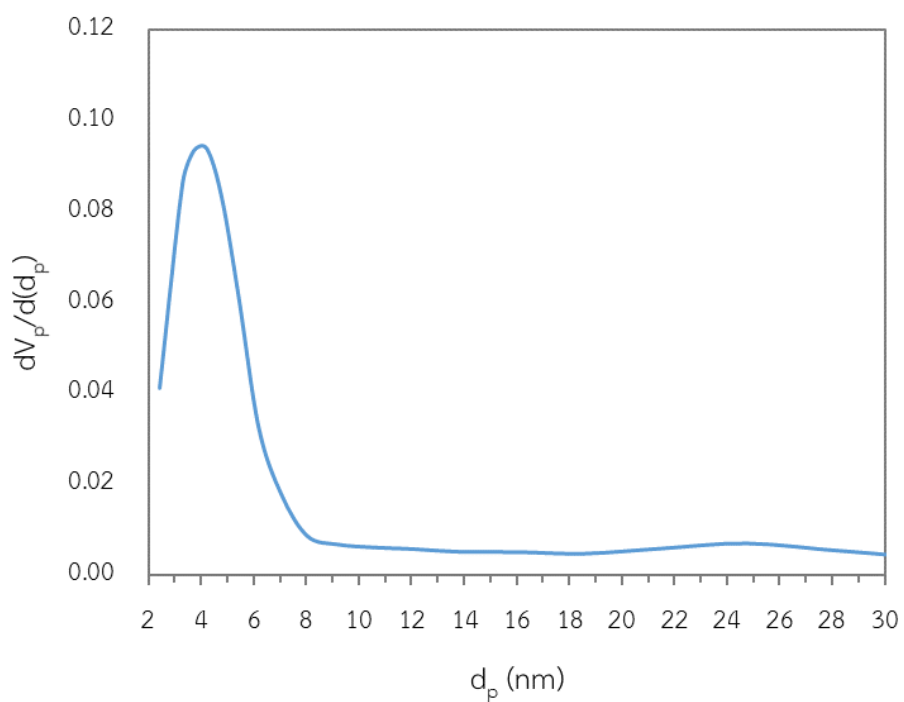
Figure 52 Pore diameter distribution of Ru/10%TiO$_2$-Al$_2$O$_3$ catalyst.
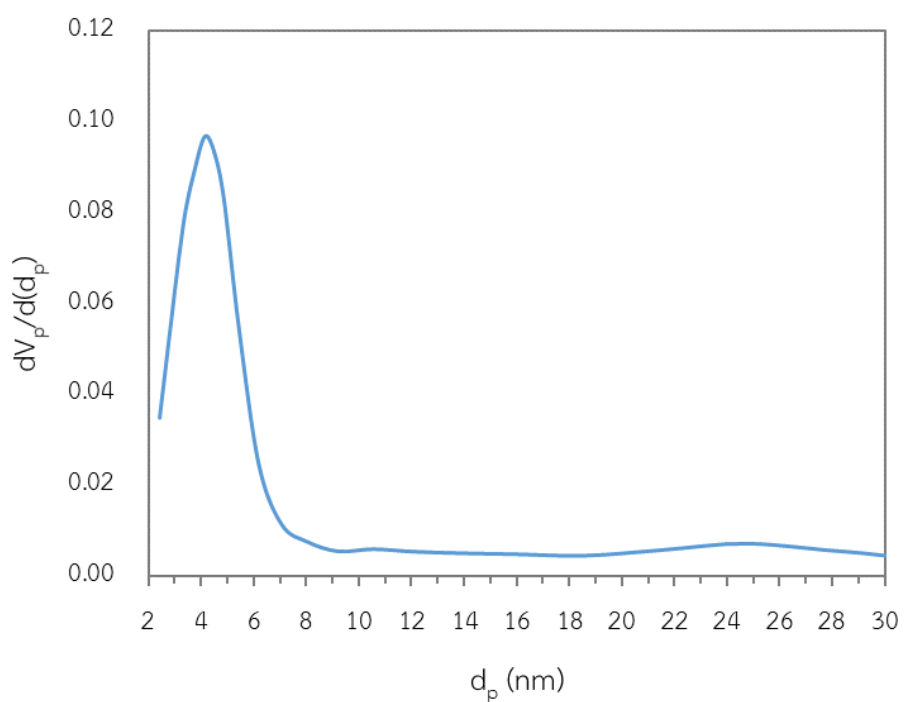
Figure 53 Pore diameter distribution of Ru/15%TiO$_2$-Al$_2$O$_3$ catalyst.
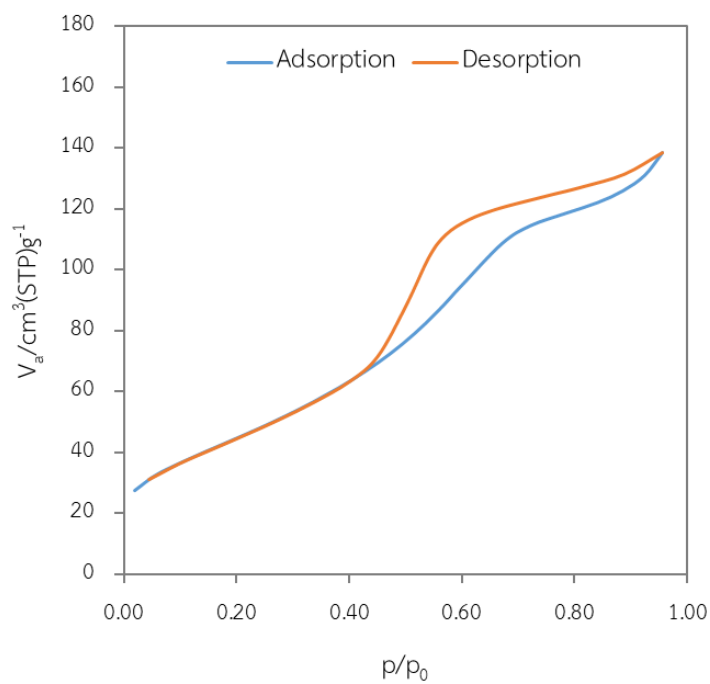
Figure 54 N_2 adsorption and desorption isotherm of RNN catalyst.
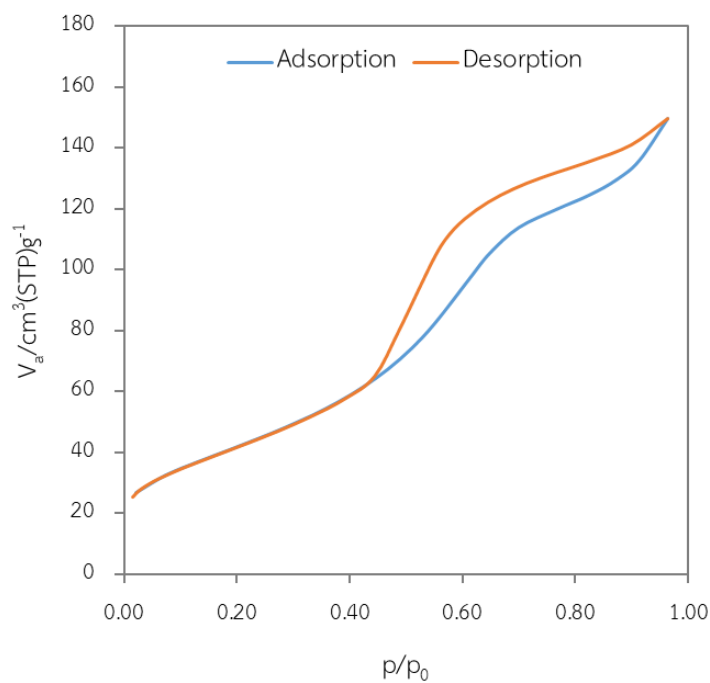
Figure 55 N_2 adsorption and desorption isotherm of Ru/Al$_2$O$_3$ (commercial) catalyst.
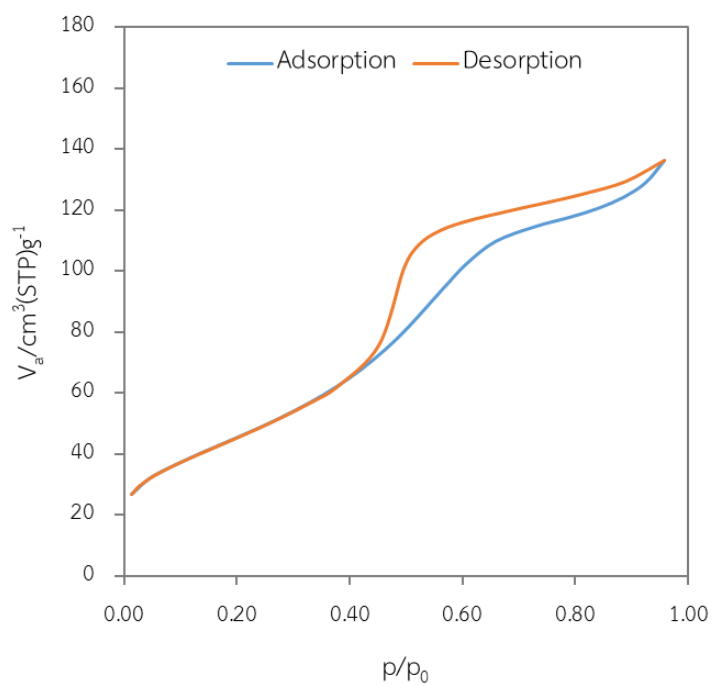
Figure 56 N_2 adsorption and desorption isotherm of Ru/2.5%TiO$_2$-Al$_2$O$_3$ catalyst.
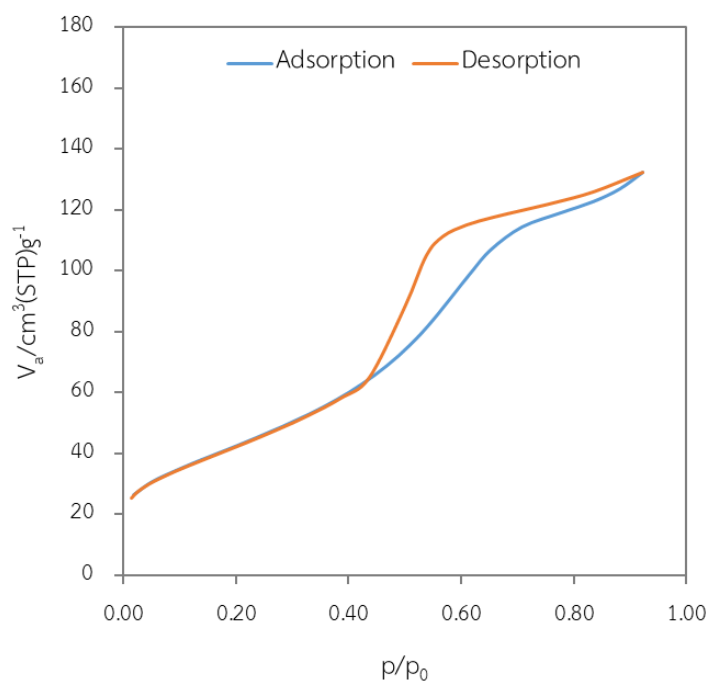
Figure 57 N_2 adsorption and desorption isotherm of Ru/5%TiO$_2$-Al$_2$O$_3$ catalyst.
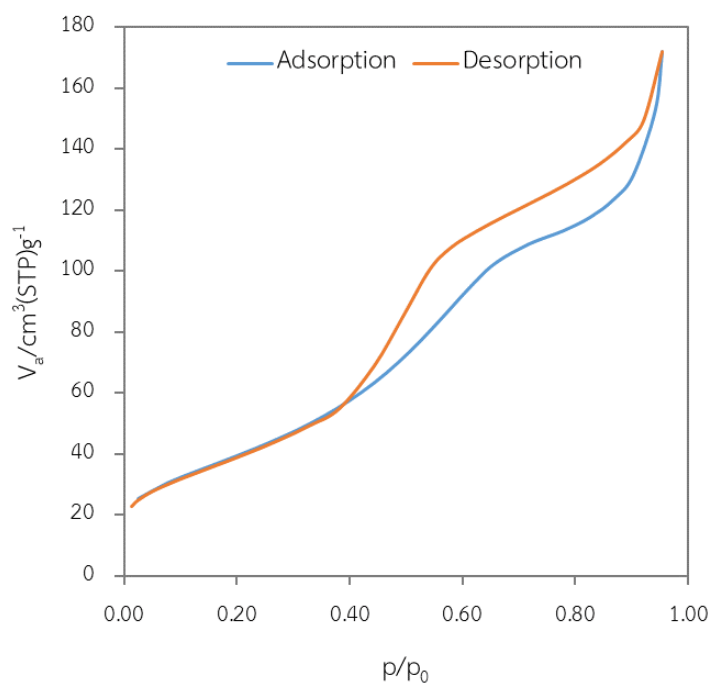
Figure 58 N_2 adsorption and desorption isotherm of Ru/10%TiO$_2$-Al$_2$O$_3$ catalyst.
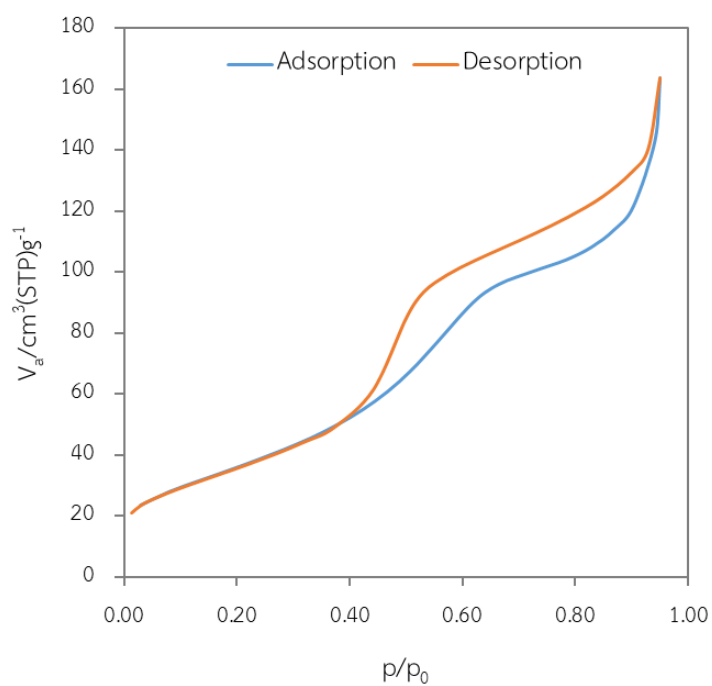
Figure 59 N_2 adsorption and desorption isotherm of Ru/10%TiO$_2$-Al$_2$O$_3$ catalyst.

Figure 60 shows XRD patterns of RNN, Ru/Al$_2$O$_3$ (Commercial) and Ru supported on various amount of TiO$_2$ in Al$_2$O$_3$ catalysts. The XRD patterns appeared

Catalyst	Crystallite size (nm)	% rutile-TiO$_2$

diffraction peaks of RuO$_2$ in all catalysts which the positions of diffraction peak of RuO$_2$ consisted to 2θ = 28°, 35° and 54.5° [4]. In the catalysts with TiO$_2$ presence, diffraction peaks of TiO$_2$ appeared anatase phase in all these catalysts which the main diffraction peak of TiO$_2$-anatase phase is 2θ = 25.3°. Moreover, diffraction peaks of TiO$_2$-rutile phase appeared only in Ru/10%TiO$_2$-Al$_2$O$_3$ and Ru/15%TiO$_2$-Al$_2$O$_3$ catalysts which the main diffraction peak is 2θ = 27.4° [66].
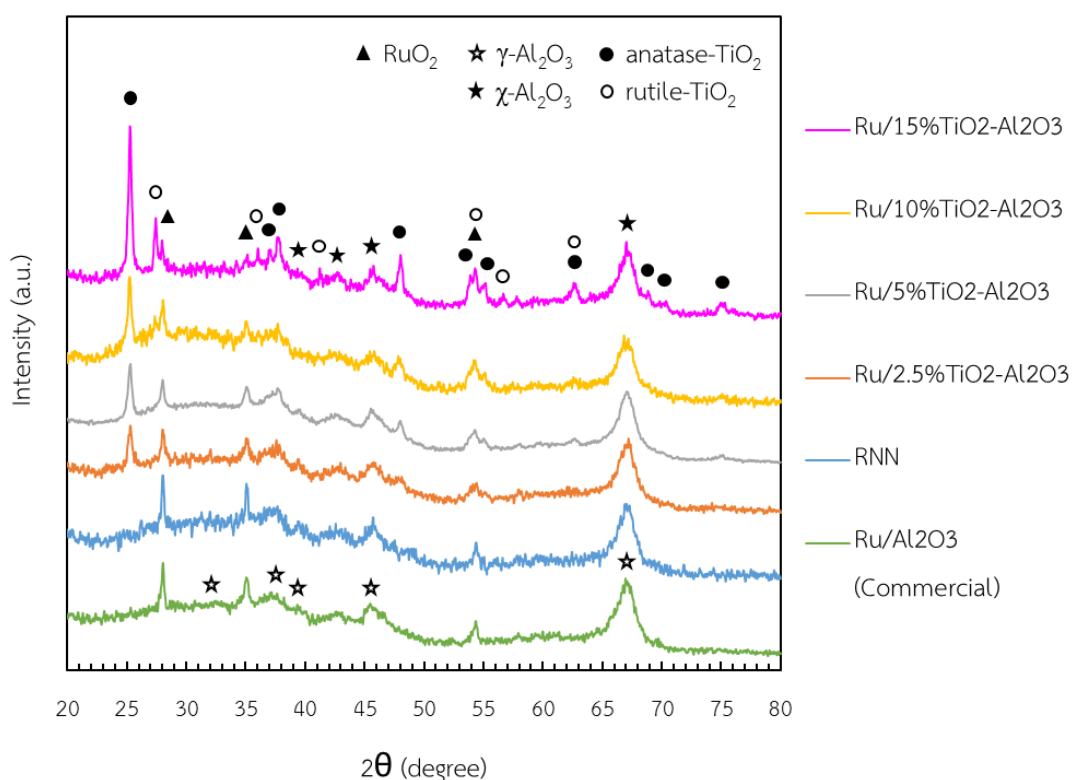
Figure 60 XRD pattern of RNN, Ru/Al$_2$O$_3$ (Commercial) and Ru/TiO$_2$-Al$_2$O$_3$ catalysts.

	RuO_2	Al_2O_3	anatase-TiO_2	rutile-TiO_2	
Ru/Al_2O_3 (Commercial)	31	5.6	-	-	-
RNN	31	6.3	-	-	-
Ru/2.5%TiO_2-Al_2O_3	31	5.9	18	N/A	-
Ru/5%TiO_2-Al_2O_3	25	6.0	21	N/A	-
Ru/10%TiO_2-Al_2O_3	22	6.3	24	24	48%
Ru/15%TiO_2-Al_2O_3	25	6.9	27	31	41%

Table 17 Crystallite size of RNN, Ru/Al_2O_3 (commercial) and Ru/TiO_2-Al_2O_3 catalysts calculated by XRD results.
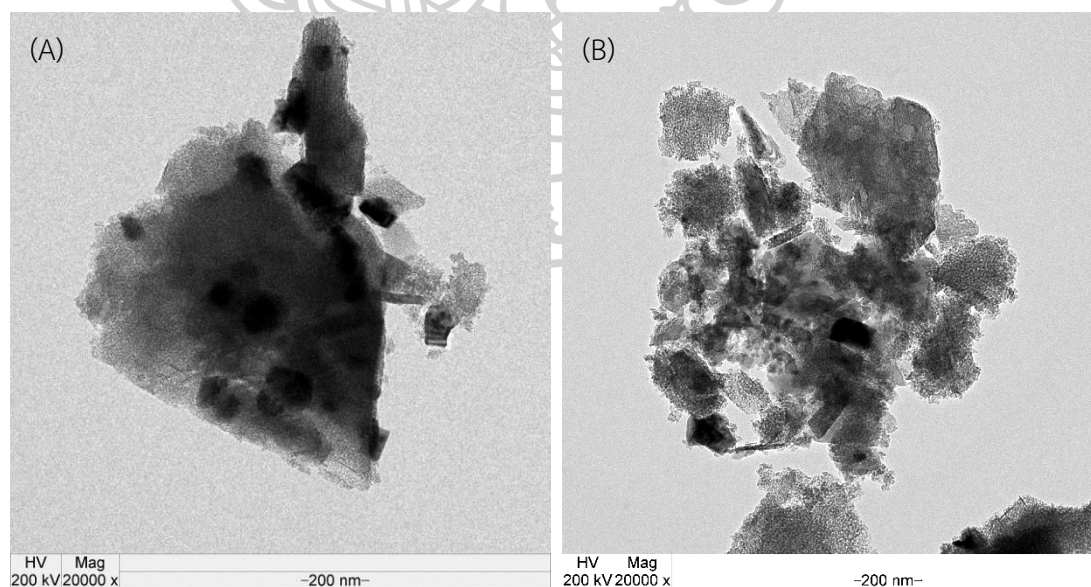
Figure 61 TEM images of (A) RNN and (B) Ru/Al_2O_3 (Commercial) catalysts.

Crystallite size of RNN, Ru/Al$_2$O$_3$ (Commercial) and Ru/TiO$_2$-Al$_2$O$_3$ catalysts calculated by XRD results is reported in **Table 17**. The presence of TiO$_2$ in catalysts results in a smaller RuO$_2$ crystallite size. In addition, Crystallite size of both anatase and rutile phase of TiO$_2$ increase with increasing TiO$_2$ loading. Content of rutile phase in TiO$_2$ is calculated from equation presented by Yuangpho N. et al. [66] which Ru/10%TiO$_2$-Al$_2$O$_3$ and Ru/15%TiO$_2$-Al$_2$O$_3$ catalysts have 48% and 41% of rutile phase. Whereas, crystallite size of TiO$_2$-rutile phase in the catalysts added small amount of TiO$_2$ cannot be calculated because their diffraction peaks are not appearing or too weak for calculation. From the results above, anatase phase of TiO$_2$ can transform to rutile phase with increasing TiO$_2$ loading.

Figure 61 and 62 show TEM images of RNN, Ru/Al$_2$O$_3$ (Commercial) and Ru/TiO$_2$-Al$_2$O$_3$ catalysts. Parts of deep black were assigned to RuO$_2$. In TEM images observed, RuO$_2$ particles was smaller with adding of TiO$_2$ in support and its particles size decreased with increasing amount of TiO$_2$ loading. Moreover, the RuO$_2$ particles of the catalyst with TiO$_2$ presence were seemed better dispersion than RNN catalyst. These results were similar to the results of crystallite size that was the RuO$_2$ crystallite size decreased with increasing TiO$_2$ loading. In Ru/2.5%TiO$_2$-Al$_2$O$_3$ catalyst, area cycled in TEM image was performed by EDS analysis that shown in **Figure 63**. The deep dark part in cycle was confirmed that Ru metal was primarily composed.
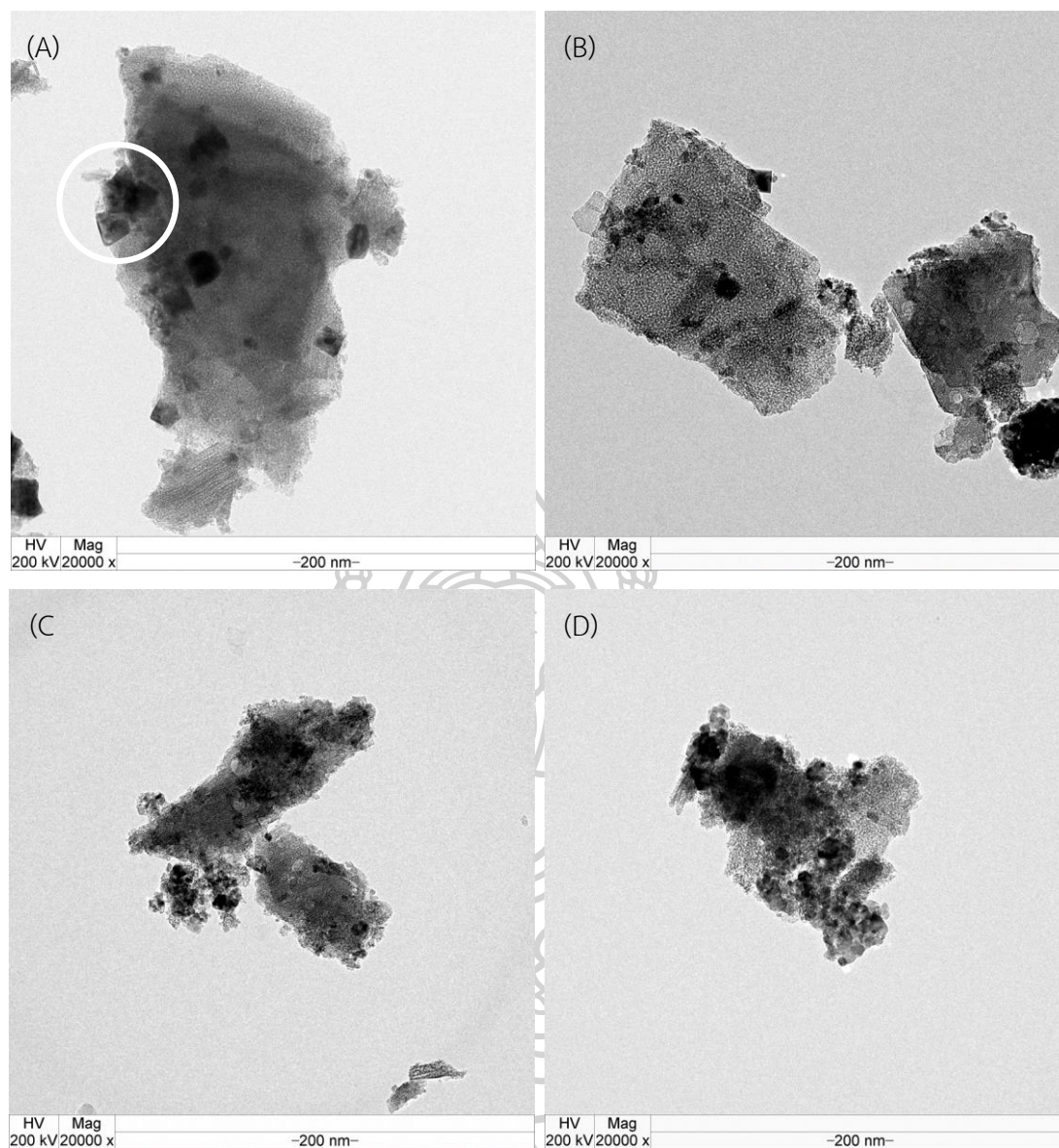
Figure 62 TEM images of Ru/TiO$_2$-Al$_2$O$_3$ catalysts seeing that (A) Ru/2.5%TiO$_2$-Al$_2$O$_3$ catalyst, (B) Ru/5%TiO$_2$-Al$_2$O$_3$ catalyst, (C) Ru/10%TiO$_2$-Al$_2$O$_3$ catalyst and (D) Ru/15%TiO$_2$-Al$_2$O$_3$ catalyst.
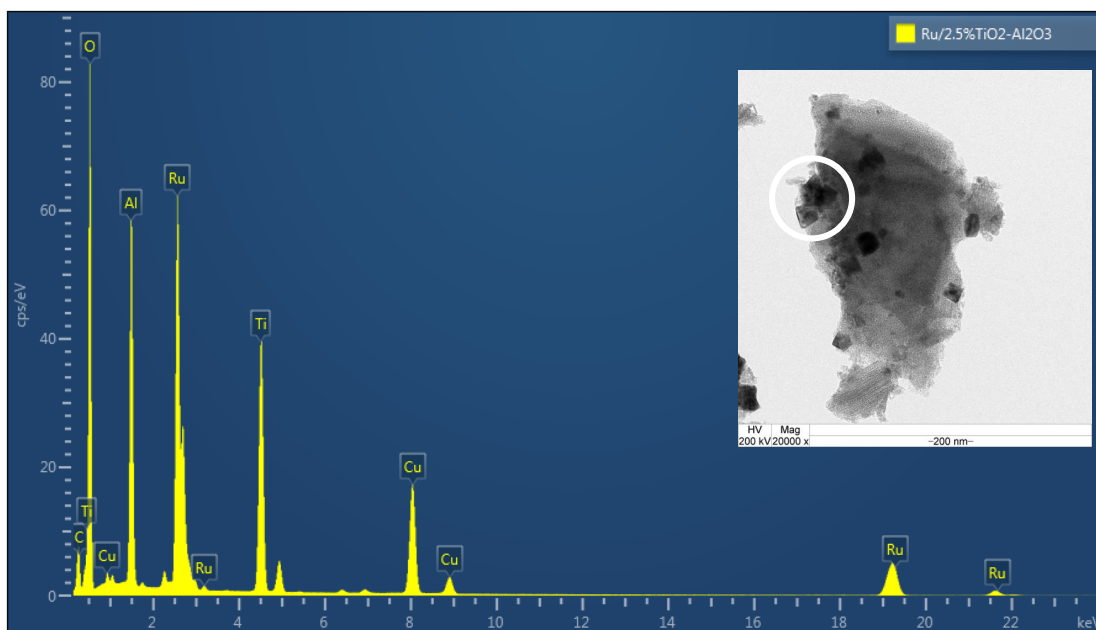
Figure 63 EDS spectra obtained at the area in cycle that presented in TEM image of Ru/2.5%TiO$_2$-Al$_2$O$_3$ catalyst.

Table 18 H$_2$ chemisorption results of RNN, Ru/Al$_2$O$_3$ (commercial) and Ru/TiO$_2$-Al$_2$O$_3$ catalysts.

Catalyst	Active site [μmol/g$_{cat.}$]	Ru dispersion [%]	Average diameter of Ru particles [nm]
Ru/Al$_2$O$_3$ (commercial)	3.0	3.1	29
RNN	3.0	3.0	30
Ru/2.5%TiO$_2$-Al$_2$O$_3$	3.5	3.5	26
Ru/5%TiO$_2$-Al$_2$O$_3$	4.7	4.7	19
Ru/10%TiO$_2$-Al$_2$O$_3$	3.6	3.7	24
Ru/15%TiO$_2$-Al$_2$O$_3$	3.7	3.7	24

Active site, Ru dispersion and average Ru particles diameter of RNN, Ru/Al$_2$O$_3$ (Commercial) and Ru/TiO$_2$-Al$_2$O$_3$ catalysts are shown in **Table 18**. In TiO$_2$ addition, their active site and Ru dispersion could increase. The maximum active site and also Ru dispersion were obtained by Ru/5%TiO$_2$-Al$_2$O$_3$ catalyst (4.7 μmol/g$_{cat}$ and 4.7%, respectively). Moreover, average Ru particles diameter of the Ru/5%TiO$_2$-Al$_2$O$_3$ catalyst was smallest of all catalysts with TiO$_2$ added and also smaller than RNN and Ru/Al$_2$O$_3$ (Commercial) catalysts. In an interesting, the amount of TiO$_2$ loading further increased was shown decreasing of active site and Ru dispersion.
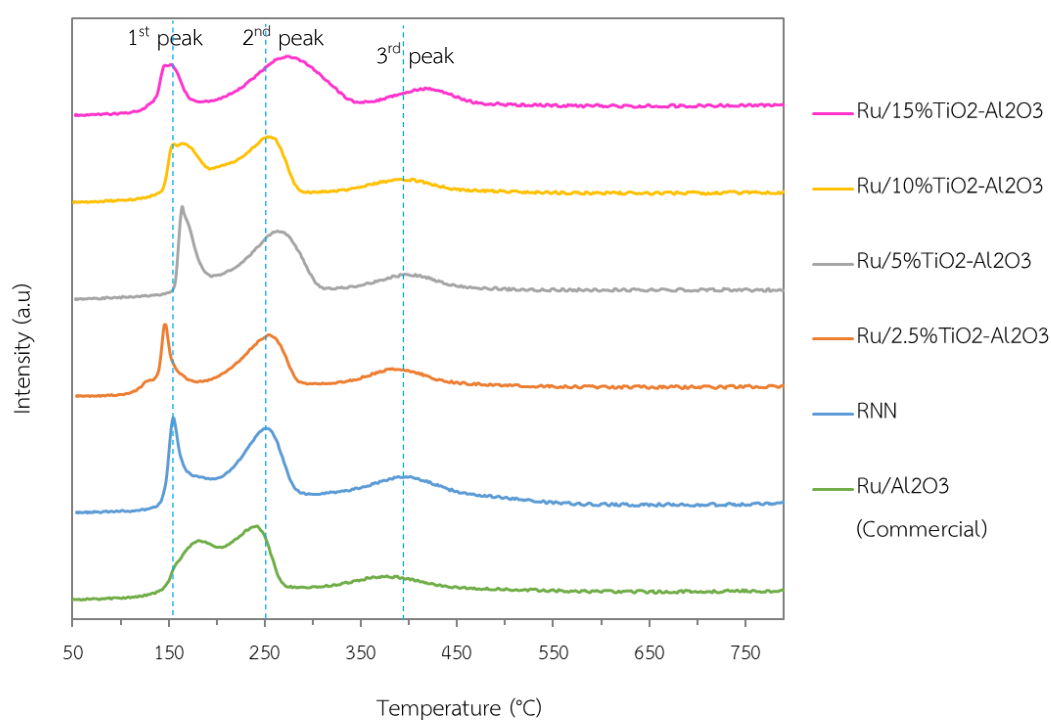
Figure 64 H$_2$-TPR profiles of RNN, Ru/Al$_2$O$_3$ (Commercial) and Ru/TiO$_2$-Al$_2$O$_3$ catalysts.

H$_2$-TPR profiles of RNN, Ru/Al$_2$O$_3$ (Commercial) and Ru/TiO$_2$-Al$_2$O$_3$ catalysts are shown in **Figure 64**. It was clear that consisted a low temperature reduction peak, a medium temperature reduction peak and a broad high temperature reduction peak. Accordance with the results reported in literatures [59, 61-63], the first reduction peak at low reduction temperature attributed to the reduction steps from RuO$_2$ to RuO and RuO to Ru^0 at medium reduction temperature or second reduction peak. The broad reduction peak at high temperature might be assigned to the oxidized Ru species reduction that interaction strongly with support. In an observation, the second and third reduction peaks were shifted toward higher reduction temperature when TiO$_2$ added into the support. Moreover, Ru/15%TiO$_2$-Al$_2$O$_3$ catalyst indicated that two peaks at high reduction temperature were more shifted to high reduction temperature than other Ru catalysts with TiO$_2$ loading due to Ru was more interacted the binary oxides support.

5.3.2 Catalytic activity test

Ru catalysts supported on various amount of TiO$_2$ in χ-Al$_2$O$_3$ are investigated in CO$_2$ hydrogenation reaction. Feed gases mixed are consisted 12.5% CO$_2$, 50% H$_2$ (4H$_2$/1CO$_2$) with He balancing. GHSV of 14,416 h^{-1} is used in this investigation. The results of Ru/TiO$_2$-Al$_2$O$_3$ catalysts are compared to Ru/χ-Al$_2$O$_3$ (or RNN) and Ru/γ-Al$_2$O$_3$ (or Ru/Al$_2$O$_3$ (Commercial)) catalysts.

CO$_2$ conversion as function of reaction temperature of RNN, Ru/Al$_2$O$_3$ (Commercial) and Ru/TiO$_2$-Al$_2$O$_3$ catalysts is illustrated in **Figure 65**. In TiO$_2$ added in support, its CO$_2$ conversion was higher than RNN catalyst and also increased with increasing TiO$_2$ loading. In an interesting, the maximum CO$_2$ conversion of large amount of TiO$_2$ loading could shift to lower reaction temperature. Moreover, Ru/5%TiO$_2$-Al$_2$O$_3$ catalyst gave the maximum CO$_2$ conversion and it could approach equilibrium more than other all catalysts.
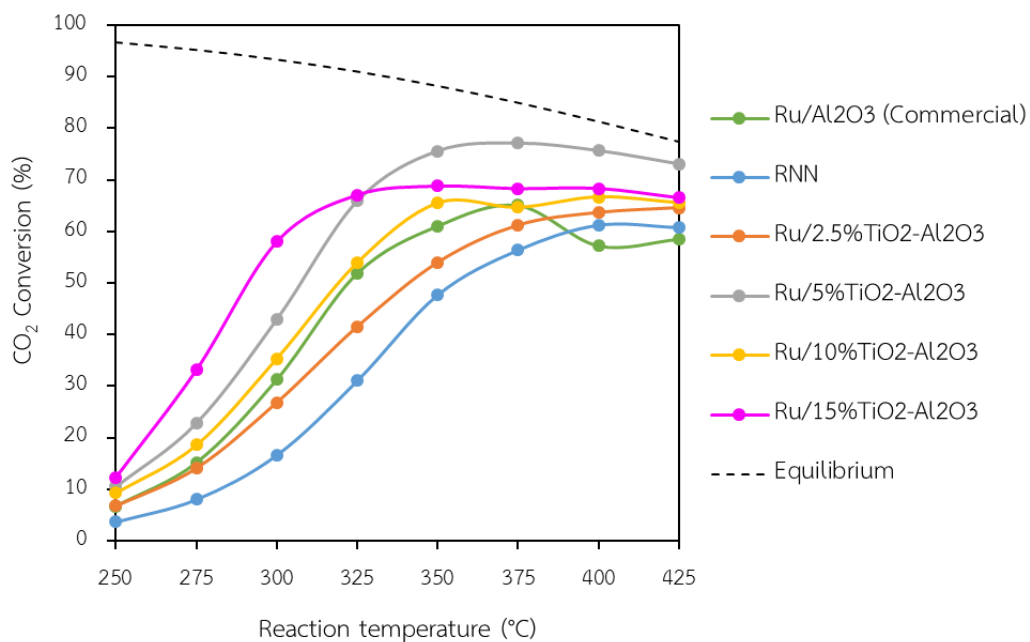
Figure 65 CO_2 conversion as function of reaction temperature of RNN, Ru/Al_2O_3 (Commercial) and Ru/TiO_2-Al_2O_3 catalysts.
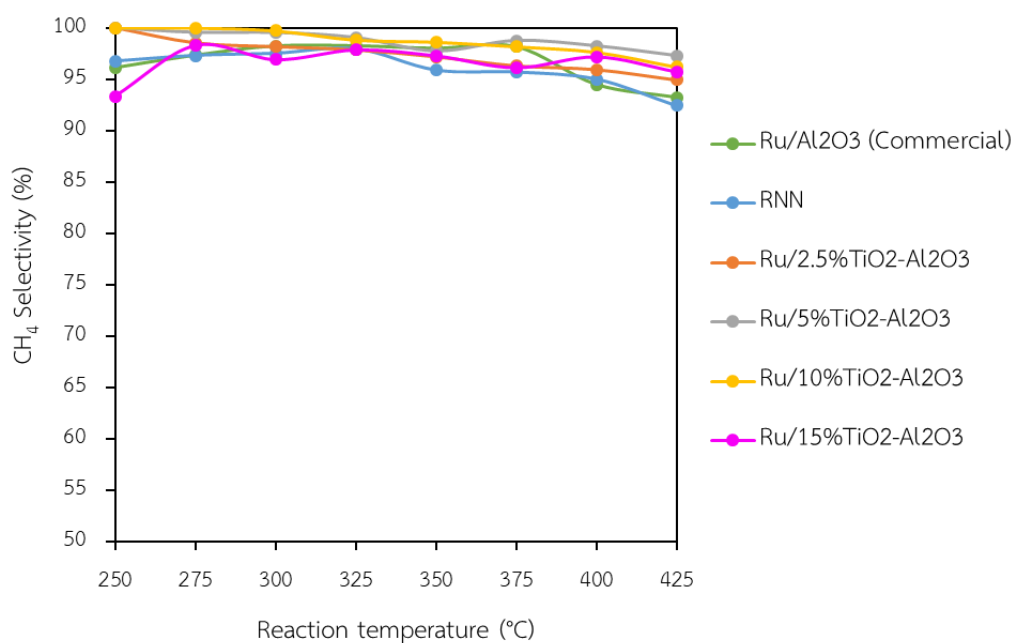
Figure 66 CH_4 selectivity as function of reaction temperature of RNN, Ru/Al_2O_3 (Commercial) and Ru/TiO_2-Al_2O_3 catalysts.
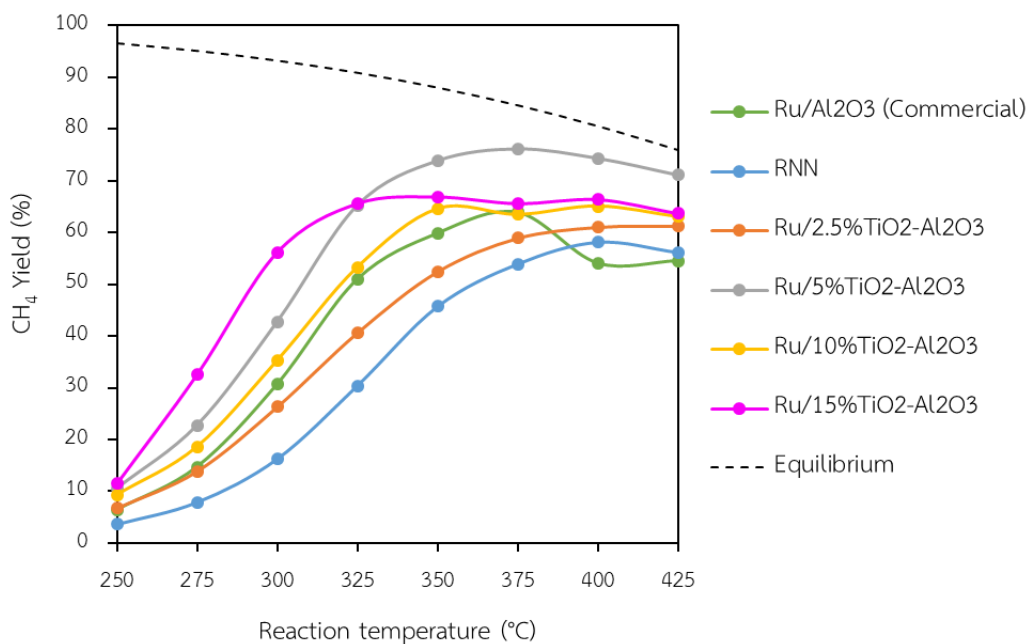
Figure 67 CH_4 yield as function of reaction temperature of RNN, Ru/Al_2O_3 (Commercial) and Ru/TiO_2-Al_2O_3 catalysts.
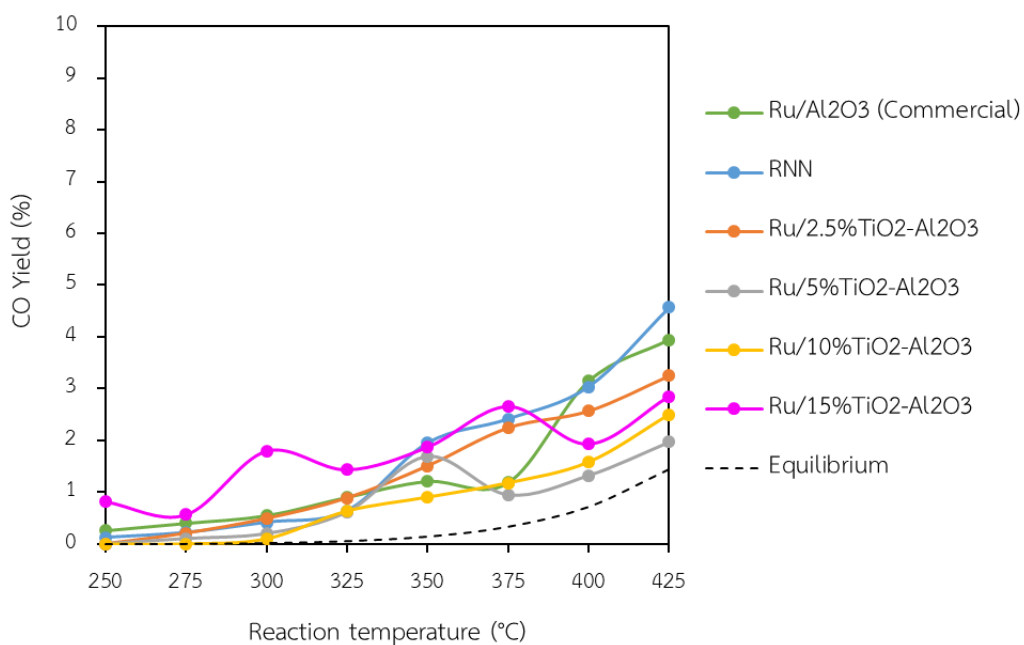
Figure 68 CO yield as function of reaction temperature of RNN, Ru/Al_2O_3 (Commercial) and Ru/TiO_2-Al_2O_3 catalysts.

CH_4 selectivity of RNN, Ru/Al_2O_3 (Commercial) and Ru/TiO_2-Al_2O_3 catalysts, and reaction temperature are plotted in **Figure 66**. The CH_4 selectivity of all catalysts could almost reach to 100% at every reaction temperature. **Figure 67 and 68** exhibit plots between CH_4 yield and CO yield with reaction temperature. The CH_4 yield of all catalysts increased rapidly with increasing reaction temperature and slowed down when approaching the equilibrium. The CH_4 yield curve of TiO_2-promoted catalyst shifted toward lower reaction temperature than RNN catalyst. Moreover, the CH_4 yield decreased in order of $Ru/5\%TiO_2$-Al_2O_3 > $Ru/15\%TiO_2$-Al_2O_3 > $Ru/10\%TiO_2$-Al_2O_3 > Ru/Al_2O_3 (Commercial) > $Ru/2.5\%TiO_2$-Al_2O_3 > RNN catalysts which obtained at reaction temperature of 350°C. The maximum CH_4 yield of $Ru/5\%TiO_2$-Al_2O_3 catalyst was about 76% at 375°C, and then, it decreased with further increasing of reaction temperature. This probably due to the deactivation of catalyst. In addition, CO yield of all catalysts increased with increasing reaction temperature and did not more than 5% of CO yield. In an interesting, the addition of TiO_2 in support could reduce the amount of CO yield.

Plots between rate of CH_4 formation of RNN, Ru/Al_2O_3 (Commercial) and Ru/TiO_2-Al_2O_3 catalysts, and reaction temperature are exhibited in **Figure 69**. In an observation, the amount of CH_4 formation per gram catalyst with TiO_2 presence was more than Ru catalyst without TiO_2 added. These results of CH_4 formation rate could confirm the description above that the addition of TiO_2 in support promoted CH_4 formation. In $Ru/5\%TiO_2$-Al_2O_3 catalyst, it could get the maximum rate of CH_4 formation due to the amount of its active site was more than all catalysts that could be seen in H_2 chemisorption result.

Turnover frequencies (TOF) of CO_2 conversion are displayed in **Figure 70** which showing linearity in reaction temperature of 250 – 325°C. In an observation, the TOF of $Ru/15\%TiO_2$-Al_2O_3 catalyst was obviously higher other all catalysts probably due to it had stronger interaction between Ru and binary oxides support. Decreasing order of TOF was followed as $Ru/15\%TiO_2$-Al_2O_3 > $Ru/10\%TiO_2$-Al_2O_3 ~ $Ru/5\%TiO_2$-Al_2O_3 > Ru/Al_2O_3 (Commercial) > $Ru/2.5\%TiO_2$-Al_2O_3 > RNN catalysts.
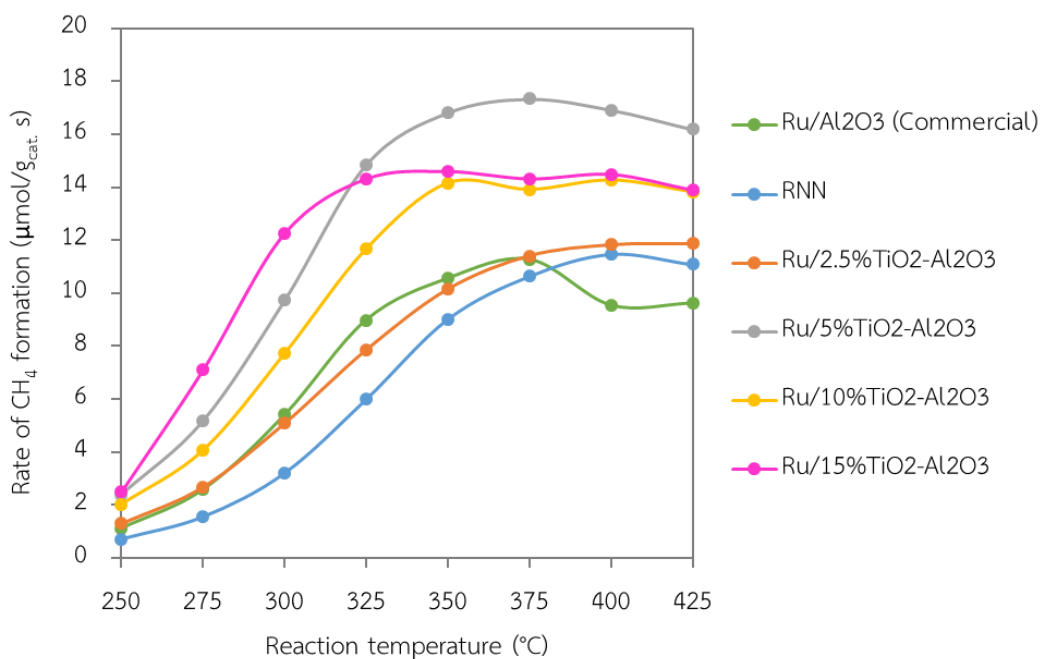
Figure 69 Rate of CH_4 formation as function of reaction temperature of RNN, Ru/Al$_2$O$_3$ (Commercial) and Ru/TiO$_2$-Al$_2$O$_3$ catalysts.
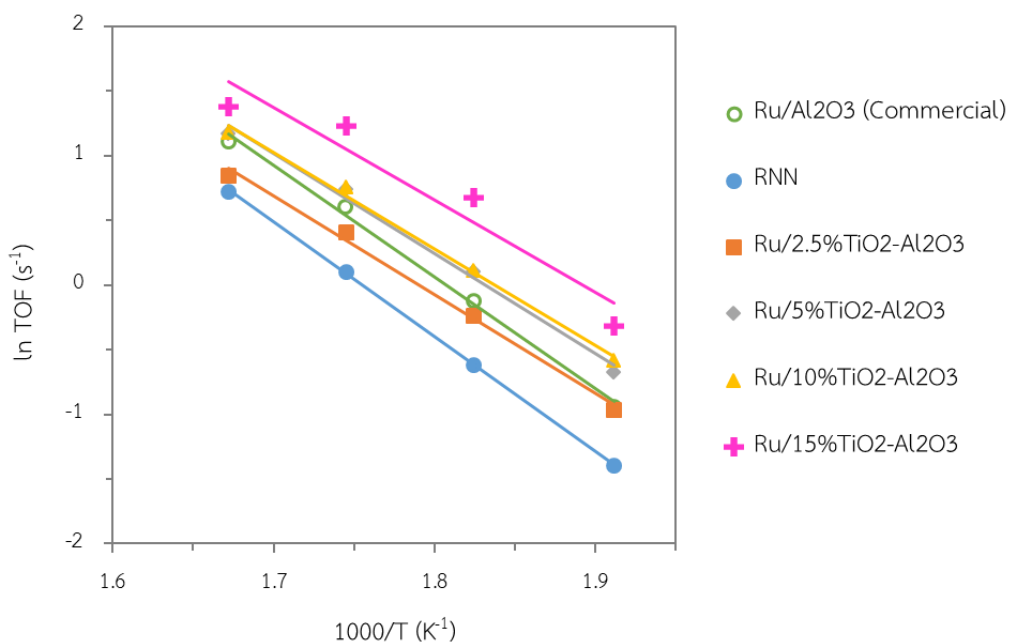

Figure 70 Turnover frequency (TOF) of CO_2 conversion obtained from RNN, Ru/Al$_2$O$_3$ (Commercial) and Ru/TiO$_2$-Al$_2$O$_3$ catalysts.

Table 19 Apparent activation energy (E_a) of CO_2 hydrogenation reaction obtained from RNN, Ru/Al_2O_3 (Commercial) and Ru/TiO_2-Al_2O_3 catalysts.

Catalyst	E_a [kJ/mol]
Ru/Al_2O_3 (Commercial)	78
RNN	75
$Ru/2.5\%TiO_2$-Al_2O_3	70
$Ru/5\%TiO_2$-Al_2O_3	74
$Ru/10\%TiO_2$-Al_2O_3	66
$Ru/15\%TiO_2$-Al_2O_3	94

Apparent activation energies (E_a) of RNN, Ru/Al_2O_3 (Commercial) and Ru/TiO_2-Al_2O_3 catalysts in CO_2 hydrogenation reaction are shown in **Table 19**. It could be calculated from slopes of fitted linear curves [67]. The E_a values of all catalysts were similar to results of Ru/Al_2O_3 catalyst in CO_2 hydrogenation reaction [51].

5.4 Comparison of catalytic activity of ZrO_2-Al_2O_3 and TiO_2-Al_2O_3 supported Ru catalysts.

In this section, $Ru/10\%ZrO_2$-Al_2O_3 and $Ru/20\%ZrO_2$-Al_2O_3 catalysts are compared with $Ru/5\%TiO_2$-Al_2O_3 and $Ru/15\%TiO_2$-Al_2O_3 catalysts and also RNN catalyst. This comparison is determined in rate of CH_4 formation and turnover frequency (TOF) of those catalysts. Feed gases composition used is 12.5% CO_2, 50% H_2 ($4H_2/1CO_2$) with He balancing. GHSV of 14,416 h^{-1} is used in this investigation.
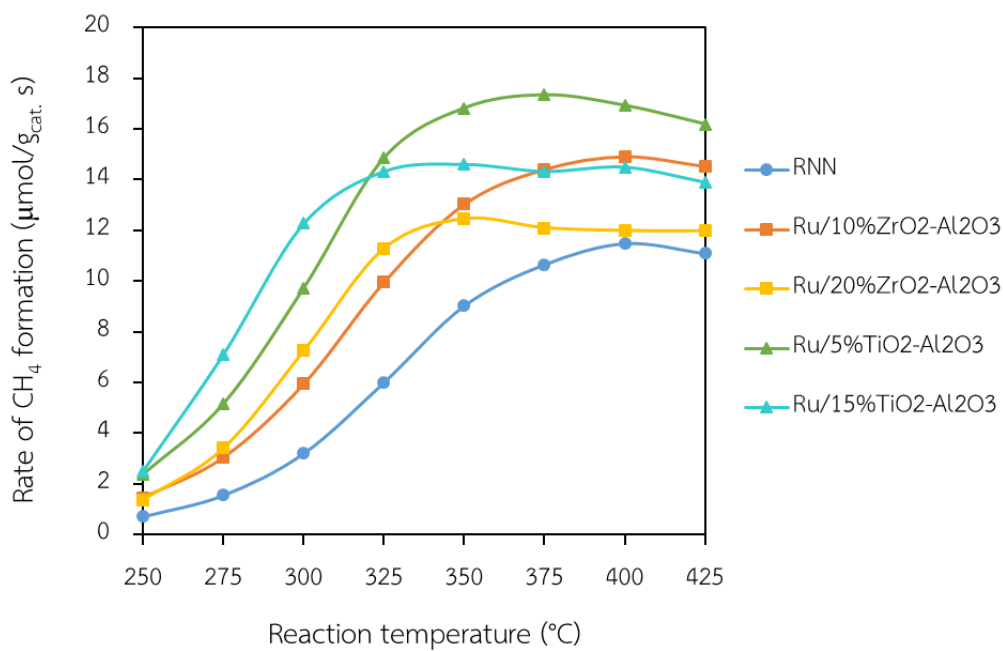
Figure 71 Rate of CH_4 formation as function of reaction temperature of $Ru/10\%ZrO_2$-Al_2O_3, $Ru/20\%ZrO_2$-Al_2O_3, $Ru/5\%TiO_2$-Al_2O_3, $Ru/15\%TiO_2$-Al_2O_3 and RNN catalysts.
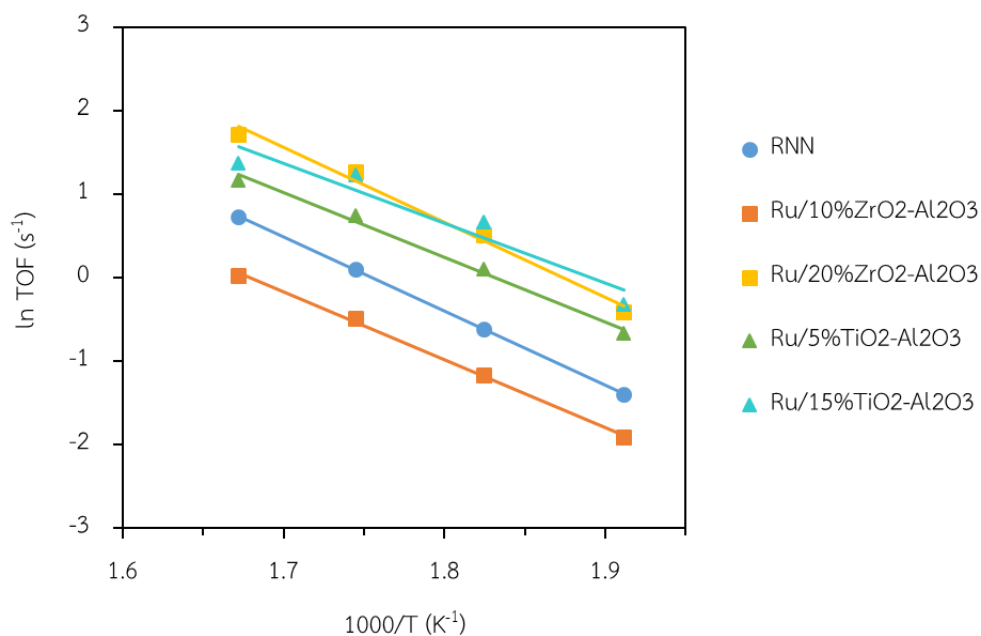
Figure 72 Turnover frequency (TOF) of CO_2 conversion obtained from $Ru/10\%ZrO_2$-Al_2O_3, $Ru/20\%ZrO_2$-Al_2O_3, $Ru/5\%TiO_2$-Al_2O_3, $Ru/15\%TiO_2$-Al_2O_3 and RNN catalysts.

Plot of CH_4 formation rate versus reaction temperature of Ru/10%ZrO_2-Al_2O_3, Ru/20%ZrO_2-Al_2O_3, Ru/5%TiO_2-Al_2O_3, Ru/15%TiO_2-Al_2O_3 and RNN catalysts is indicated in **Figure 71**. It observed that both ZrO_2 loading and TiO_2 loading in Ru catalysts were higher rate of CH_4 formation than RNN catalyst. Moreover, Ru catalysts with TIO_2 presence could give CH_4 formation rate more than Ru catalyst with ZrO_2 presence.

In **Figure 72** indicate turnover frequency (TOF) of CO_2 conversion over Ru/10%ZrO_2-Al_2O_3, Ru/20%ZrO_2-Al_2O_3, Ru/5%TiO_2-Al_2O_3, Ru/15%TiO_2-Al_2O_3 and RNN catalysts. The TOF values of Ru/20%ZrO_2-Al_2O_3 catalyst were not much with those of Ru/15%TiO_2-Al_2O_3 catalyst and the TOF values were followed in order of Ru/20%ZrO_2-Al_2O_3 ∼ Ru/15%TiO_2-Al_2O_3 > Ru/5%TiO_2-Al_2O_3 > RNN > Ru/10%ZrO_2-Al_2O_3 catalysts.
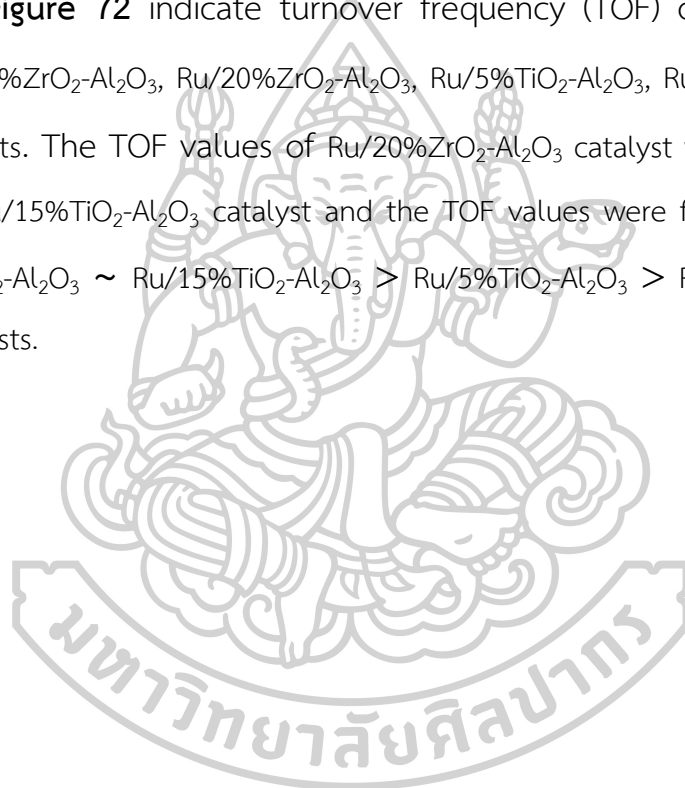
CHAPTER VI

CONCLUSIONS AND RECOMMENDATIONS

6.1 Conclusion

6.1.1 Effect of ruthenium precursors

In this study, 1 wt.% Ru catalyst supported on χ-Al_2O_3 was prepared by incipient wetness impregnation method. Effect of three different ruthenium precursors including ruthenium (III) nitrosyl nitrate solution, ruthenium (III) acetylacetonate and Hexaammineruthenium (III) chloride used in catalytic preparation was investigated, which denoted as RNN, RAA and RCl catalysts. The RNN and RAA catalysts gave high active site and Ru dispersion, whereas, the active site of RCl catalyst could not determine. CO_2 conversion and selectivity of RNN and RAA catalysts were almost similar and higher than that of RCl catalyst, moreover, CH_4 yield of RNN and RAA catalysts were 2 times higher than RCl catalyst at reaction temperature of 400°C. The worst results of RCl was probably due to residual chlorine covered on the catalyst surface, which inhibited the adsorption of CO_2 and H_2 molecules.

6.1.2 Effect of ZrO_2 addition in χ-Al_2O_3 supported Ru catalyst

ZrO_2-Al_2O_3 with different Zr loading content varied as 5, 10, 15 and 20 wt.%. was used as the support for Ru catalyst. The addition of ZrO_2 could improve active site and Ru dispersion of Ru/χ-Al_2O_3 catalyst, moreover, Ru/10%ZrO_2-Al_2O_3 catalyst gave the highest active site and Ru dispersion (9.7 μmol/$g_{cat.}$ and 9.8%, respectively). In addition, Ru catalysts added with ZrO_2 could affect the interaction between Ru and binary oxides support. The Ru/ZrO_2-Al_2O_3 promoted CO_2 conversion and CH_4 yield. In addition of large amount of ZrO_2 to Ru catalysts (Ru/20%ZrO_2-Al_2O_3 catalyst),

it gave values of TOF more than Ru catalysts with other support due to the interaction between Ru and binary oxides support was stronger than other catalysts.

6.1.3 Effect of TiO_2 addition in χ-Al_2O_3 supported Ru catalyst

Ru catalyst supported on TiO_2-Al_2O_3 was different Ti loading content varied as 2.5, 5, 10 and 15 wt.% was investigated in this part. The Ru/TiO_2-Al_2O_3 exhibited higher active site, Ru dispersion and smaller RuO_2 particles size, and at the same time, the addition of TiO_2 in the Ru catalysts could improve interaction between Ru and binary oxides support. Moreover, the Ru catalysts with TiO_2 presence could give higher CH_4 formation rate than Ru catalyst without TiO_2 loading. The TOF values of large amount of TiO_2 loaded in Ru catalyst (Ru/15%TiO_2-Al_2O_3 catalyst) were higher than Ru catalysts with other support because Ru was stronger interact to binary oxides support than other Ru catalysts.

6.1.4 Comparison of catalytic activity of ZrO_2-Al_2O_3 and TiO_2-Al_2O_3 supported Ru catalysts.

Ru catalysts supported on 10%ZrO_2-Al_2O_3 and 20%ZrO_2-Al_2O_3 were compared with Ru catalysts supported on 5%TiO_2-Al_2O_3, 15%ZrO_2-Al_2O_3 and also Ru/χ-Al_2O_3 catalyst. The addition of Ti and Zr in Ru catalysts could give better rate of CH_4 formation than Ru/χ-Al_2O_3 catalyst. Moreover, Ru/TiO_2-Al_2O_3 catalysts could show higher CH_4 formation rate than Ru/ZrO_2-Al_2O_3 catalysts.

APPENDIX A

CALCULATION OF CATALYTIC PREPARATION

A.1 Calculation of support preparation

A.1.1 Calculation of ZrO_2/Al_2O_3 support preparation

Example: Preparation of 15% ZrO_2 supported on Al_2O_3 by wet impregnation.

In this preparation, properties information used for calculation is followed below.

— Formula of zirconium n-butoxide (ZNB) = $C_{16}H_{36}O_4Zr$

— Purity of zirconium n-butoxide solution = 80% w/w

— Density of zirconium n-butoxide solution (ρ_{ZNB}) = 1.07 g/ml

— Molecular weight of zirconium n-butoxide (MW_{ZNB}) = 383.68 g/mol

— Molecular weight of zirconium dioxide (MW_{ZrO2}) = 123.22 g/mol

— Molecular weight of gibbsite (MW_{GB}) = 155.96 g/mol

— Molecular weight of aluminum oxide (MW_{Al2O3}) = 101.96 g/mol

Basis: Total weight of ZrO_2/Al_2O_3 = 2 g

Volume of zirconium n-butoxide solution (V_{ZNB}) is calculated by

$$m_{ZrO2} = (2 \text{ g } ZrO_2/Al_2O_3) \times \frac{(15 \text{ g } ZrO_2)}{(100 \text{ g } ZrO_2/Al_2O_3)} = 0.30 \text{ g}$$

$$m_{ZNB \text{ sol.}} = 0.30 \text{ g } ZrO_2 \left| \frac{383.68 \text{ g/mol ZNB}}{123.22 \text{ g/mol } ZrO_2} \right| \frac{1 \text{ mol ZNB}}{1 \text{ mol } ZrO_2} \left| \frac{1 \text{ g ZNB sol.}}{0.8 \text{ g ZNB}} \right.$$

$\therefore m_{ZNB \text{ sol.}} = 1.17 \text{ g}$

$$V_{ZNB\ sol.} = \frac{m_{ZNB\ sol.}}{\rho_{ZNB}} = \frac{1.17\ g}{1.07\ g/ml} = 1.09\ ml$$

Weight of gibbsite is calculated by

$$m_{Al2O3} = (2\ g\ ZrO_2/Al_2O_3) \times \frac{(75\ g\ Al_2O_3)}{(100\ g\ ZrO_2/Al_2O_3)} = 1.70\ g$$

$$m_{GB} = 1.7\ g\ Al_2O_3 \left| \frac{155.96\ g/mol\ GB}{101.96\ g/mol\ Al_2O_3} \right| \frac{1\ mol\ GB}{1\ mol\ Al_2O_3}$$

$$\therefore m_{GB} = 2.60\ g\ GB$$

A.1.2 Calculation of TiO_2/Al_2O_3 support preparation

Example: Preparation of 15% TiO_2 supported on Al_2O_3 by wet impregnation.

In this preparation, properties information used for calculation is followed below.

- Formula of titanium (IV) butoxide (TNB) = $Ti(OCH_2CH_2CH_2CH_3)_4$
- Purity of titanium (IV) butoxide solution = 97% w/w
- Density of titanium (IV) butoxide solution = 1.00 g/ml
- Molecular weight of titanium (IV) butoxide (MW_{TNB}) = 340.32 g/mol
- Molecular weight of titanium dioxide (MW_{TiO2}) = 79.87 g/mol
- Molecular weight of gibbsite (MW_{GB}) = 155.96 g/mol
- Molecular weight of aluminum oxide (MW_{Al2O3}) = 101.96 g/mol

Basis: Total weight of TiO_2/Al_2O_3 = 2 g

Volume of titanium (IV) butoxide solution (V_{TNB}) is calculated by

$$m_{TiO2} = (2 \text{ g } TiO_2/Al_2O_3) \times \frac{(15 \text{ g } TiO_2)}{(100 \text{ g } TiO_2/Al_2O_3)} = 0.30 \text{ g}$$

$$m_{TNB \text{ sol.}} = 0.30 \text{ g } TiO_2 \left| \frac{340.32 \text{ g/mol TNB}}{79.87 \text{ g/mol } TiO_2} \right| \frac{1 \text{ mol TNB}}{1 \text{ mol } TiO_2} \left| \frac{1 \text{ g TNB sol.}}{0.97 \text{ g TNB}} \right.$$

$\therefore m_{TNB \text{ sol.}} = 1.32 \text{ g}$

$$V_{TNB \text{ sol.}} = \frac{m_{TNB \text{ sol.}}}{\rho_{TNB}} = \frac{1.32 \text{ g}}{1.00 \text{ g/ml}} = 1.32 \text{ ml}$$

Weight of gibbsite is calculated by

$$m_{Al2O3} = (2 \text{ g } ZrO_2/Al_2O_3) \times \frac{(75 \text{ g } Al_2O_3)}{(100 \text{ g } ZrO_2/Al_2O_3)} = 1.70 \text{ g}$$

$$m_{GB} = 1.7 \text{ g } Al_2O_3 \left| \frac{155.96 \text{ g/mol GB}}{101.96 \text{ g/mol } Al_2O_3} \right| \frac{1 \text{ mol GB}}{1 \text{ mol } Al_2O_3}$$

$\therefore m_{GB} = 2.60 \text{ g GB}$

A.2 Calculation of catalytic preparation

Example: Preparation of 1% Ru supported on χ-Al_2O_3 by incipient wetness impregnation with Ruthenium (III) nitrosyl nitrate precursor.

In this preparation, properties information used for calculation is followed below.

— Formula of ruthenium (III) nitrosyl nitrate (RNN) = $Ru(NO)(NO_3)_x(OH)_y$, $x + y = 3$

— Purity of ruthenium (III) nitrosyl nitrate solution = 1.5% (typical)

— Density of ruthenium (III) nitrosyl nitrate solution (ρ_{RNN}) = 1.07 g/ml

Basis: Total weight of support = 2 g

Volume of ruthenium (III) nitrosyl nitrate solution (V_{RNN}) is calculated by

$$m_{RNN\ sol.} = 2\ g\ Al_2O_3 \left| \frac{0.01\ g\ Ru}{0.99\ g\ Al_2O_3} \right| \frac{98.5\ g\ RNN\ sol.}{1.5\ g\ Ru}$$

$$\therefore\ m_{RNN\ sol.} = 1.33\ g$$

$$V_{RNN\ sol.} = \frac{m_{RNN\ sol.}}{\rho_{RNN}} = \frac{1.33\ g}{1.07\ g/ml} = 1.24\ ml$$

APPENDIX B

CALCULATION OF CRYSTALLITE SIZE

The Scherrer's equation is used to estimate the average crystallite size that shown in Eq. (B.1).
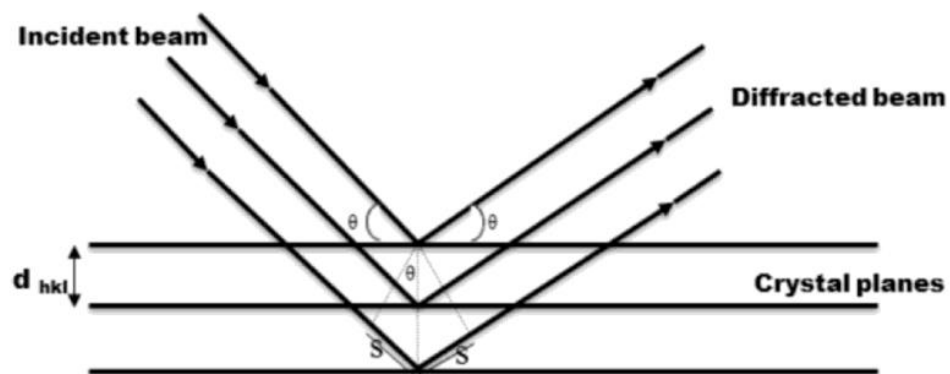
Figure 73 Observing the crystal plane of diffraction phenomenon [68].

The Scherrer's equation:

$$D = \frac{K\lambda}{\beta \cos\theta} \tag{B.1}$$

Where   D is crystallite size, Å.

K is constant dependent on crystallite shape = 0.9.

λ is x-ray wavelength = 1.54 Å (for CuKα).

β is the full width at half maximum which can be calculated by Warren's formula.

θ is Bragg angle.

The Warren's formula is used for β calculation that showed in Eq. (B.2).

$$\beta^2 = \beta_M^2 - \beta_S^2 \qquad\qquad (B.2)$$

Where β_M and β_S are the full width at half maximum in radians for the sample and standard, respectively. The β_S can be get from **Figure B.2**. This graph is the full width at half maximum in radians for α-Al$_2$O$_3$ that used as standard
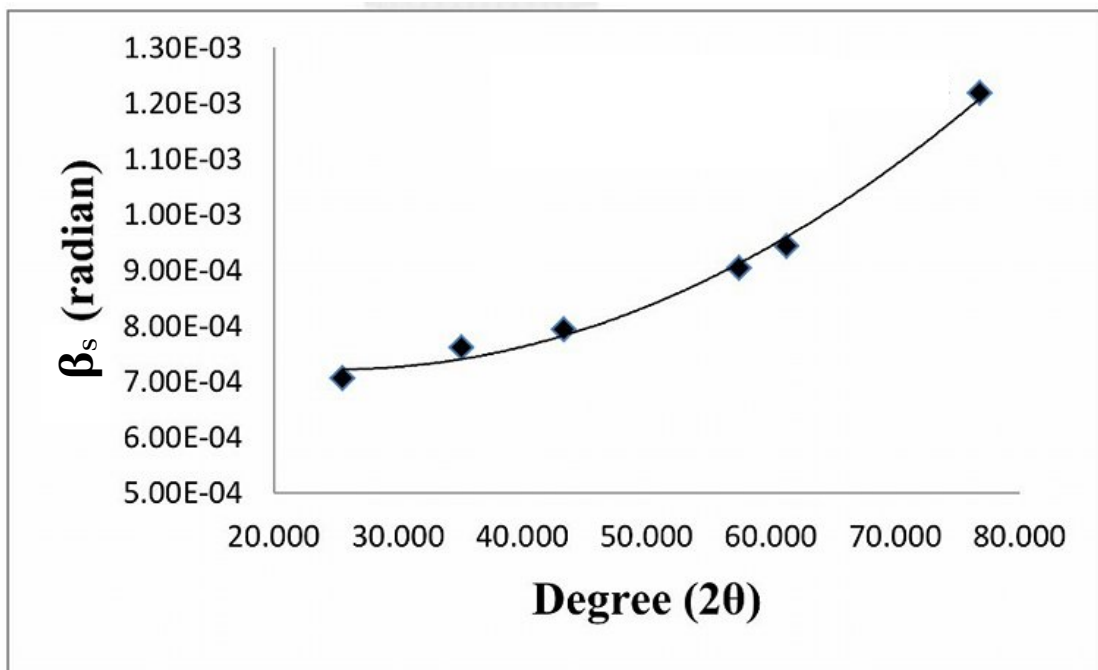
Figure 74 Graph of the full width at half maximum in radians for α-Al$_2$O$_3$ that used as standard.

APPENDIX C

CALCULATION OF ACTIVE SITE, METAL DISPERSION

AND METAL PARTICLE SIZE

C.1 Calculation of active site

Active site of catalyst can be calculated by Eq. (C.1).

$$\text{Active site} = \frac{\text{Moles of metal chemisorbed } H_2}{\text{Total weight of catalyst}} = \frac{V_{H_2, STP} \times S}{W \times 22414} \tag{C.1}$$

Where $V_{H_2, STP}$ is volume of H_2 chemisorbed at STP, cm^3.

W is total weight of catalyst, g.

S is stoichiometric factor of H_2 to Ru atom or H_2/Ru = 2

C.2 Calculation of metal dispersion

Metal dispersion can be calculated by Eq. (C.2) [69, 70].

$$\text{Metal dispersion (\%)} = \frac{\text{Number of metal atoms chemisorbed } H_2}{\text{Total number of metal atoms in catalyst}}$$

$$= \frac{V_{H_2, STP} \times S \times M \times 100}{\text{Metal weight \%}} \tag{C.2}$$

Where $V_{H_2, STP}$ is volume of H_2 chemisorbed at STP, cm^3.

M is molecular weight of metal, g/mol.

S is stoichiometric factor of H_2 to Ru atom or H_2/Ru = 2

C.3 Calculation of metal particle size

Metal particle size can be calculated by equation reported by Shen X. et al. [69] that followed in Eq. (C.3).

$$\text{Metal particle size} = \frac{6v_m}{\%\text{metal dispersion} \times a_m} \tag{C.3}$$

Where v_m is the volume occupied by a metal atom = 13.65×10^{-3} nm^3 for Ru

a_m is the surface area occupied by an exposed surface metal atom

= 9.09×10^{-2} nm^2
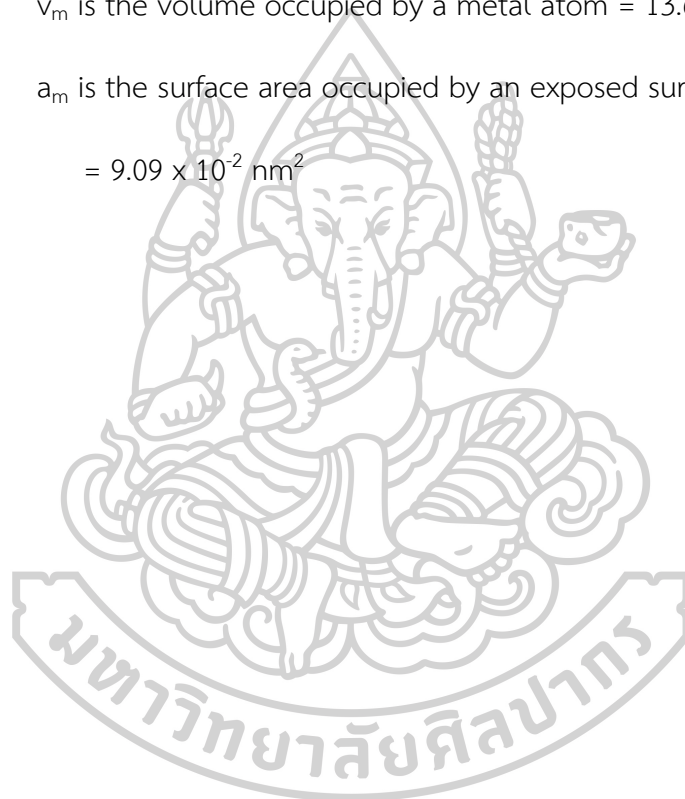
APPENDIX D

CALCULATION OF CO_2 CONVERSION, CH_4 SELECTIVITY, CH_4 YIELD, CH_4 FORMATION RATE AND TOF

Composition of outlet gases mixture in reaction test is measured by GC-TCD equipment which it reports as area of species' peak. The calibration curves of species observed in this research are shown in **Figure 75 – 77**.

Figure 75 contains a plot of "Area of CO_2 peak" versus "vol.% CO_2" with the fitted equation:

$$y = 9459.8x$$
$$R^2 = 0.9983$$
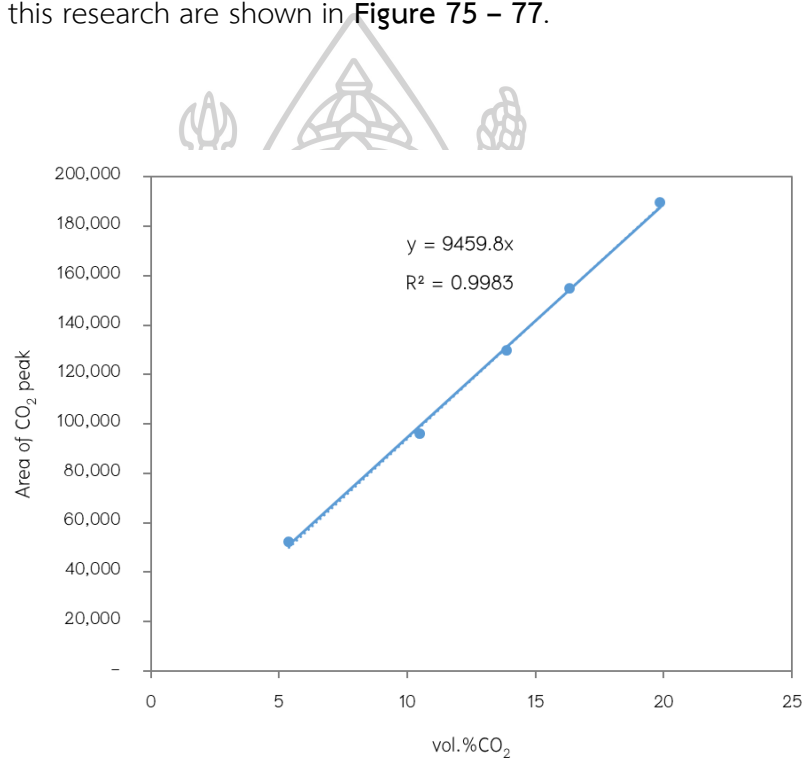
Figure 75 Calibration curve of CO_2 peak measured by GC-TCD.
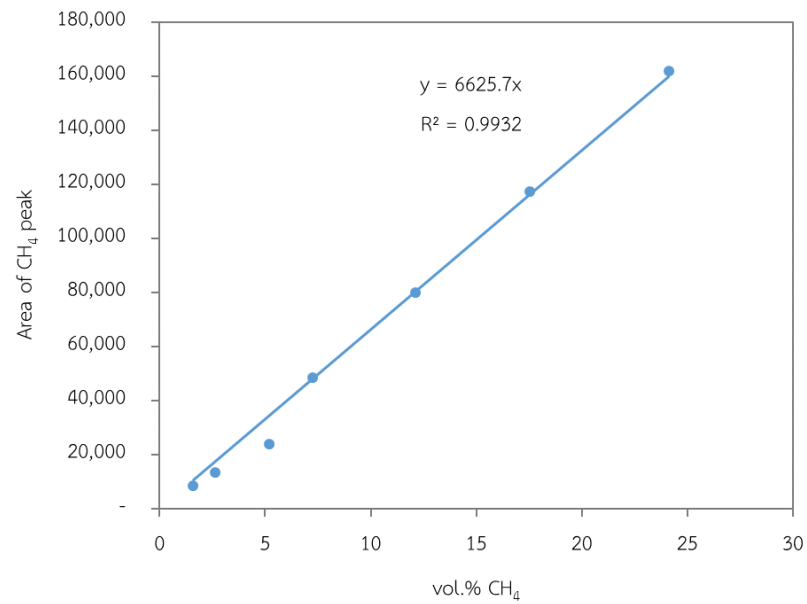
Figure 76 Calibration curve of CH_4 peak measured by GC-TCD.
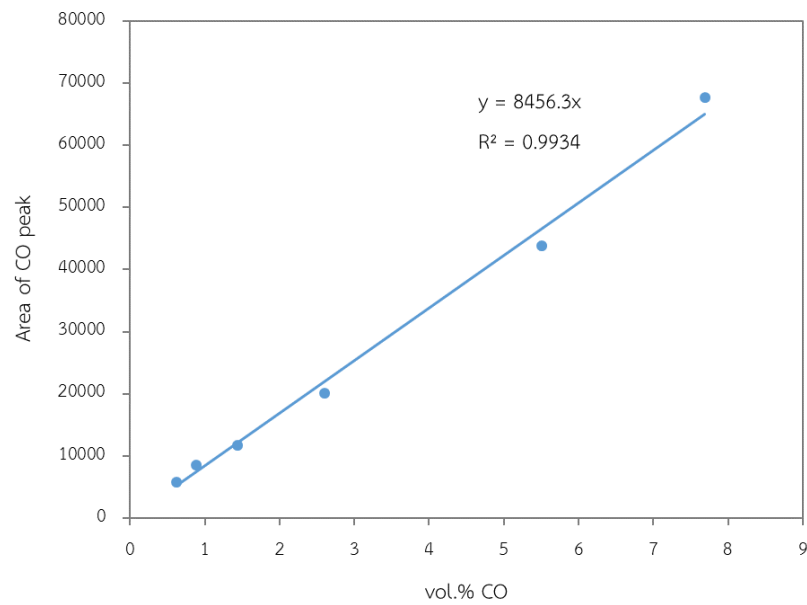
Figure 77 Calibration curve of CO peak measured by GC-TCD.

D.1 Calculation of CO_2 conversion

CO$_2$ conversion can be calculated by Eq. (D.1).

$$CO_2 \text{ conversion (\%)} = \frac{\text{Area of CO}_2 \text{ inlet peak - Area of CO}_2 \text{ outlet peak}}{\text{Area of inlet CO}_2 \text{ peak}} \times 100 \qquad (D.1)$$

D.2 Calculation of CH_4 selectivity

CH$_4$ selectivity can be calculated by Eq. (D.2).

$$CH_4 \text{ selectivity (\%)} = \frac{\text{Area of CH}_4 \text{ peak}}{\text{Area of CH}_4 \text{ peak + Area of CO peak}} \times 100 \qquad (D.2)$$

D.3 Calculation of CH_4 yield

CH$_4$ yield can be calculated by Eq. (D.3).

$$CH_4 \text{ yield (\%)} = CH_4 \text{ selectivity} \times CO_2 \text{ conversion} \qquad (D.3)$$

D.4 Calculation of CH_4 formation rate

CH$_4$ formation rate can be calculated by Eq. (D.4).

$$\underset{\text{(moles/g}_{cat.}\cdot\text{time)}}{CH_4 \text{ formation rate}} = \frac{\text{Molar folw rate of CO}_2 \text{ inlet} \times CO_2 \text{ conversion}}{\text{Weight of catalyst}} \times CH_4 \text{ selectivity}$$

$$(D.4)$$

D.5 Calculation of turnover frequency (TOF)

Turnover frequency (TOF) can be calculated by Eq. (D.5).

$$\text{TOF (time}^{-1}) = \frac{\text{Molar folw rate of } CO_2 \text{ inlet} \times CO_2 \text{ conversion}}{\text{Active site} \times \text{Weight of catalyst}} \tag{D.5}$$

REFERENCES

1. Wang, W., et al., *Recent advances in catalytic hydrogenation of carbon dioxide.* Chem Soc Rev, 2011. **40**(7): p. 3703-27.

2. Janke, C., et al., *Catalytic and adsorption studies for the hydrogenation of CO2 to methane.* Applied Catalysis B: Environmental, 2014. **152-153**: p. 184-191.

3. Su, X., et al., *Catalytic carbon dioxide hydrogenation to methane: A review of recent studies.* Journal of Energy Chemistry, 2016. **25**(4): p. 553-565.

4. Li, D., et al., *Catalytic properties of sprayed Ru/Al2O3 and promoter effects of alkali metals in CO2 hydrogenation.* Applied Catalysis A: General, 1998. **172**(2): p. 351-358.

5. Chaitree, W., et al., *Effect of nanocrystalline χ-Al2O3 structure on the catalytic behavior of Co/Al2O3 in CO hydrogenation.* Catalysis Today, 2011. **164**(1): p. 302-307.

6. Malki, A., et al., *Calcination products of gibbsite studied by X-ray diffraction, XPS and solid-state NMR.* Journal of Solid State Chemistry, 2014. **215**: p. 8-15.

7. Liu, S.H., et al., *In situ EXAFS studies of copper on ZrO2 during catalytic hydrogenation of CO2.* Journal of Electron Spectroscopy and Related Phenomena, 2005. **144-147**: p. 373-376.

8. Xu, J., et al., *CO2 methanation over TiO2–Al2O3 binary oxides supported Ru catalysts.* Chinese Journal of Chemical Engineering, 2016. **24**(1): p. 140-145.

9. Garbarino, G., et al., *Methanation of carbon dioxide on Ru/Al2O3 and Ni/Al2O3 catalysts at atmospheric pressure: Catalysts activation, behaviour and stability.* International Journal of Hydrogen Energy, 2015. **40**(30): p. 9171-9182.

10. Saeidi, S., et al., *Mechanisms and kinetics of CO2 hydrogenation to value-added products: A detailed review on current status and future trends.* Renewable and Sustainable Energy Reviews, 2017. **80**: p. 1292-1311.

11. Lunde, P.J. and F.L. Kester, *Carbon Dioxide Methanation on a Ruthenium Catalyst.* Industrial & Engineering Chemistry Process Design and Development, 1974. **13**(1): p. 27-33.

12. S. Duyar, M., et al., *Kinetics of CO2 methanation over Ru/γ-Al2O3 and implications for renewable energy storage applications.* Journal of CO2 Utilization, 2015. **12**: p. 27-33.

13. Wikipedia, *Platinum group*, in *Wikipedia*. Wikipedia: https://en.wikipedia.org/wiki/Platinum_group#Ruthenium.

14. Lenntech, *Ruthenium - Ru*, in *Periodical table*. Lenntech: https://www.lenntech.com/periodic/elements/ru.htm.

15. Chemistry, R.S.o., *Ruthenium*, in *Periodic Table*. Royal Soctety of Chemistry: http://www.rsc.org/periodic-table/element/44/ruthenium.

16. Britannica, T.E.o.E., *Ruthenium*, in *Encyclopædia Britannica*. 2018, Encyclopædia Britannica, inc.: https://www.britannica.com/science/ruthenium.

17. Staff, L.S., *Facts About Ruthenium*, in *Planet Earth*. 2013, Live Science: https://www.livescience.com/34836-ruthenium.html.

18. Jadhav, S.G., et al., *Catalytic carbon dioxide hydrogenation to methanol: A review of recent studies.* Chemical Engineering Research and Design, 2014. **92**(11): p. 2557-2567.

19. Britannica, T.E.o.E., *Alumina*, in *Encyclopædia Britannica*. 2016, Encyclopædia Britannica, inc.: https://www.britannica.com/science/alumina.

20. Young, J.A., *Aluminum Oxide, Al2O3.* Journal of Chemical Education, 2003. **80**(3): p. 258.

21. K., D., *Material Review: Alumina (Al2O3).* School of Doctoral Studies (European Union) Journal, 2010: p. 107-114.

22. P. Souza Santosa, H.S.S., S.P. Toledo, *Standard Transition Aluminas. Electron Microscopy Studies.* Materials Research, 2000. **3**(4): p. 104-114.

23. Meephoka, C., et al., *Effect of phase composition between nano γ- and χ- Al2O3 on Pt/Al2O3 catalyst in CO oxidation.* Catalysis Communications, 2008. **9**(4): p. 546-550.

24. Favaro, L., et al., *Experimental and ab initio infrared study of χ-, κ- and α- aluminas formed from gibbsite.* Journal of Solid State Chemistry, 2010. **183**(4): p. 901-908.

25.   DaNa2.0, *Zirconium Dioxide*, in *DaNa2.0*

DaNa2.0: https://nanopartikel.info/en/nanoinfo/materials/zirconium-dioxide.

26.   AZoNano, *Zirconium Oxide Nanoparticles – Properties, Applications*, in *AZoNano*. AZoNetwork: https://www.azonano.com/article.aspx?ArticleID=3347.

27.   Cai, M., et al., *Methanation of carbon dioxide on Ni/ZrO2-Al2O3 catalysts: Effects of ZrO2 promoter and preparation method of novel ZrO2-Al2O3 carrier.* Journal of Natural Gas Chemistry, 2011. **20**(3): p. 318-324.

28.   Basu, B., J. Vleugels, and O.V.D. Biest, *Transformation behaviour of tetragonal zirconia: role of dopant content and distribution.* Materials Science and Engineering: A, 2004. **366**(2): p. 338-347.

29.   Wikipedia, *Zirconium dioxide*, in *Wikipedia*. Wikipedia: https://en.wikipedia.org/wiki/Zirconium_dioxide.

30.   Yoshimura, M., *Phase Stability of Zirconia.* Vol. 67. 1988, ResearchGate: American Ceramic Society Bulletin.

31.   Design, M., *Temperature-Dependent Phase Transitions of ZrO2*, in *Materials Design*. Materials Design, Inc.: http://www.materialsdesign.com/appnote/temperature-dependent-phase-transitions-zro2.

32.   Patra, D., *Titanium dioxide*, in *Encyclopædia Britannica*. 2017, Encyclopædia Britannica, inc.: https://www.britannica.com/science/titanium-dioxide.

33.   AZoNano, *Titanium Oxide (Titania, TiO2) Nanoparticles – Properties, Applications*, in *AZoNano*. AZoNetwork: https://www.azonano.com/article.aspx?ArticleID=3357.

34.   Hanaor, D.A.H. and C.C. Sorrell, *Review of the anatase to rutile phase transformation.* Journal of Materials Science, 2011. **46**(4): p. 855-874.

35.   Allen, N.S., et al., *The effect of crystalline phase (anatase, brookite and rutile) and size on the photocatalytic activity of calcined polymorphic titanium dioxide (TiO2).* Polymer Degradation and Stability, 2018. **150**: p. 31-36.

36.   Wikipedia, *Titanium dioxide*, in *Wikipedia*. Wikipedia: https://en.wikipedia.org/wiki/Titanium_dioxide.

37. Lin, Q., et al., *Crystal phase effects on the structure and performance of ruthenium nanoparticles for CO2 hydrogenation.* Catalysis Science & Technology, 2014. **4**(7): p. 2058-2063.

38. Diebold, U., *The surface science of titanium dioxide.* Surface Science Reports, 2003. **48**(5): p. 53-229.

39. Wetchakun, N. and S. Phanichphant, *Effect of temperature on the degree of anatase–rutile transformation in titanium dioxide nanoparticles synthesized by the modified sol–gel method.* Current Applied Physics, 2008. **8**(3): p. 343-346.

40. Chen, X. and S.S. Mao, *Titanium Dioxide Nanomaterials: Synthesis, Properties, Modifications, and Applications.* Chemical Reviews, 2007. **107**(7): p. 2891-2959.

41. Ovenstone, J. and K. Yanagisawa, *Effect of Hydrothermal Treatment of Amorphous Titania on the Phase Change from Anatase to Rutile during Calcination.* Chemistry of Materials, 1999. **11**(10): p. 2770-2774.

42. Hu, Y., H.L. Tsai, and C.L. Huang, *Effect of brookite phase on the anatase–rutile transition in titania nanoparticles.* Journal of the European Ceramic Society, 2003. **23**(5): p. 691-696.

43. Fei Yin, Z., et al., *Recent progress in biomedical applications of titanium dioxide.* Physical Chemistry Chemical Physics, 2013. **15**(14): p. 4844-4858.

44. Woodley, S.M. and C.R.A. Catlow, *Structure prediction of titania phases: Implementation of Darwinian versus Lamarckian concepts in an Evolutionary Algorithm.* Computational Materials Science, 2009. **45**(1): p. 84-95.

45. Chang, P.-L., et al., *Size effects on χ- to α-Al2O3 phase transformation.* Journal of the European Ceramic Society, 2009. **29**(16): p. 3341-3348.

46. A. Tonejc, A.M.T.a.D.B., *Comparison of the transformation sequence from γ-AlOOH (boehmite) to α-Al2O3 (corundum) induced by heating and by ball milling* Materials Science and Engineering, 1994. **A181/A182**: p. 1227-1231.

47. Al'myasheva, O.V., et al., *Preparation of Nanocrystalline Alumina under Hydrothermal Conditions.* Inorganic Materials, 2005. **41**(5): p. 460-467.

48. Kanezaki, E., et al., *Direct Detection of a Phase Change in PdO/CeO2 Supported on χ-Al2O3 by Means of in situ High-Temperature Measurements of XRD and*

FTIR. Analytical Sciences, 2004. **20**(7): p. 1069-1073.

49. Janlamool, J. and B. Jongsomjit, *Catalytic Ethanol Dehydration to Ethylene over Nanocrystalline chi- and gamma-Al2O3 Catalysts.* Journal of oleo science, 2017. **66**(9): p. 1029-1039.

50. Stangeland, K., et al., *CO2 Methanation: The Effect of Catalysts and Reaction Conditions.* Energy Procedia, 2017. **105**: p. 2022-2027.

51. Panagiotopoulou, P., *Hydrogenation of CO2 over supported noble metal catalysts.* Applied Catalysis A: General, 2017. **542**: p. 63-70.

52. Iizuka, T., Y. Tanaka, and K. Tanabe, *Hydrogenation of CO and CO2 over rhodium catalysts supported on various metal oxides.* Journal of Catalysis, 1982. **76**(1): p. 1-8.

53. Fujita, S.-I. and N. Takezawa, *Difference in the selectivity of CO and CO2 methanation reactions.* Chemical Engineering Journal, 1997. **68**(1): p. 63-68.

54. Li, D., et al., *Hydrogenation of CO2 over sprayed Ru/TiO2 fine particles and strong metal–support interaction.* Applied Catalysis A: General, 1999. **180**(1): p. 227-235.

55. Kwak, J.H., L. Kovarik, and J. Szanyi, *CO2 Reduction on Supported Ru/Al2O3 Catalysts: Cluster Size Dependence of Product Selectivity.* ACS Catalysis, 2013. **3**(11): p. 2449-2455.

56. Suo, Z.-h., et al., *Characterization of TiO2-, ZrO2- and Al2O3-supported iron catalysts as used for CO2 hydrogenation.* Applied Catalysis A: General, 1997. **148**(2): p. 301-313.

57. Rynkowski, J.M., et al., *Characterization of Ru/CeO2-Al2O3 catalysts and their Performance in CO2 Methanation.* Reaction Kinetics and Catalysis Letters, 2000. **71**(1): p. 55-64.

58. Thommes, M., et al., *Physisorption of gases, with special reference to the evaluation of surface area and pore size distribution (IUPAC Technical Report).* Vol. 87. 2015: Pure and Applied Chemistry.

59. Nurunnabi, M., et al., *Effects of Ruthenium Precursors on Ru/Mn/Al2O3 and Ru/Al2O3 Catalysts for Fischer-Tropsch Synthesis.* Journal of the Japan Petroleum Institute, 2010. **53**: p. 75-82.

60.   Murata, S. and K.-I. Aika, *Preparation and characterization of chlorine-free ruthenium catalysts and the promoter effect in ammonia synthesis.: 1. An alumina-supported ruthenium catalyst.* Journal of Catalysis, 1992. **136**(1): p. 110-117.

61.   Nurunnabi, M., et al., *Effect of Mn addition on activity and resistance to catalyst deactivation for Fischer–Tropsch synthesis over Ru/Al2O3 and Ru/SiO2 catalysts.* Catalysis Communications, 2007. **8**(10): p. 1531-1537.

62.   Liu, Y., et al., *In situ Raman study on the partial oxidation of methane to synthesis gas over Rh/Al2O3 and Ru/Al2O3 catalysts.* Journal of Catalysis, 2008. **256**(2): p. 192-203.

63.   Wang, M., et al., *Oscillations during partial oxidation of methane to synthesis gas over Ru/Al2O3 catalyst.* Journal of Natural Gas Chemistry, 2009. **18**(3): p. 300-305.

64.   Basahel, S., et al., *Influence of crystal structure of nanosized ZrO2 on photocatalytic degradation of methyl orange.* Vol. 10. 2015, https://www.researchgate.net/publication/273322523: Nanoscale Research Letters.

65.   Souza, M.M.V.M., D.A.G. Aranda, and M. Schmal, *Reforming of Methane with Carbon Dioxide over Pt/ZrO2/Al2O3 Catalysts.* Journal of Catalysis, 2001. **204**(2): p. 498-511.

66.   Yuangpho, N., et al., *Enhanced photocatalytic performance of TiO2 particles via effect of anatase–rutile ratio.* Physica E, 2015. **67**: p. 18-22.

67.   Vannice, M.A., *The catalytic synthesis of hydrocarbons from H2CO mixtures over the group VIII metals: I. The specific activities and product distributions of supported metals.* Journal of Catalysis, 1975. **37**(3): p. 449-461.

68.   Shah, M.A., M.A. Bhat, and J.P. Davim, *Nanotechnology Applications for Improvements in Energy Efficiency and Environmental Management* Nanomaterials, Novel Preparation Routes and Characterizations, ed. I.A. Wani. 2014, United States of America: IGI Global.

69.   Shen, X., et al., *Behavior of H2 chemisorption on Ru/TiO2 surface and its application in evaluation of Ru particle sizes compared with TEM and XRD*

analyses. Applied Catalysis A: General, 2008. **335**(2): p. 187-195.

70.   Okal, J., et al., *The use of hydrogen chemisorption for the determination of Ru dispersion in Ru/γ-alumina catalysts.* Applied Catalysis A: General, 2007. **319**: p. 202-209.

VITA

NAME   Kanyanat Jeenjumras

DATE OF BIRTH   29 May 1992

PLACE OF BIRTH   Nakornpathom, Thailand

HOME ADDRESS   191, Sakormthanakorn Road, Lumpaya District,

Meuang Nakorn Pathom, Nakorn Pathom Province 73000